A STUDY OF DOMAIN DYNAMICS IN PERPENDICULARLY-MAGNETIZED ULTRATHIN IRON FILMS

A STUDY OF DOMAIN DYNAMICS IN PERPENDICULARLY-MAGNETIZED ULTRATHIN IRON FILMS

By

NIDAL M. ABU-LIBDEH, M.Sc.

A Thesis
Submitted to the School of Graduate Studies
in Partial Fulfillment of the Requirements
for the Degree of
Doctor of Philosophy

McMaster University

DOCTOR OF PHILOSOPHY (2010)
(Physics & Astronomy)

McMaster University
Hamilton, Ontario, Canada

TITLE: A Study of Domain Dynamics in Perpendicularly-Magnetized Ultrathin Iron Films

AUTHOR: Nidal M. Abu-Libdeh, B.Sc.(Yarmouk University, Irbid, Jordan), M.Sc.(Memorial University, St.John's, Newfoundland, Canada)

SUPERVISOR: Dr. D. Venus

NUMBER OF PAGES: xviii, 137

Abstract

Relaxation mechanisms in perpendicularly-magnetized ultrathin Fe/ 2 ML Ni(111)/ W(110) films, with thickness between 1.25 and 2.00 ML, have been studied using the ac magnetic susceptibility as a function of temperature and/or time. Different time scales were probed by varying the constant rate of temperature variation, R as the susceptibility was measured. After quenching the film from high temperature, the susceptibility curve was found to relax through a shift in the peak position along the temperature axis and through changes in shape, as a function of time. In general, two opposing behaviors were found; for small R (≤ 0.30 K/s) the susceptibility peak temperature decreases as R increases, for large R (≥ 0.30 K/s) the peak temperature increases with R. The first behavior is understood as a "dynamical observation" of a domain phase transformation. The density of topological defects in the quenched high temperature delocalized phase undergoes an activated relaxation as low temperature ordered stripe phase is established. The fundamental time scale (τ_{0R}) of this process is in the order of 1.0 s. These findings complement the results of numerical simulation [24, 26, 27] and quantify the important dynamical barriers involved in the geometrical rearrangement of domains in moving from a delocalized phase to the ordered stripe phase. The experiments at large R are sensitive to a much shorter time scale over which the domain density equilibrates when temperature is changed. This process causes an increase in the peak temperature with R that depends linearly on R over the range of values of R accessible in this study.

Acknowledgements

I would like to express my deep gratitude to my thesis supervisor Prof. David Venus for providing the facilities and for giving me the opportunity to work and learn new things in his research group. His expertise, combined with kind patience and unbelievably positive attitude have helped and encouraged me many times during the years of my study.

I would also like to thank Prof. Takashi Imai and Prof. Marek Niewczas for their participation on my thesis committee. They provided me with many helpful comments and suggestions throughout my study.

It is my pleasure to thank Marek Kiela for his invaluable technical assistance and his warm friendship. Without his expertise, my work would have been extremely difficult. Many thanks should also go to Dr. Michael Dunlavy and Dr. Q. Li for teaching me how to master surface science experiments. Many thanks to Katharina Fritsch for her collaboration in the Lab., and for proofreading some of the chapters of this thesis. Thanks to Rob D'Ortenzio and Edgar Xutuc for the valuable friendship and good times I spent with them in the Lab. Special thanks to my dear friend Azzam Hazim for his incredible support and friendship.

Finally, I would like to thank my wife Nivin for encouragement and patience during the course of my work. Warm thanks to my children Alaa, Muhammad and Omar. This thesis is dedicated to them.

Abbreviations

ML: Monolayer

GMR: Giant Magnetoresistance

MOKE: Magneto-Optic Kerr Effect

SMOKE: Surface Magneto-Optic Kerr Effect

SRT: Spin Reorientation Transition

LEED: Low-Energy Electron Diffraction

AES: Auger Electron Spectroscopy

ARAES: Angle Resolved Auger Electron Spectroscopy

hcp: Hexagonal Close-Packed

fcc: Face Centered Cubic

bcc: Body Centered Cubic

MSA: Magnetic Surface Anisotropy

SDS: Stripe Domain Structure

PMA: Perpendicular Magnetic Anisotropy

UHV: Ultrahigh Vacuum

TSP: Titanium Sublimation Pump

MBE: Molecular Beam Epitaxy

FM: Frank-van der Merwe growth mode

VW: Volmer-Weber growth mode

SK: Stranski-Krastanov growth mode

RFA: Retarding Field Analyzer

FWHM: Full Width at Half Maximum

SSR: Square Sum of Residual

Contents

List of Figures

List of Tables

Chapter 1

Introduction

Magnetization of ultrathin films (a few atomic layers in thickness) is a very active field of research in recent years. This is due to their great potential for application in areas such as magnetic sensors and high density storage devices, and their use as models in the study of fundamental properties of magnetism in two dimensions. The research in this field has revealed some new interesting phenomena such as giant magnetoresistance (GMR) [1], and oscillatory exchange coupling between ferromagnetic layers separated by a non-magnetic layer [2].

In ultrathin magnetic films, one might expect it to be energetically favorable for the magnetization to lie in the plane, to minimize the stray fields. Surprisingly, however, a significant proportion of the magnetic films with a thickness less than 10 atomic layers support the magnetization perpendicular to the film plane. This phenomenon is derived from the breaking of the translational symmetry at a surface, and the "surface anisotropy" that results. In some cases the surface anisotropy favors a perpendicular magnetization and overcomes the short-range part of the dipole interaction to create a uniaxial perpendicular anisotropy. In ultrathin films with perpendicular anisotropy, the long-range dipole-dipole interaction is effectively antiferromagnetic and thus drives the formation of magnetic domains. In this work, we provide an experimental study of the dynamics of these domains in perpendicularly magnetized ultrathin iron films. Magnetic properties are characterized by using the surface magneto-optic Kerr effect (SMOKE) to measure the complex magnetic ac-susceptibility of the ultrathin iron films.

1.1 Review of Previous Studies

The remarkable advances in computational performance (see for example [3]) and improvement in the ability to grow and characterize metal films of a few atomic layer in thicknesses on a metal substrate (see for example [4–7] have lead to a series of exciting observations regarding the character of the magnetic domains in ultrathin films. The domain structure in ferromagnetic materials arises from a balance between the short range ferromagnetic exchange interaction, magnetocrystalline anisotropy and shape anisotropy (dipolar) energies. In an ultrathin film, the surface magnetocrystalline anisotropy is large and may hold the magnetization perpendicular to the plane of the film. As the film thickness increases, at constant temperature, the competition between the two anisotropies results in a spin reorientation transition (SRT) point where the magnetization flips to lie in the plane of the film [8–10]. This is known as a thickness-driven spin-reorientation transition. A temperature-driven spin-reorientation transition occurs as the temperature increases at constant thickness as predicted by Pescia and Pokrovsky [11] and observed experimentally by Pappas *et al.* [12] in a system consisting of ultrathin fcc Fe films grown on Cu(001) substrate at low temperature.

In the case of thin films with in-plane magnetization the domain state in equilibrium is a single domain state (if edge effects are neglected). By contrast, the domain structure in perpendicularly magnetized ultrathin films is expected, according to theoretical and computational studies, to undergo a series of phases as the temperature

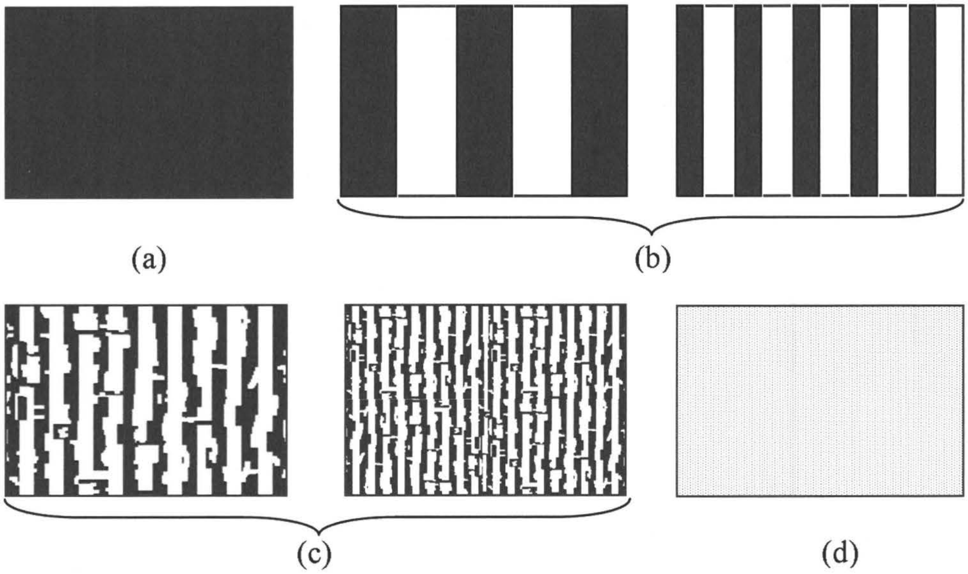

Figure 1.1: *A schematic graph of domain structures in perpendicularly magnetized ultrathin films, as the temperature is increased. Temperature increases left to right top to bottom. (a) a single domain phase, (b) an ordered stripe domain phase, (c) a delocalized domain phases, and (d) a paramagnetic phase. Stripe domain density is an exponential function of temperature.*

is increased (Fig. 1.1). At low temperature, the domains are expected to be so large that a single domain will occupy the entire sample (Fig. 1.1a). In this case the film has a net magnetic moment [13–16]. This is consistent with the experimental observation of a net ferromagnetic moment in the out-of-plane orientation at low temperature [17]. At a characteristic temperature, the film loses its net magnetic moment due to the formation of multiple domains in an ordered stripe domain phase (Fig. 1.1b). For samples with square or rectangular symmetry, the domain walls are oriented along a common crystallographic axis in the ordered stripe domain phase [3, 14–16, 18–20]. A continuum model indicates that as the temperature is increased, the averaged stripe domain width, L, decreases exponentially and the domain density, n $(\sim \frac{1}{L})$, undergoes a corresponding exponential increase [14–16, 21, 22]. As the temperature further increases, the surface anisotropy decreases significantly and fluctuations in the domain walls become important and minimize the free energy by breaking the ordered stripe domains into segments which may not aligned along a single axis [3, 14–16, 19, 20]. Domain phases of this type include Ising nematic phase and tetragonal phase (Fig. 1.1c). In the Ising nematic phase, the domains have no positional order, but they have long-range orientational order, while in the tetragonal phase domains of mutually perpendicular stripes appear [3, 16, 19, 20]. In this study, these types of phases are referred to as "delocalized" phases. Finally, as the temperature increases, the tetragonal state is replaced by a paramagnetic state (Fig. 1.1d), although it is not clear whether or not this occurs by gradual collapse of domains [3, 16, 20].

There are many theoretical studies of the phase diagram and the dynamics of domains in ultrathin film with perpendicular anisotropy [3, 13–16, 18–20, 23–29]. In a Monte Carlo study of a system of Ising spins aligned perpendicular to the plane of the lattice, it has been found that as temperature increases, a continuous phase transition from low temperature stripe phase to a high temperature tetragonal phase takes place [19, 20]. However, it is later argued that the phase transition observed by Booth *et al.* [20] should correspond to a nematic - tetragonal phase transition [23]. Moreover, in recent studies [28, 29] it has been suggested that the phase transition is a first-order transition not a continuous one. In a subsequent work by Cannas *et al.* [27], it is found that the phase transition can proceed directly from the ordered stripe phase to the tetragonal phase or through an intermediate nematic phase depending on the dipolar strength relative to the exchange coupling . A Monte Carlo study by Bromley *et al.* [24] has simulated the dynamics of the same system mentioned above. They have considered the relaxation of an initially saturated magnetic state toward the equilibrium. At low temperature, they find that the relaxation toward the ordered stripe phase occurs over three time scales: a short time scale over which the magnetization slowly decays through the nucleation and growth of domains of spins with opposite orientation to the initial magnetization; an intermediate time scale over which the number of up and down domains equilibrate; and a long time scale over which the system relaxes by rearranging the stripe domains along a single axis. At high temperature however, the relaxation process was found to be described by a single process in which the magnetization rapidly decays to zero, beyond which the system is in the equilibrium tetragonal phase. More recently, Cannas *et al.* [26] studied the dynamical behavior of the same system after a sudden quench of the tetragonal phase to low temperature. Their finding was that the quenched state relaxes to the equilibrium state in two different ways: initial relaxation to a metastable nematic phase that then decays slowly to the low temperature ordered stripe phase by nucleation; or alternatively, by direct nucleation of the equilibrium ordered stripe phase by rearrangement of stripe domains along a single axis.

Although there are many experimental studies of the behavior of perpendicularly magnetized ultrathin films [30–40], very few have studied the dynamical properties [7, 32, 39]. The vast majority of these studies use magnetic imaging techniques where they mostly observe the ordered stripe domain phase and characterize its dependence upon film thickness [30] or upon temperature [31, 33]. Delocalized domain phases are rarely observed [30]. Instead a direct phase transformation from stripe to paramagnetic phase has been observed, which is identified as a Curie transition [31, 33]. This raises the question of whether the delocalized phases is rare, or is difficult to image.

In the last number of years, our group at McMaster University have concentrated on the structure and magnetic properties of the perpendicularly magnetized ultrathin Fe films deposited on a 2 monolayers (ML) Ni(111)/W(110) substrate [5, 34–39, 41, 42]. The 2 ML ultrathin Ni buffer on top of W(110) is used to allow good wetting and lattice matching for the growth of fcc Fe films. Low-energy electron diffraction (LEED) and angle-resolved Auger electron spectroscopy (ARAES) show that the Fe films grow as slightly distorted (111)-fcc for up to 3 ML, after which a gradual deformation to the bcc structure has been found [5, 40]. Complex magnetic ac-susceptibility measurements $\chi(= \chi^{'} + i\chi^{''})$ as a function of temperature [35, 37] have revealed that Fe films with thicknesses of 2.2 ML or less have an out-of-plane moment, whereas a temperature-driven spin reorientation transition (SRT) from the out-of-plane to in-plane orientation occurs for films thicker than 2.2 ML. The ac-susceptibility is described, as proposed by Kashuba and Pokrovsky [14, 15], to the domain wall motion. The real part of the susceptibility, $\chi^{'}$, was found to be well described by two processes [35–38, 42]. The susceptibility arises from the linear response of the domain state to an applied magnetic field as those domains with their magnetic moment oriented parallel to the applied field grow at the expense of those with their moment antiparallel to the applied field. As the temperature is increased, the equilibrium stripe domain density, n_{eq}, increases exponentially. The domain walls stiffen with respect to the applied field during condensation and the equilibrium susceptibility, χ_{eq}, decreases exponentially with increasing temperature; that is $\chi_{eq} \propto n_{eq}(T)^{-1} \propto e^{-\kappa T}$. Venus and others [34, 37–39] find that the value of κ obtained experimentally for Fe films lies in the range of (0.04 to 0.055) which is in the same order of magnitude as that which they calculated [37] based on the result of Kashuba and Pokrovsky [14, 15]. In a low temperature range, domain walls are pinned by defects in the film structure and the domain wall motion between pinning sites is thermally activated process with an activation energy. The source of the pinning has been found to be due to the variations in the perpendicular magnetic anisotropy at the monolayer steps in the film thickness [37, 38] which is in agreement with theory [43]. In a recent study by Venus and Dunlavy [39], the analysis of the imaginary part of the susceptibility, $\chi^{''}$, has shown that the activation energy does not have a single value, E_a, but rather is represented by a normalized truncated Lorentzian distribution $f(E_a)$. Another important finding is that the domain wall creation and/or annihilation is also an activated process with an activation energy, E_n, distinct from the pinning of existing walls [39, 44, 45]. This causes the stripe domain state to be frozen far from its equilibrium value at low temperature [39].

1.2 Thesis Objective and Outline

As noted above, a perpendicularly-magnetized system could undergo different relaxation processes with different relaxation times. These processes include domains creation with a short time scale, domain density equilibration with an intermediate time scale, and the reorientation of domain segments along a certain favourable direction, with a long time scale. The aim of this work is to identify these different processes dynamically, and characterize time and energy scales involved in each process in a real system consisting of Fe films deposited on a 2 ML Ni(111)/ W(110) substrate. The investigation is made using the magnetic ac susceptibility. Different time scales have been accessed by altering the constant rate of change in temperature variation, R as the susceptibility is measured. A much longer time scale has also been accessed by measuring the susceptibility as a function of time at constant temperature when cooling or heating is stopped.

The presentation of this thesis is organized as follows: following this introductory chapter, the necessary theoretical background materials relevant for this work is presented in Chapter 2. The materials in this chapter are organized in two main parts; in the first part, the magnetism is discusses in general whereas the second part is devoted for the magnetism in ultrathin films with perpendicular anisotropy. In this part, the effect of the relaxation processes on the ac susceptibility is modeled and discussed in more detail. Chapter 3 provides an overview description of the equipment and experimental techniques which were used in the work. Chapter 4 presents the experimental results and discussion, and in chapter 5, the main conclusions of this thesis will be summarized.

Chapter 2

Theory

In the previous chapter, we presented the motivation for this study, and outlined the plan for the discovering the different relaxation mechanisms in a perpendicularly magnetized ultrathin film. In this chapter we give an overview of the necessary theoretical background to the experimental results of this study. This chapter is divided up into two main parts. In the first part, a review of magnetism is discussed in general, while in the second part the magnetism in an ultrathin film is discussed. The reader interested in a more complete description of magnetism is referred to the following excellent texts [46–48].

2.1 Kinds of Magnetism

All materials are in some sense magnetic. Under appropriate conditions, the material is either diamagnetic, paramagnetic, antiferromagnetic, ferrimagnetic, or ferromagnetic. Classically, this classification is determined by the relative alignment of the atomic magnetic moments in the material. The response of a magnetic material to an applied magnetic field is measured by the so-called magnetic susceptibility χ. It is defined as the ratio of the magnetization to the applied magnetic field intensity.

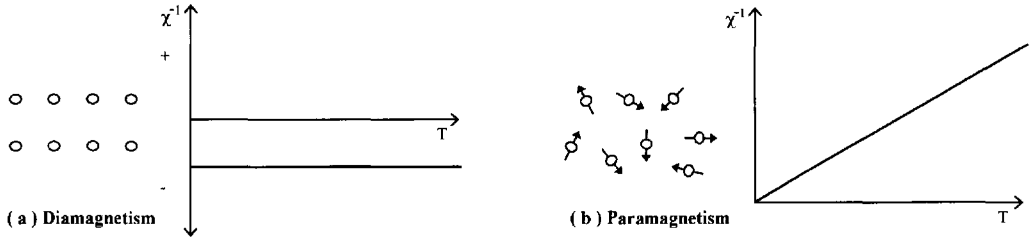

(a) Diamagnetism

(b) Paramagnetism

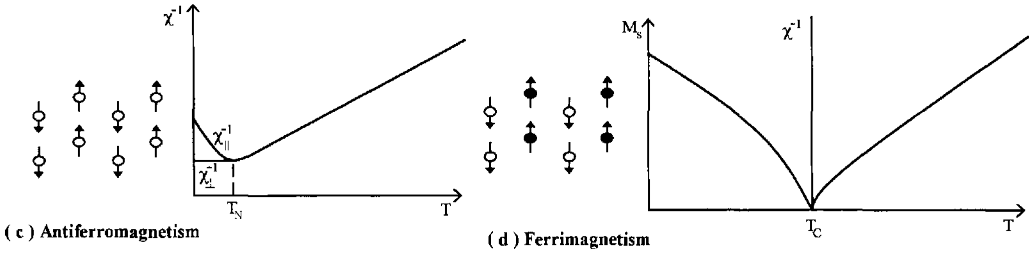

(c) Antiferromagnetism

(d) Ferrimagnetism

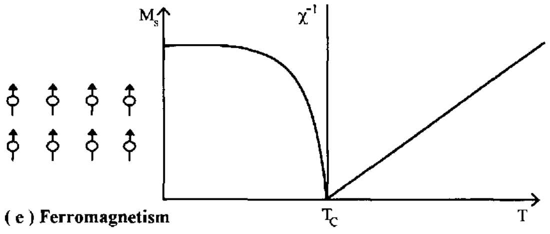

(e) Ferromagnetism

Figure 2.1: *Kinds of magnetism: A circle represents an atom or ion, and an arrow through that circle represents its net magnetic moment. Open and solid circles represents atoms or ions of different magnetic moments (After [46]).*

The following gives a general description of the magnetic structure of each type of the magnetic materials as well as their response to an applied magnetic field as a function of temperature (see Fig. 2.1).

Diamagnetism

A diamagnetic material contains atoms which have no net magnetic moments in zero magnetic filed. In the presence of an applied magnetic field, a net magnetic moment is induced in the material in the opposite direction to the applied magnetic field. The mechanism by which this happens is the acceleration of the orbital electrons by electromagnetic induction caused by the time variation of the applied magnetic field as it penetrates to the orbit. The relative susceptibility of such a material is independent of temperature (Fig. 2.1a). It is negative and small, typically $\chi \simeq 10^{-5}$.

Paramagnetism

The susceptibility of a paramagnetic material is positive and small, of the order of $\chi \simeq 10^{-5} - 10^{-2}$. The paramagnetic susceptibility of localized magnetic moments is a temperature dependent quantity (Fig. 2.1b), given by the Curie law

$$\chi = \frac{constant}{T}. \tag{2.1}$$

This magnetic behaviour is found in materials that contain magnetic atoms or ions that are widely separated so that they exhibit insignificant interaction with one another, and hence, they are randomly oriented relative to each other.

Antiferromagnetism

In an antiferromagnetic material the magnetic moments are aligned antiparallel to one another below a transition temperature T_N (Néel temperature) (Fig. 2.1c). An important feature of antiferromagnets is the temperature dependence of the magnetic susceptibility. Above the Néel temperature, the susceptibility varies in accordance with the Curie-Weiss law

$$\chi = \frac{constant}{T - \Theta_a}, \tag{2.2}$$

where Θ_a is a constant. The relative magnetic susceptibility of antiferomagnetic material, χ, ranges from $10^{-5} - 10^{-2}$, the same as for paramagnets with the difference in magnetic structure. Antiferromagnets are characterized by a strong temperature and field dependence of the susceptibility at $T < T_N$. When the applied magnetic field is parallel to the direction of the magnetic moments, the susceptibility $\chi_{||}$ is temperature dependent and goes to zero at $T = 0$K. On the other hand, when the applied magnetic field is normal to the magnetic moments, the susceptibility $\chi_{\perp}$ has a constant value from $T = 0$ to $T = T_N$ and it is equal the maximum value of $\chi_{||}(T = T_N)$ as shown in Fig. 2.1c.

Ferrimagnetism

In a ferrimagnetic material, as in the case of antiferromagnetes, the magnetic moments are arranged antiparallel to one another below a certain critical temperature (Curie temperature T_C). In contrast to the antiferromagnets, the atomic magnetic moments are unequal so there is no exact cancellation of magnetization. The resultant spontaneous magnetization does not disappear until the Curie temperature is reached as shown in Fig. 2.1d. Above the Curie temperature, ferrimagnets show paramagnetic susceptibility behaviour (Fig. 2.1d), and its dependence on temperature is described by the Curie-Néel law

$$\chi^{-1} = \chi_o^{-1} + \frac{T}{C} + \frac{b}{T - \theta}, \tag{2.3}$$

where χ_o, C, b, and θ are constants.

Ferromagnetism

In a ferromagnetic material, the magnetic moments (caused mostly by the spin of electrons) are aligned to one another as a result of strong positive interaction acting between neighbouring spins (Fig. 2.1e). This gives rise to a large spontaneous magnetization of the sample in some directions (easy magnetization axis). The spontaneous magnetization decreases as temperature increases, and in the absence of an external magnetic field, disappears at a critical temperature (known by the Curie temperature, T$_C$) as shown in Fig. 2.1e. In the vicinity of the Curie temperature ($T \leq T_C$), the temperature dependence of the spontaneous magnetization is

$$M(T) \sim \left(1 - \frac{T}{T_C}\right)^{\beta}, \tag{2.4}$$

where β is called the critical exponent. Above the Curie temperature ($T > T_C$), the ferromagnet behaves like a classical paramagnet with a paramagnetic susceptibility that obeys the Curie-Weiss law

$$\chi = \frac{constant}{T - T_C}. \tag{2.5}$$

In order to minimize its magnetostatic self-energy, the ferromagnetic material is subdivided into domains of different orientation of the magnetization vector for temperatures below the Curie temperature. The concept of domains was originally introduced by Weiss in 1907 [49] to explain why magnetic materials can be in a state of zero total magnetization while still having locally a non-zero spontaneous magnetization. Inside a domain, the magnetization is parallel to one of the preferential directions, which are determined by the *magnetic anisotropy energy* of the crystal. The transition from one direction of magnetization to another in adjacent domain is continuous, i.e, domain walls have a finite width and therefore an internal structure. The reason the magnetic moments change their direction gradually within the domain wall is to minimize the increase in the *exchange energy* due to this change. In the following sections, we will present a detailed review of the properties that determine the magnetic domain structure; among these are the strength of the exchange interaction between magnetic atoms, the demagnetizing field which is related to the magnetostatic self-energy, and the magnetic anisotropy.

2.2 The Exchange Interaction

The exchange interaction is the origin of the alignment of the spins in a magnetic system. The energy of a system of interacting spins is written as

$$\mathcal{H}_{ex} = -J \sum_{i \neq j} \boldsymbol{S}_i \cdot \boldsymbol{S}_j, \tag{2.6}$$

where the coupling constant J is the *exchange integral*, and $\boldsymbol{S}_i$ and $\boldsymbol{S}_j$ are the total spin quantum number of atom i and j respectively. If J is positive, the *exchange energy* associated with the exchange interaction is minimum when the spins are parallel. In the case of a negative exchange integral, the lowest energy state results from antiparallel spins. The exchange interaction is a result of quantum Fermi statistics when applied to electrons interacting by the Coulomb interaction. The exchange energy can be large because it has the coupling strength of the Coulomb interaction.

To illustrate the origin of the exchange interaction, we consider the system of a hydrogen molecule consists of two hydrogen atoms. Each atom has one electron orbiting around a proton. The total wave function of the system $\Psi(\boldsymbol{r}_1, \boldsymbol{s}_1; \boldsymbol{r}_2, \boldsymbol{s}_2)$ can be expressed as a product of two parts, one containing the spatial coordinate $\psi(\boldsymbol{r}_1,\boldsymbol{r}_2)$ and one containing the spin variables $\Theta(\boldsymbol{s}_1,\boldsymbol{s}_2)$; that is

$$\Psi(\boldsymbol{r}_1, \boldsymbol{s}_1; \boldsymbol{r}_2, \boldsymbol{s}_2) = \psi(\boldsymbol{r}_1, \boldsymbol{r}_2)\Theta(\boldsymbol{s}_1, \boldsymbol{s}_2). \tag{2.7}$$

Fermi statistics asserts that the total wave function Ψ must change its sign under the exchange of the two electrons. In other words, Ψ must be an antisymmetric function:

$$\psi(\boldsymbol{r}_1, \boldsymbol{r}_2)\Theta(\boldsymbol{s}_1, \boldsymbol{s}_2) = -\psi(\boldsymbol{r}_2, \boldsymbol{r}_1)\Theta(\boldsymbol{s}_2, \boldsymbol{s}_1). \tag{2.8}$$

This condition can be realized by having the spin wave function, Θ, be symmetric under spin exchange and the spatial wave function, ψ, be antisymmetric under the coordinate exchange, or vice versa. As a first approximation, the spatial wave function

ψ can be written as a linear combination of the wave function for isolated atoms:

$$\psi_{s,a}(\boldsymbol{r}_1, \boldsymbol{r}_2) = \frac{1}{\sqrt{2}}[\varphi_1(\boldsymbol{r}_1)\varphi_2(\boldsymbol{r}_2) \pm \varphi_1(\boldsymbol{r}_2)\varphi_2(\boldsymbol{r}_1)], \tag{2.9}$$

where $\varphi_i(\boldsymbol{r}_j)$ is the spatial wave function of the hydrogen atom with electron i at position $(\boldsymbol{r}_j)$. The subscripts s and a mean symmetric and antisymmetric with respect to the exchange of the electron coordinate $\boldsymbol{r}_1$,$\boldsymbol{r}_2$. On the right-hand side of Eq. 2.9, we take the + sign for s and the - sign for a, and the factor $1/\sqrt{2}$ is required to normalize ψ_s and ψ_a.

The Hamiltonian $\mathcal{H}$ of the hydrogen molecule is given by the sum of those for the isolated atoms, $\mathcal{H}_0$:

$$\mathcal{H}_0 = -\frac{\hbar^2}{2m}\nabla_1^2 - \frac{\hbar^2}{2m}\nabla_2^2 - V_c(\boldsymbol{r}_1, \boldsymbol{R}_1) - V_c(\boldsymbol{r}_2, \boldsymbol{R}_2), \tag{2.10}$$

and the additional term, $\Delta\mathcal{H}$:

$$\Delta\mathcal{H} = V_c(\boldsymbol{r}_1, \boldsymbol{r}_2) + V_c(\boldsymbol{R}_1, \boldsymbol{R}_2) - V_c(\boldsymbol{r}_1, \boldsymbol{R}_2) - V_c(\boldsymbol{r}_1, \boldsymbol{R}_1), \tag{2.11}$$

where $V_c(\boldsymbol{a}, \boldsymbol{b})$ $(= e^2/|\boldsymbol{a} - \boldsymbol{b}|)$ is the Coulomb potential, $\boldsymbol{r}$ and $\boldsymbol{R}$ are the positon of the electron and proton, respectively. Therefore the difference in the energies of the states given by Eq. 2.9 is calculated as

$$E_s - E_a =< \psi_s|\mathcal{H}|\psi_s > - < \psi_a|\mathcal{H}|\psi_a > . \tag{2.12}$$

The calculation of the integration of Eq. 2.12 from the first principals is very complicated task, but can be found for example in Ref.[50] and references therein. In the limit of large distance between the hydrogen atoms, the main part of energy difference between the symmetric and antisymmetric state is given by

$$E_s - E_a = E_{ex} =< \varphi_1(\boldsymbol{r}_1)\varphi_2(\boldsymbol{r}_2)|\frac{e^2}{\boldsymbol{r}_1 - \boldsymbol{r}_2}|\varphi_1(\boldsymbol{r}_2)\varphi_2(\boldsymbol{r}_1) > . \tag{2.13}$$

Although the total Hamiltonian $\mathcal{H}$ does not depend on the spin variables, the energy of the system depends on the relative orientation of the spins. This was first pointed out by Heisenberg in 1928 [51]. To reflect this fact, he introduced a spin Hamiltonian that includes the dependence of the relative orientation of the atomic spins in the form of Eq. 2.6. The step from a hydrogen molecule to a crystal of iron is a giant one as they involve a complicated statistical mechanical treatment.

In summary, one can understand the exchange interaction as the following. When two atoms are adjacent, we can consider electron 1 moving around proton 1, and electron 2 moving around proton 2. But electrons are indistinguishable, and we must also consider the possibility that the two electrons exchange places, so that electron 1 moving around proton 2 and electron 2 moving around proton 1. This consideration introduce an additional term, the exchange energy E_{ex} into the expression of the total energy of the atoms.

2.3 Magnetic Anisotropy

In a ferromagnetic material, the spontaneous magnetization has an easy axis, or several easy axes, along which the magnetization prefers to lie. The easy axis is commonly a crystal axis. For example, in the hexagonal closed-packed (hcp) materials, it is energetically favourable for the magnetization, within a domain, to align along the long c-axis. The dependence of the internal energy of the system on the direction of the spontaneous magnetization is called anisotropy energy.

Two major contributions dominate the anisotropy energy; the spin-orbit coupling and the dipole-dipole interaction. The spin-orbit coupling relates the magnetization to the crystal lattice and results in magnetocrystalline anisotropy. Because of its long-range character, the dipole-dipole interaction leads to a contribution to the anisotropy which depends upon the specimen shape, hence, called the shape anisotropy. Other types of anisotropy can be produced by a special treatment that has directional characteristic such as the application of mechanical stress to the material which induces the magnetoelastic anisotropy. In the following, the magnetocrystalline and shape anisotropies, the most important in magnetic ultrathin films, will be discussed in more detail.

2.3.1 Magnetocrystalline Anisotropy

Magnetocrystalline anisotropy is due to spin-orbit coupling. When an external magnetic field tries to reorient the spin of an electron, the orbit of the electron also tends to be reoriented. But the orbit is strongly coupled to the lattice by the strong crystal electric field, and therefore resists the attempt to rotate the spin axis. The field has the symmetry of the crystal involved. Hence, the magnetocrystalline anisotropy has the same symmetry as the crystal structure of the material.

The magnetocrystalline anisotropy energy can be expanded in successive power of α_x, α_y, α_z, where the α_i are the direction cosines of the orientation of the magnetization with respect to the crystal axes. In case of cubic crystal the terms which include the odd powers of α_i must vanish, because a change in sign of any of the α_i should bring the magnetization vector to a direction which is equivalent to the original direction. Furthermore, the expression can be simplified by the crystal symmetry. In this case, the bulk magnetocrystalline anisotropy energy E_a for a cubic crystal can be expressed as [47]

$$\begin{aligned} E_a &= K_0 + K_1(\alpha_x^2\alpha_y^2 + \alpha_y^2\alpha_z^2 + \alpha_z^2\alpha_x^2) + K_2\alpha_x^2\alpha_y^2\alpha_z^2 \\ &\quad + K_3(\alpha_x^2\alpha_y^2 + \alpha_y^2\alpha_z^2 + \alpha_z^2\alpha_x^2)^2 + \cdots. \end{aligned} \tag{2.14}$$

For a hexagonal crystal, the anisotropy energy has the form [47]

$$E_a = K_0 + K_1 \sin^2\theta + K_2 \sin^4\theta + K_3 \sin^6\theta + K_4 \sin^6\theta \cos^6\phi, \tag{2.15}$$

where θ is the angle between magnetization vector and the hexagonal axis, and ϕ is the azimuthal angle of the magnetization measured from a principal crystallographic direction in the base plane. For a tetragonal lattice, the anisotropy energy reads [47]

$$E_a = K_0 + K_1 \sin^2\theta + K_2 \sin^4\theta + K_3 \cos^2\alpha \cos^2\beta, \tag{2.16}$$

where the magnetization vector makes an angle of θ with respect to the tetragonal axis and forms angles of α and β with other two axes.

The coefficients, $K_i^{'s}$, in the above equations are the magnetic anisotropy constants. They can be either positive or negative depending on the orientation of the easy axis. The form of the magnetocrystalline anisotropy energy is often approximated by the K_1 term. If K_1 is positive as in the case of fcc-Fe, the anisotropy energy E_a for [100] is lower than that for [111], so that [100] becomes the easy axis. Because the cubic symmetry, [010] and [001] are also easy axes. If K_1 is negative as in the case of Ni, the [111] is the easy axis.

There are various means for measuring the magnetic anisotropy constant (see Ref.[47]). The most convenient method yet is to calculate it from the magnetization curve. The area that enclosed by the magnetization curve, the ordinate axis, and the line $M = M_s$ represents the energy required to magnetize a unit volume of the specimen to its saturation state. This energy can be also calculated from the increase of the anisotropy energy in this process, ΔE_a. For example, for uniaxial anisotropy, if we apply a magnetic field perpendicular to the easy axis (c-axis), the increase in the anisotropy energy (using Eq. 2.15 approximated by the K_1 term) is

$$\begin{aligned} \Delta E_a &= E_a(\theta = 90) - E_a(\theta = 0) \\ &= K_1. \end{aligned} \tag{2.17}$$

As has been discussed above, the magnetocrystalline anisotropy (more precisely, the effective or the macroscopic magnetocrystalline anisotropy) is produced through the interaction between the spontaneous magnetization and the crystal lattice, so that the temperature dependence of the spontaneous magnetization should give rise to a change in the effective magnetocrystalline anisotropy. Above the Curie temperature T_C, when the ferromagnetic order disappears the effective anisotropy vanishes, and the anisotropy constants goes to zero. However, a vanishing effective anisotropy for $T > T_C$ does not indicate that the microscopic anisotropy vanishes either, or that the underlying spin-orbit coupling is strongly varying with temperature [47, 52].

The effective anisotropy typically decreases more rapidly than the magnetic ordering upon an increase in the temperature. It has been demonstrated, both experimentally and theoretically, that the temperature behaviour of K_i depends on the magnetic symmetry of the system ([47] and references therein). When the anisotropy is expanded in spherical harmonics, $Y^l_m(\theta, \phi)$, the symmetry may be denoted by the lowest value of l needed to describe the phenomenon. The dependence of K_i on temperature is given as [53, 54]:

$$\frac{K_l(T)}{K_l(0)} = \left[\frac{M_s(T)}{M_s(0)}\right]^{\frac{l(l+1)}{2}}, \tag{2.18}$$

where M_s is the spontaneous magnetization of the system. The anisotropy for structures with uniaxial symmetry, as in the hexagonal crystal, can be expanded with an expression begin with terms having an l value of 2, while cubic symmetry requires the expression to begin with terms having $l = 4$.

2.3.2 Shape Anisotropy

Shape anisotropy, also referred to as magnetostatic anisotropy, results from the long-range magnetic dipole-dipole interaction. The dipole interaction energy Ω_{ij} between two magnetic moments $\boldsymbol{m}_i$ and $\boldsymbol{m}_j$ with mutual distance $\boldsymbol{r}_{ij}$ reads [47, 48]

$$\Omega_{ij} = \Omega_o \left(\frac{\boldsymbol{m}_i \cdot \boldsymbol{m}_j}{r^3_{ij}} - \frac{3(\boldsymbol{m}_i \cdot \boldsymbol{r}_{ij})(\boldsymbol{m}_j \cdot \boldsymbol{r}_{ij})}{r^5_{ij}} \right), \tag{2.19}$$

where Ω_o is a positive constant giving the strength of the interaction. The inherent anisotropic properties in the dipole-dipole interaction are exhibited by the explicit $\boldsymbol{r}_{ij}$

dependence. Eq. 2.19. reflects the potential energy which the magnetic moment $\boldsymbol{m}_i$ gains in the dipolar field of $\boldsymbol{m}_j$. In a macroscopic body the total field contribution of all moments which are localized outside a volume surrounding the moment $\boldsymbol{m}_i$ is assumed up by a continuous dipolar, or *demagnetizing*, field $\boldsymbol{H}_d$. Its strength and direction generally vary with position inside the sample but are often assumed to be constant (they are constant only inside an ellipsoid). For an arbitrary shaped sample, the demagnetizing field for a given direction of magnetization $\boldsymbol{M}$ relative to sample axes may be approximated as

$$\boldsymbol{H}_d = -N\boldsymbol{M}. \tag{2.20}$$

where the constant of proportionality, N, is called *the demagnetization factor* and, in general, it is shaped-dependent tensor with a trace of 1.

The magnetostatic-self energy generated by the demagnetizing field can be expressed as [47, 48]

$$E_d = -\frac{\mu_o}{2V}\int \boldsymbol{H}_d \cdot \boldsymbol{M} dv, \tag{2.21}$$

where μ_o is the magnetic permeability of vacuum, V is the volume of the specimen. If the specimen is in the form of an ellipsoid with semi-major axis parallel to the z-axis, the demagnetization factor along the x- and y-axes is given by $N_{xx} = N_{yy} = \frac{1}{2}(1-N_{zz})$, where N_{zz} is the demagnetization factor along the z-axis. Let the magnetization vector makes an angle θ with the z-axis, we have then the magnetostatic self-energy of the body as

$$\begin{aligned} E_d &= \frac{1}{2}\mu_0 M^2 N_{zz} + \frac{1}{2}\mu_0 M^2 (N_{xx} - N_{zz}) \sin^2\theta \\ &= \frac{1}{2}\mu_0 M^2 (N_{xx} - N_{zz}) \sin^2\theta + \mathit{constant}. \end{aligned} \tag{2.22}$$

This expression of the magnetostatic energy has an angle-dependent term of exactly the same form as the leading term of the uniaxial magnetocrystalline anisotropy energy of Eq. 2.15. The long axis of the specimen plays the same role as the easy axis of the crystal, and shape anisotropy constant K_a is given by

$$K_a = \frac{1}{2}\mu_0 M^2(N_{xx} - N_{zz}). \tag{2.23}$$

Considering only the magnetostatic self-energy, according to Eq. 2.22 the ellipsoidal-shaped specimen will prefer to be magnetized along its long axis, z-axis. Thus shape alone can be a source of magnetic anisotropy.

Thin magnetic film with its normal vector parallel to z-axis represents the limit of a plate of infinite lateral extension. This condition yield the simple demagnetization factor with all tensor elements are zero except for the direction parallel to z-axis. Hence, the magnetostatic self-energy of homogeneously magnetized thin film reads

$$E_d = -\frac{1}{2}\mu_o M^2 \sin^2\theta + constant, \tag{2.24}$$

where θ is the angle between the z-axis and the direction of the magnetization $\boldsymbol{M}$. Obviously, $\theta = \pi/2$ minimize the magnetostatic energy of Eq. 2.24. Hence, in-plane orientation of the magnetization is favoured. Therefore, perpendicular anisotropy of thin magnetic films requires additional crystalline contributions as will be discussed in section 2.6.3

2.4 Band Magnetism

Ferromagnetism

The Heisenberg model of ferromagnetism of Eq. 2.6 is a phenomenological approach based on the localized moment approximation. It is well suited to describe the ferromagnetism of mostly localized electrons found in materials such as 3d metal oxides and their compounds. Although it contains many important insights into magnetic behaviour of 3d transition metals, it is not suitable to describe its magnetic properties at low temperature ($T \approx 0$). In the 3d transition magnetic metal (Fe, Co, Ni),

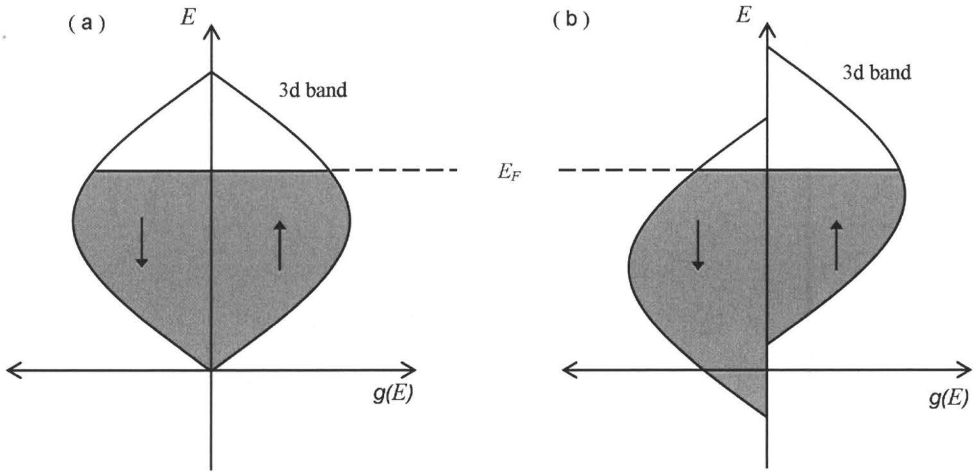

Figure 2.2: *Density of state of spin-up and spin-down electrons for 3d transition metal. In case of magnetic material, the spin-up and spin-down bands are exchange-split as shown in (b). This shows the validity of stoner criterion. In (a) a non-magnetic band structure is shown (after [57])*

the electrons which carry the magnetic moments are delocalized (*itinerant*). This means that the magnetic interaction is between the electrons in the delocalized band states. Therefore, ferromagnetism of 3d transition metals is usually modeled by band structure calculations. The band model of ferromagnetism was introduced by Stoner [55, 56], and describes much of the physics of basic magnetism at low temperature.

Assuming the band theory of metal is understood, the Stoner model can be explained as follows. Electrons have an intrinsic magnetic moment due to their spin. This spin is quantized along an axis and the projections on this axis are often referred as to spin-up and spin-down. In a 3d transition metal, itinerant electrons form the conduction 3d band which can be imagined to be divided up into two half-bands. One is for those electrons with spin-up direction called spin-up band, and the other, the spin-down band is for electrons with spin-down direction. Starting with the non-magnetic band structure, spin-up and spin-down band contains an equal number of spin-up and spin-down electrons as in Fig. 2.2a. This is to reduce the total kinetic energy. There is a reduction in the exchange energy if the electron spins align but this is also leads to an increase in the kinetic energy of the electrons. The kinetic energy increases because, if the electron spins align, the Pauli exclusion principle does not permit two electrons to occupy the same kinetic energy state. Whether the 3d metal is a ferromagnetic or not depends on the balance between the gain in kinetic energy and the reduction in exchange energy as a result of spin alignment. The Stoner criterion for ferromagnetism is a statement of this balance:

$$Ig(E_F) \geq 1, \tag{2.25}$$

where I, the exchange integral (also known as the Stoner parameter); $I_{i,j}$ has no classical interpretation. Quantum mechanically, it is a measure of the Coulomb interaction between two electrons of the same spin in the two states $\varphi_i(\mathbf{r}_i)\varphi_j(\mathbf{r}_j)$ and $\varphi_i(\mathbf{r}_j)\varphi_j(\mathbf{r}_j)$ (see Eq. 2.13). $g(E_F)$ is the density of states of the electrons at the Fermi energy level which is a measure of the increase in the total kinetic energy of the electrons if the electrons spin is allowed to align. This is because the increase in the kinetic energy is greater as the states in the band are spread over energy range, that is, if the density of state $g(E)$ is small. Therefore, ferromagnetism is favoured in systems with strong exchange integrals and large state densities at the Fermi energy.

The saving in exchange energy appears as a split in the energy of the spin-up and spin-down bands as shown in Fig. 2.2b. The average magnetic moment per atom is then evaluated as

$$\mu = \mu_B(N \downarrow - N \uparrow), \tag{2.26}$$

where $N \uparrow$ and $N \downarrow$ is the number of electrons in spin-up and spin-down band respectively. At this point, it is worth to mention that the Stoner model of ferromagnetism also explains the observed fractional magnetic moment of 3d transition metal. Calculated values of magnetic moments per atom for various elements are shown in Table 2.1.

Magnetocrystalline Anisotropy

Within the model of itinerant electrons, the magnetocrystalline anisotropy is explained as a modification to the band structure induced by the spin-orbit coupling. Spin-orbit coupling can be interpreted as the coupling between the spin of an electron and the magnetic field created by its own orbital motion around the nucleus. The orbital motion is coupled to the lattice via the crystal electric field that takes on the symmetry of the lattice itself. For a ferromagnetic 3d transition metal, some of the electronic states in the 3d-band are degenerate near the Fermi surface, most often at high symmetry points in the lattice [58]. Spin-orbit coupling lifts this degeneracy. The splitting of the degenerate states at the Fermi level decreases the density of the state at Fermi surface and increases the density of state below the Fermi level. Hence, the total energy of the electrons decreases. The amplitude of the band splitting depends on the spin direction which is locked by the direction of the electron orbital which in turn is determined by the crystal field [58]. The direction in which the spin-orbit coupling produces the maximum splitting and thus the minimum system energy gives rise to the easy axis.

2.5 Ferromagnetic Domains

The concept of magnetic domains was postulated at the beginning of the last century by Weiss [49]. He was the first to connect two observation that are unique to ferromagnetic materials, namely (*i*) a huge magnetization as a response to a small external magnetic field, and (*ii*) a remnant magnetization which may or may not vanishes, depending on the magnetic history of the sample. These observations were the key ingredients in the postulate that a ferromagnetic material in zero external magnetic field is usually divided into regions with full magnetization, with the direction of this spontaneous magnetization varying from region to region. These regions

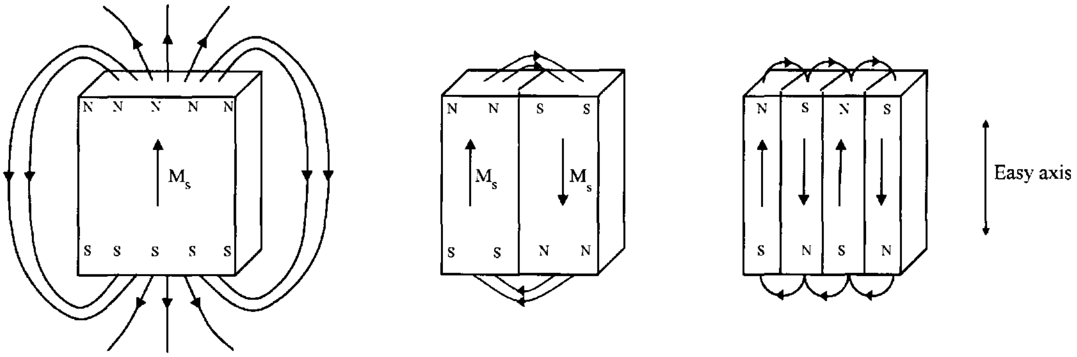

Figure 2.3: *Division into domains: The sample divides up into domains in order to reduce the magnetostatic-self energy stored in the external stray magnetic field. The arrow indicates the direction of the magnetization in each domain.*

are called domains and the boundary between two domains is called a domain wall.

2.5.1 The Origin of Domains

The reason for the creation of domains is the attempt to reduce the magnetostatic self-energy of the sample. As discussed earlier in Sec. 2.3.2, the magnetostatic self-energy results from the interaction between the sample magnetization **M** and the dipolar field $\mathbf{H}_d$. Figure 2.3a shows a single crystal of a uniaxial anisotropy, spontaneously saturated to the easy axis. The magnetostatic energy of this crystal is $\propto \int H_d^2 dv$, evaluated over all space where $\mathbf{H}_d$ is appreciable. This considerable energy can be reduced approximately by a factor of two, if the crystal splits into two domains magnetized in opposite direction as in Fig.2.3b. This is because of the reduced spatial extension of the dipolar field [46, 47]. The magnetostatic energy will be reduced further, if the crystal splits into four domains as in Fig.2.3c, and so on. But the exchange energy in ferromagnetic material is minimum only when the adjacent spins are parallel. Therefor, the domains will continue to form until the decrease in magnetostatic energy is balanced by the increase in the exchange energy, and thus, the size of domains is determined by this balance.

2.5.2 Domain Wall Structure

As has been mentioned out above, the division into domains is at the expense of exchange energy which is stored in the domain walls. The size of domain walls depends on the balance between the exchange energy, which forces the atom spins to align, and the magnetocrystalline anisotropy energy which forces the spins to align along the crystal easy axis. For a hexagonal crystal, within one domain all spins align along the easy axis, namely the c-axis. In an adjacent domain the spins would be reversed, pointing in the opposite direction but still along the c-axis. This situation cost much exchange energy which tries to align the spins. There is a balance; the exchange energy tries to make the wall as wide as possible, in order to make the angle between adjacent spins as small as possible, and the anisotropy energy tries to make the wall as thin as possible, in order to reduce the number of spins pointing away from the easy axis. As a results of this competition, the wall has a certain finite width and a certain structure. Because the spins in the domain wall are not quite parallel to one another and not parallel to the easy axis, the domain wall also has a certain energy per unit area of its surface.

As a simple illustration, one can make an approximated calculation of domain wall width and energy in a hexagonal crystal with an uniaxial anisotropy as follows [59]. Figure. 2.4 shows a schematic diagram of a domain wall. The exchange energy per unit area of the wall is

$$\begin{aligned} \sigma_{ex} &= -2J\sum_{i,j} \boldsymbol{S}_i \cdot \boldsymbol{S}_j = -2JS^2\sum_{i,j}\cos(\phi_{ij}) \\ &\approx -2JS^2 + JS^2\sum_{i,j}\phi_{ij}^2, \end{aligned} \tag{2.27}$$

where J is the exchange integral, $\boldsymbol{S}_i$ is the spin of the ith atom and the sum is carried out for only nearest neighbors and the angle ϕ_{ij} is a small angle between the spins of adjacent atoms which varies nonuniformly along an axis normal to the wall surface,

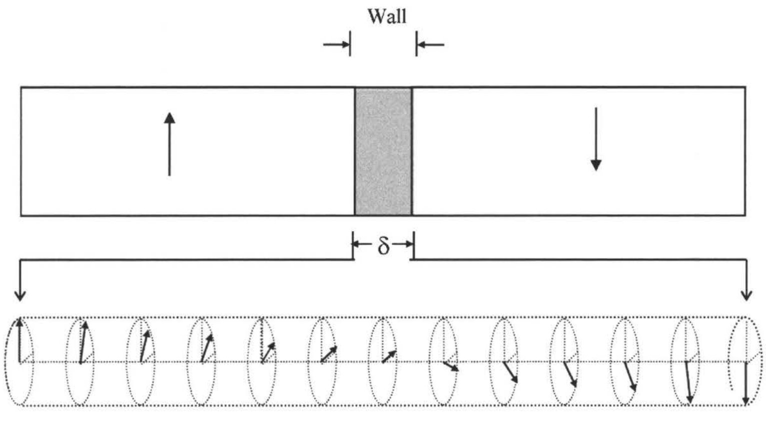

Figure 2.4: *Structure of a 180° Bloch wall in a uniaxial crystal.*

say the x-axis. The first term of Eq. 2.27 is the reduction in energy achieved by the ferromagnetic alignment but the second term is the extra energy because within the wall adjacent spins are tilted by an angle ϕ_{ij}. If we write $\phi_{ij} = a\ \partial\phi/\partial x$, where a is the interatomic distance, then the exchange energy per atom is $JS^2a^2\ (\partial\phi/\partial x)^2$. Accordingly, the total exchange energy stored in a unit area of the wall is

$$\sigma_{ex} = \frac{nJS^2}{a}\int_{-\infty}^{+\infty}\left(\frac{\partial\phi}{\partial x}\right)^2 dx = A\int_{-\infty}^{+\infty}\left(\frac{\partial\phi}{\partial x}\right)^2 dx, \tag{2.28}$$

where n is the number of atoms per unit cell and $A(= nJS^2/a)$ is the exchange stiffness constant. As a first approximation, we assume that the wall has an effective width, δ, and the angle ϕ varies uniformly from 0 to 180^o. Therefore, the exchange energy per unit area of the wall becomes

$$\sigma_{ex} = A\int_{0}^{\delta}\left(\frac{\partial\phi}{\partial x}\right)^2 dx = \frac{A\pi^2}{\delta}. \tag{2.29}$$

If the uniaxial anisotropy energy per unit volume is described phenomenologically as $K_u \sin^2\phi$, then the total anisotropy energy per unit wall area is

$$\begin{aligned}\sigma_a &= \int_0^{\delta} K_u \sin^2\phi\, dx \\ &= \frac{K_u\delta}{2},\end{aligned} \tag{2.30}$$

where K_u is the anisotropy constant. Therefore, the total energy per unit area of a domain wall in a hexagonal crystal is

$$\sigma_{DW} = \sigma_{ex} + \sigma_a = \frac{A\pi^2}{\delta} + \frac{K_u\delta}{2}. \tag{2.31}$$

The minimum total energy is achieved for a wall width

$$\delta = \pi\left(\frac{2A}{K_u}\right)^{1/2} \approx \pi\left(\frac{A}{K_u}\right)^{1/2}, \tag{2.32}$$

and thus, the total energy of the wall per unit area in the equilibrium state is

$$\sigma = \pi\sqrt{2AK_u} \approx 4\sqrt{AK_u}. \tag{2.33}$$

In above illustration, the domain wall is assumed to separate domains whose magnetization are in the opposite directions, and is called a 180° wall. There are other type of domain walls such as a 90° wall separating domains whose magnetization make a 90° angle.

From above discussion, one can conclude that whether or not a domain forms at all depends on a balance of the increase in wall energy with the reduction in the magnetostatic self-energy. However, the balance between the exchange energy and the magnetocrystalline anisotropy determine the width of the domain walls. The exchange energy tries to keep the wall width large to allow only a small variation of the angles between adjacent spins, while the magnetocrystalline anisotropy favours an abrupt changes of spin directions since it tries to lock the spins along the easy axis.

2.5.3 Bloch Wall and Néel Wall

In the above discussion, the spin in the domain wall is assumed to rotate such that it always remains parallel to the plane of the wall as in Fig. 2.4. This type of domain wall is called a Bloch wall, after Bloch who first investigated the spin structure of

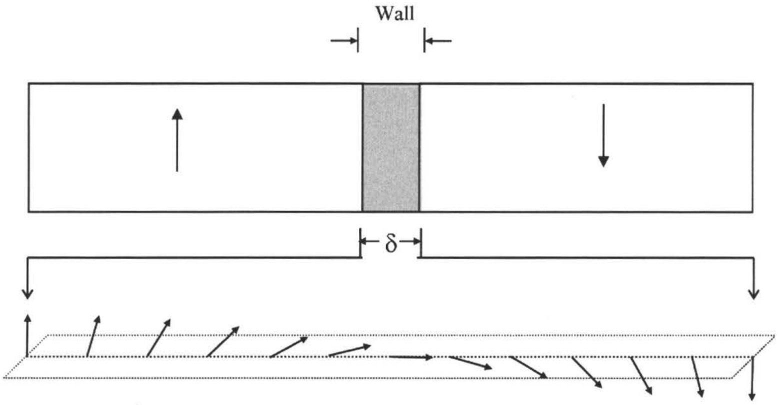

Figure 2.5: *Structure of a 180° Néel-wall in a uniaxial crystal.*

the domain walls [60]. The total energy per unit area σ_{DW} of a Bloch wall is not a constant of the material but depends also on the thickness of the sample. The above calculation assumes no magnetostatic energy contribution to the domain wall energy. However, the wall structure contains a non-zero component of the magnetization on the sample surface where the wall terminates (wall external surface), and the energy of the resulting surface magnetic poles must be taken in account. In a thick sample, where the sample thickness d is larger than the wall width δ, the magnetostatic energy due to the free magnetic poles on the wall external surface is negligible relative to the usual exchange and anisotropy energy. It should be clear from Sec. 2.3.2 that as the sample thickness decreases, the magnetostatic energy, and so the total energy, of a Bloch wall that extends through the thickness of the sample increases as a result of the free magnetic poles at the top and bottom surfaces of the wall [47, 48, 61] (see Fig.2.6). Therefore, in the case of a very thin sample such as thin film in which $d < \delta$, the magnetostatic energy of the wall can be reduced if the spin, while rotating, remains parallel to a plane normal to the wall as in Fig. 2.5. The result is a Néel wall. Then, a smaller magnetostatic energy at the internal surface of the wall is accepted as the price of removing the larger magnetostatic energy at external surface [47, 48, 61].

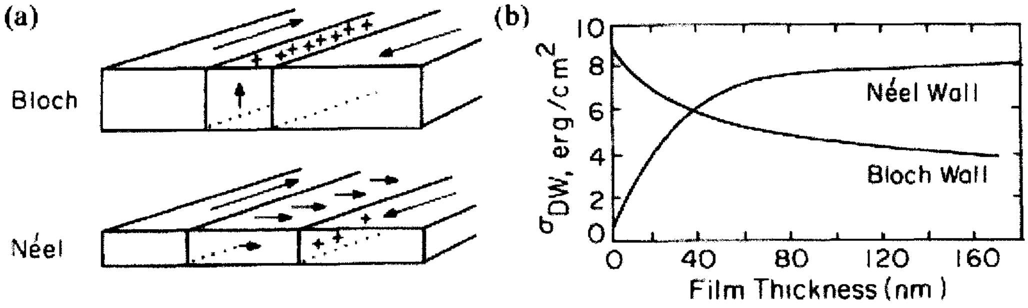

Figure 2.6: *(a) A schematic representation of Bloch wall, top, with charged surfaces on the external surfaces of the sample and Néel wall, bottom, with charged surfaces internal to the sample. (b) Domain wall energy (σ_{DW}) of Bloch and Néel walls as a function of the film thickness (from [48]).*

The Néel wall energy (including the magnetostatic energy) decreases with decreasing film thickness because it is proportional to the area of the wall internal surface inside the film (see Fig. 2.6). For a film with an intermediate thickness $d \approx \delta$, the energies of Bloch and Néel wall are comparable. In this case a new kind of domain wall called the cross-tie wall appears and it is composed of a mixture of Bloch and Néel walls [47, 48].

2.6 Magnetism Of Ultrathin Films

In ultrathin films, a significant fraction of film is occupied by atoms at the surface, or at the film/substrate interface. The most obvious difference between atoms at a surface and atoms in the bulk is that the surface atoms have no neighbouring atoms on one side. This reduction in symmetry may cause a significant modification of magnetic properties at surfaces and interfaces from those in the same bulk material. As a results, ultrathin films can show characteristic features that do not exist for bulk materials. Of these, we discuss the magnetic ordering behaviour in two-dimensional system, the modification of magnetic moments at surfaces and interfaces, and the magnetic surface anisotropy (MSA) that arise from the broken symmetry at the surfaces of the film. Later, we will discuss an interesting phenomena driven by the surface anisotropy, namely, a stripe domain structure (SDS) in ultrathin films with perpendicular magnetic anisotropy (PMA).

2.6.1 Magnetic Ordering in Two-Dimensional System

One of the most fundamental quantities in magnetism is the spontaneous magnetization M_s, and especially its temperature dependence

$$M_s = M_s(T=0)\left(1 - \frac{T}{T_C}\right)^{\beta}, \tag{2.34}$$

where β is the critical exponent that describes the second-order phase transition from the ferromagnetic to the paramagnetic phase, and T_C is the transition Curie temperature where the spontaneous magnetization vanishes. Statistical mechanics predicts different values of β depending on the dimensionality of the system and the degrees of freedom of the spin. Hence, β is different in 3D bulk, at a surface or in an ultrathin film. In the Heisenberg model, the orientation of the spins is not restricted. The predicted value of β for 3D-Heisenberg model is about 0.367 while it is 0 for the isotropic 2D-Heisenberg model (no long range order at finite temperature, as shown by the *Mermin-Wagner theorem* [62]). In the XY model, the spin orientation is confined in a plane. In this case, $\beta \approx 0.35$ for 3D system and $\beta \approx 0.24$ for finite-size 2D system. In the case of Ising model, where the spins are restricted to point either up or down, the predicted β values are 0.325 for a 3D system and 0.125 for 2D system.

Experimental measurements of critical exponents β of ultrathin films have shown that most of ultrathin films can be described by 2D Ising-like systems [63–65] or 2D XY-like systems [66, 67]. Further more, Li and Baberschke [68] have shown that a dimensional crossover from a 2D Ising system ($\beta \approx 0.125$) to a 3D Ising system ($\beta \approx 0.325$) takes place upon increasing the film thickness from 5 ML to 7 ML of Ni(111) on a W(110) substrate.

2.6.2 Magnetic Moments At Surfaces and Interfaces

As discussed in section 2.4, itinerant magnetism leads to a magnetic moment that is determined by the electronic band structure. A positive exchange interaction splits the valance band into a majority band and minority band. The difference in the number of occupied states between these two bands gives rise to the average magnetic moment per atom (Eq. 2.26). The most important quantity that determines the amplitude of the band splitting, and hence the strength of the magnetic moment, is the density of states $g(E)$ close to the Fermi level. For 3d-transition metals, the density of states close to the Fermi energy is dominated by the contribution of the d band. As a first approximation, the density of states of the d band is inversely proportional to the band width [59]:

$$g \sim \frac{1}{W_d}, \tag{2.35}$$

The band width W_d is determined by the overlap between the d orbitals of adjacent atoms. This width can be described within the nearest-neighbour tight-binding approximation as [59]:

$$W_d = \sqrt{z}h, \tag{2.36}$$

where z is the number of nearest neighbours and h is the hopping integral, which is a measure of the overlap.

At a surface the number of nearest neighbours is reduced. For example in a bulk fcc material z is 12, but at a (111) surface it is 9, at the (100) surface it is only 8, while at the (110) surface it is 7. If one grows a monolayer on a non-transition metal substrate the number of magnetic nearest neighbours is reduced even further, to 6 for (111), to 4 for (100) and to only 2 for a (110) surface. Thus, the local density of states is narrower at the surface or in a monolayer than in the bulk. If the Fermi energy

Table 2.1: *Calculated magnetic moments (in Bohr magneton μ_B) in the bulk, at the surface and at the interface (from [69])*

Metal	Bulk	Surface	interface	Atom
bcc V	0.00	0.00	2.87	3.0
bcc Cr	0.59	2.49	3.84	4.0
bcc Fe	2.25	2.98	3.20	4.0
hcp Co	1.64	1.76	1.89	3.0
fcc Ni	0.56	0.68	1.02	2.0

is not too close to the edge of the band, this will lead to an increase in $g(E_F)$ and hence, an increase in the magnetic moment of the 3d-transition metals at surfaces and at film/substrate interfaces. Furthermore, while V and Pd in bulk fail to satisfy the Stoner criterion, it is possible they satisfy it when they are in monolayer or next to a ferromagnetic layer at the interface. The calculated values of the magnetic moment per atom are summarized in Table 2.1 for various elements and environments.

2.6.3 Magnetic Surface Anisotropy

As has been pointed out above, the translational symmetry at ultrathin film surfaces is broken in the direction of the film normal. This can give rise to a uniaxial anisotropy. This anisotropy is called the magnetocrystalline surface anisotropy. Néel has discussed this surface anisotropy within a phenomenological model of the magnetocrystalline anisotropy. In this model, the pairwise interactions between neighbouring atomic magnetic moments separated by a vector $\boldsymbol{r}$ reads [70]:

$$E(r) \sim l(r)\cos^2\phi + q(r)\cos^4\phi, \tag{2.37}$$

where $l(r)$ and $q(r)$ are expansion coefficients and ϕ is the angle between a line joining the atoms that are distance r apart, and the parallel magnetic moments of the two atoms considered. Using this model, he derived the surface anisotropy energy for fcc

(111) and fcc (100) surfaces as [70]

$$E_s = -K_s \sin^2\theta, \tag{2.38}$$

where K_s, the surface anisotropy energy per unit surface area, is different for (111) surface from that for (100) surface. Here θ is the angle between the magnetization and the surface normal. In case of positive K_s the surface anisotropy favours the magnetization to lie in the film plane, while if K_s is negative it favours *an easy axis perpendicular* to the film plane.

Owing to the different atomic environments, the magnetocrystalline anisotropy in thin films has two parts: a bulk magnetocrystalline anisotropy for interior atoms and surface magnetocrystalline anisotropy for the surface atoms. In cubic materials the bulk anisotropy vanishes to fourth order, however, at surface the broken symmetry brings the second order anisotropy term into play. Therefore, the surface magnetocrystalline anisotropy could be much larger than the bulk contribution in very thin films.

In a ferromagnetic ultrathin film, the anisotropy energy, per unit volume, can very often be written in an expression where the bulk and the surface anisotropy are treated separately as [71]

$$E_{an} = -\left(K_a + \frac{2K_s}{d}\right)\sin^2\theta + K_v(\theta,\phi), \tag{2.39}$$

where d is the film thickness, K_a is the shape anisotropy constant[1] per unit volume and K_v is the effective bulk (volume) magnetocrystalline anisotropy constant per unit volume. K_s is the surface anisotropy constant per unit of the surface area, and the factor of 2 includes both the top and bottom surfaces. $(K_a + 2K_s/d)$ is usually called the effective perpendicular magnetic anisotropy (PMA) constant K_{eff}. In this way K_{eff} is an explicit function of film thickness. It is possible the lowest-energy state for the

---

[1] see Eq. 2.24 in sec.2.3.2; $K_a = \frac{1}{2}\mu_0 M^2$

magnetization may change with film thickness. For example, from out-of-plane when K_{eff} is negative to in-plane when K_{eff} becomes positive. This phenomena is known as a *spin reorientation transition* (SRT) [10]. On the other hand the anisotropy constants are a function of a number of parameters such as temperature, chemical composition and stress. Hence, a spin reorientation transition could occur by changing one of these parameters at constant film thickness. Spin reorientation transitions and perpendicular magnetic anisotropy have been observed for a number of ultrathin films (see for example ref.[3] and references therein).

2.7 Magnetic Domain Structure in Ultrathin Films with Perpendicular Anisotropy

When the perpendicular magnetic anisotropy (PMA) is strong enough to hold the magnetic moments perpendicular to the film plane, the dipole-dipole interaction is effectively antiferromagnetic and favours the formation of a domain structure. This was first predicted by Yafet and Gyorgy [72], who found that *a stripe domain structure* (SDS) with alternating up and down domains, is energetically favourable compared to other states. While Czech and Villain [73] later have argued that the checkerboard configuration has even lower energy, it has been confirmed that the stripes have the lowest energy [14–16, 21, 22].

At low temperature, the domains are oriented along a common crystallographic axis in the *ordered stripe* domain phase. Others [14–16] refer to this phase as the *smectic* phase in analogy with a phase in liquid crystals, or *true stripe-domain* phase. In this phase there are different types of dislocations in the domain structure that results in an algebraic decay in the positional order [14–16]. At higher temperature, the domains lose their long-range positional order by the proliferation of dislocations but retain their long-range orientational order. This new phase is referred to as *an Ising nematic* phase [14–16]. At even higher temperature, mutually perpendicular stripe domains appear. This is known as *a tetragonal* phase because of the absence of the long-range orientational order [14–16]. In this study, we refer to the Ising nematic and the tetragonal phases as the *delocalized* phases. A further increase in the temperature drives the film to the paramagnetic phase. This is possible if the Curie temperature is lower than the temperature at which a spin-reorientation transition from the out-of-plane state to the in-plane state takes place.

The stripe domain density $n(T)$ (*the total numbers of domain walls per unit length*) is determined by the balance of the magnetostatic self-energy gained due to domain formation against the energy required to create the domain walls, E_w. (The domain walls are Bloch walls, not Néel walls, so the wall magnetization runs along the wall length with no cost in magnetostatic energy. Néel walls are preferred only in thin films exhibiting in-plane magnetization). A number of authors have calculated the resulting domain density [14–16, 21, 22, 72]. Kashuba and Pokrovsky [14, 15] have calculated the equilibrium domain density n for a spin-continuum model of a monolayer film as follows. The total Hamiltonian of a two-dimensional (2D) ferromagnet reads [14, 15]:

$$\begin{aligned}\mathcal{H} &= \Gamma_s \int [\nabla \cdot \boldsymbol{n}(\boldsymbol{r})]^2 d^2r - K_s \int n_z^2 d^2r \\ &+\frac{\Omega_s}{8\pi} \int\int \frac{\boldsymbol{n}(\boldsymbol{r}) \cdot \boldsymbol{n}(\boldsymbol{r}') - 3(\boldsymbol{v} \cdot \boldsymbol{n}(\boldsymbol{r}))(\boldsymbol{v} \cdot \boldsymbol{n}(\boldsymbol{r}'))}{|\boldsymbol{r} - \boldsymbol{r}'|^3} d^2r d^2r', \qquad (2.40)\end{aligned}$$

where the spin-field $\boldsymbol{n}(\boldsymbol{r})$ is the continuum analog of the discrete spin lattice $\boldsymbol{S}_i$ with lattice constant a. $\Gamma_s = (1/2)\gamma S^2 J$ is the exchange energy (γ denotes the number of nearest neighbours, J the exchange constant, and S the spin per atom), and K_s is the single-ion anisotropy which includes the contribution from the surface anisotropy. The third term in the Hamiltonian of Eq. 2.40 represents the dipole interaction of strength $\Omega_s = \mu_0(g\mu_B a^{-2} S)^2$ (g denotes the Lande$'$ factor, μ_B the Bohr magneton). Here $\boldsymbol{v}$ is a unit vector along the direction of $(\boldsymbol{r} - \boldsymbol{r}')$. The total energy of domain formation *per unit area of a monolayer film*, assuming a ferromagnetic state with alternating up and down stripes reads [14–16]:

$$E = E_s n - \frac{\Omega_s}{\pi} n \ln(\frac{2}{\pi l n}), \tag{2.41}$$

where $n = 1/L$ is the domain density (see its definition above), and L is the domain width. The first term of Eq. 2.41 represents the energy cost per unit area due to domain wall creation with domain wall energy $E_s = 4[\Gamma_s K_{\text{eff}}]^{1/2}$ per unit *length* and domain wall thickness $l = \pi[\Gamma_s/K_{\text{eff}}]^{1/2}$. Here $K_{\text{eff}}(= K_s - \Omega_s/a)$ is the effective anisotropy that includes a contribution from the short range part of the dipole interaction [14–16]. The second term represents the energy gained due to domain creation which is the difference between the dipole energy of the stripe domain structure and the dipole energy of the single domain state [14]:

$$E_d = -\frac{\Omega_s}{\pi} \sum_{m,n} \int_{(2m)L+l}^{(2m+1)L-l} dx \int_{(2n-1)L-l}^{(2n)L-l} dx' \int_{-L_y/2}^{L_y/2} dy \int_{-L_y/2}^{L_y/2} dy' [(x-x')^2 + (y-y')^2]^{-3/2}, \tag{2.42}$$

where L_y is the length of the film in the y-direction that is directed parallel to the domain walls. The equilibrium domain density can be calculated by the minimization of total energy of Eq. 2.41 with respect to n, as done in ref.[14–16]. This yields

$$n_{\text{eq}}(T) = \frac{2}{\pi l} \exp\left(-\frac{\pi E_s}{\Omega_s} - 1\right). \tag{2.43}$$

This result can be generalized for a thin film with thickness $d = Nb$, where N is the number of layers separated by out-of-plane lattice constant b [16, 37]. In this case, the total energy *per unit volume* of the film is given by [14–16]:

$$E = E_w n - \frac{\Omega d}{\pi} n \ln(\frac{2}{\pi l n}), \tag{2.44}$$

where $E_w = 4[\Gamma K_{\text{eff}}]^{1/2}$ is the domain wall energy per unit *area*. Here $\Gamma = \Gamma_s/b$ is the exchange stiffness and $K_{\text{eff}}(= K_s/d - \Omega)$ where $\Omega = \Omega_s/b^2$. The corresponding equilibrium domain density is then [14–16]:

$$n_{\text{eq}}(T) = \frac{2}{\pi l} \exp\left(-\frac{\pi E_w}{\Omega d} - 1 \right). \tag{2.45}$$

2.8 Magnetic ac-Susceptibility of Ultrathin Films with Perpendicular Anisotropy

The magnetic susceptibility (χ) of a magnetic ultrathin film with a stripe domain structure results from the growth of one domain type, say by δ, at the expense of the other one when a magnetic field H is applied perpendicular to the film (Fig. 2.7). Abanov *et al.*[16] have calculated the average magnetization M which results from the difference in up and down domain widths, $L + \delta$ and $L - \delta$. L is interpreted in the present circumstance as the average stripe width. The averaged magnetization can then be calculated as [16]

$$M = M_{sat} \frac{(L+\delta) - (L-\delta)}{(L+\delta) + (L-\delta)} = M_{sat} n(T,H)\delta, \tag{2.46}$$

where $n(T,H)$ is the domain density when a magnetic field H is applied and $M_{sat}(= g\mu_B S/a^2 b)$ is the saturation magnetization. The total energy per unit film of the film with stripe domain structure reads [14–16]:

$$E = E_w n - \frac{\Omega d}{\pi} n \ln\left(\frac{2}{\pi l n} \cos(\frac{\pi n \delta}{2}) \right) - \mu_0 H M_{sat} n \delta, \tag{2.47}$$

where the last term represents the Zeeman energy. In this case, the magnetic state is in equilibrium if [14–16]:

$$\begin{aligned} n_{\text{eq}}(T,H) &= n_{\text{eq}}(T)\sqrt{1 - \left(\frac{H}{H_c}\right)^2} \\ \delta &= \frac{2}{\pi n_{\text{eq}}(T,H)} \sin^{-1}\left(\frac{H}{H_c}\right), \end{aligned} \tag{2.48}$$

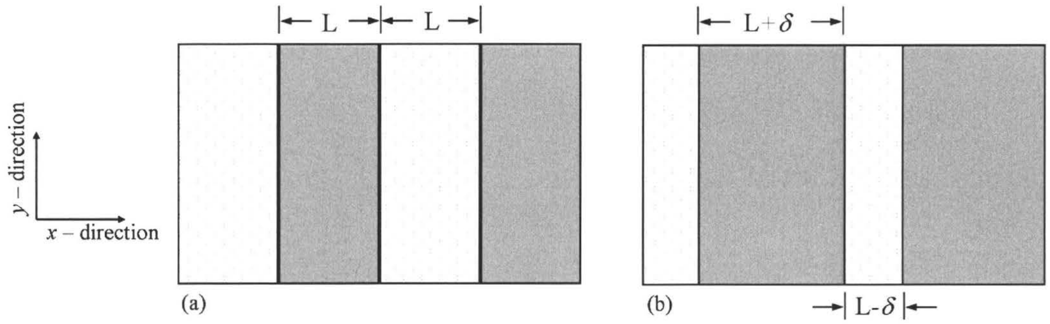

Figure 2.7: *A schematic representation of stripe domain structure in a ferromagnetic film in the absence of a magnetic field (a) and when a magnetic field is applied (b). In (a) the up and down domains have equivalent width L, while in (b) the applied filed causes domains with their spins parallel to the applied field (dark) to grow by an amount δ at the expense of the antiparallel domains (white)*

where H_c is the magnetic field required to drive the film to a single domain state. It is defined as

$$H_c = \frac{\Omega d}{2\mu_0 M_{sat}} n_{\text{eq}}(T). \tag{2.49}$$

At the equilibrium, the average magnetization is then expressed as

$$M^{\text{eq}} = \frac{2M_{sat}}{\pi} \sin^{-1}\left(\frac{H}{H_c}\right), \tag{2.50}$$

and the equilibrium susceptibility is then obtained by the derivative of Eq. 2.50 with respect to the applied field H at the limit $H \ll H_c$ as

$$\chi^{\text{eq}}(T) = \frac{4}{\pi d n_{\text{eq}}(T)} = \frac{2l}{d} \exp\left(\frac{\pi E_w}{\Omega d} + 1\right). \tag{2.51}$$

In a real system, defects in film structure such as inhomogeneities in film thickness [37, 38, 43] can serve to pin the domain walls. The domain wall motion between two pinning sites is thermally activated process with a relaxation time τ_a that follows an Arrhenius law [43]:

$$\tau_a(T) = \tau_{0a} \exp(\frac{E_a}{k_B T}), \tag{2.52}$$

where τ_{0a} is a constant and E_a is the activation energy that represents the height of a one-dimensional energy barrier. Hence, when applying a magnetic field H perpendicular to the film, the domain walls do not respond instantaneously but rather, on average, they move toward the equilibrium state with a relaxation time τ_a. In this case, the resulting magnetization relaxes toward equilibrium according to [43]

$$\frac{\partial M(t)}{\partial t} = \frac{-1}{\tau_a}\left(M(t) - M^{\mathrm{eq}}\right), \tag{2.53}$$

where t is the time and M^{eq} is the equilibrium value of magnetization. By assuming $M^{\mathrm{eq}} = \chi^{\mathrm{eq}} H(t) = \chi^{\mathrm{eq}} H_0 e^{i\omega t}$, and $M(t) = M_0 e^{i\omega t}$, Arnold *et al.* [42] and others [37, 38] have found that the measured magnetic ac-susceptibility is expressed as:

$$\chi(T) = \frac{M_0}{H_0} = \frac{1 - i\omega\tau_a(T)}{1 + \omega^2\tau_a^2(T)}\chi^{eq}(T), \tag{2.54}$$

where ω is the driving frequency of the applied field. This result can be generalized to a distribution of E_a [39, 43]. In an ultrathin film with perpendicular anisotropy, the activation energy E_a has been attributed to the variation in domain wall thickness at monolayer steps, which in turn results in a variation in domain wall energy [37, 38, 43]:

$$E_a = \frac{\xi d}{E_w}\left(\frac{\Delta E_w}{\Delta d}\right)^2, \tag{2.55}$$

where d is the film thickness, and ξ is the mean separation of pinning sites (monolayer steps). Assuming the magnetic anisotropy is dominated by the surface term K_s/d, the above equation can be rewritten in term of the film thickness as

$$E_a = \xi\sqrt{\Gamma K_s} d^{-3/2}. \tag{2.56}$$

Figure. 2.8 shows the real part of a typical ac-susceptibility measured from an ultrathin Fe film deposited on top of 2 ML Ni/W(110). The real part of the susceptibility exhibits a broad peak at the temperature T_p where $\omega\tau_a(T_p) \approx 1$. In the high temperature range where $T > T_p$, domains are freely moving and the susceptibility falls off due to the exponential increase in domain density in $\chi^{eq}(T)$. In the low

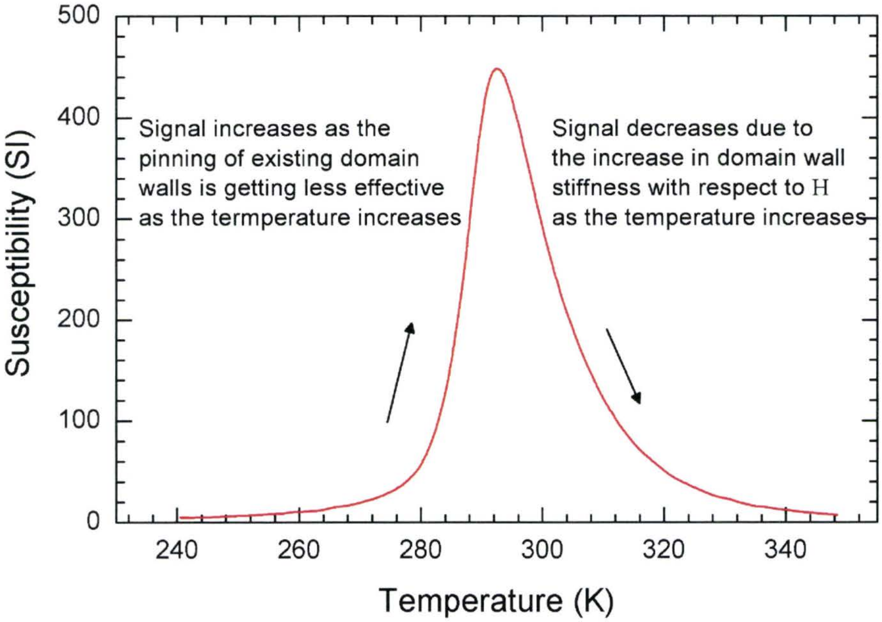

Figure 2.8: *Typical susceptibility measurement from ultrathin Fe film deposited on top a 2 ML Ni/W(110) substrate.*

temperature range where $T < T_p$, the susceptibility falls off due to the exponential increase in the relaxation time in the dynamical factor $(1 + \omega^2\tau_a^2)^{-1}$.

The precise dependence of $\chi^{\rm eq}(T)$ on temperature is controlled by $K_{\rm eff}$; this makes it very difficult to calculate from first principles. However, analysis of a large number of measurements of the real part of the susceptibility from ultrathin films with perpendicular magnetization have shown that at high temperature where $\omega\tau_a(T) \ll 1$, the variation of domain density and susceptibility is well described by [37–39, 42]:

$$[n^{\rm eq}(T)]^{-1} \sim \chi^{\rm eq}(T) = A\exp(-\kappa T), \qquad (2.57)$$

where A and κ are constants. The phenomenological parameter κ represents the linear term in the expansion of the temperature dependence of the exponent in Eq. 2.51 about temperature T_0 [38]. Assuming the anisotropy is dominated by the surface term, the parameters κ and A can be written in term of the film thickness d as:

$$\begin{aligned}\kappa = -\frac{\pi}{\Omega d}\frac{\partial E_w(T)}{\partial T}|_{T=T_0} &= -\left[\sqrt{\frac{4\pi^2\Gamma}{\Omega^2 K_s(T_0)}}\frac{\partial K_s(T)}{\partial T}|_{T=T_0}\right] d^{-3/2} \\ &= \alpha d^{-3/2} \end{aligned} \tag{2.58}$$

$$\begin{aligned} A &= \sqrt{\frac{4\pi^2 e^2\Gamma}{K_s d}}\left[\exp\left(\frac{4\pi\sqrt{\Gamma K_s(T_0)}}{\Omega} d^{-3/2}\right)\right]\exp(\kappa T_0) \\ &= \beta(d)\exp(\kappa T_0). \end{aligned} \tag{2.59}$$

2.9 Relaxation Processes in Ultrathin Films with Perpendicular Anisotropy

2.9.1 Domain Density Equilibration Process

In the above discussion, the stripe domain density is assumed to change instantaneously with temperature. In fact, the change in domain density with temperature involves the growth and/or shrinkage of domains. The domain growth and/or shrinkage is itself an activated process with activation energy E_n. This causes the stripe domain density $n(T)$ to deviate from its equilibrium value as the temperature changes. Hence, the response of the magnetic domain state to the applied magnetic field is, rather, described by the effective magnetic susceptibility $\chi^{\text{eff}}(T) \sim [n(T)]^{-1}$. The deviation of the stripe domain density from its equilibrium value depends on the time scale of the measurement itself, and it is the rate of change of temperature (R) that sets this time scale.

To construct a phenomenological description of the relaxation approximation of the domain density $n(T)$, we note that the domain growth and/or shrinkage does not proceed continuously but rather takes place in many discontinuous "Barkhausen" steps (ξ) since the domain wall has to overcome a local energy barrier. This is the same barrier involved in the domain wall motion in response to the applied magnetic field with energy barrier of E_a. Thus, we assume the activation energy E_n is the same as the activation energy E_a. In this case, the mean velocity v of the viscous wall motion between local barriers expresses as

$$v = \frac{\xi}{\tau_a(T)} = \frac{\xi}{\tau_{0a}} \mathrm{e}^{-E_a/kT}, \tag{2.60}$$

where $\tau_a(T)$ is the time constant for the activated domain wall motion between local barriers (see Eq. 2.52). When cooling from high temperature where $n = n^{\mathrm{eq}}$, domains shrink but probably do not disappear completely, leaving nucleation sites for domains to grow upon heating again. Assuming the average distance between nucleation sites is η, we define the average time for a full domain growth/shrinkage by τ_n. Using the relationship (2.60), it is expressed as

$$\tau_n = \frac{\eta}{v} = (\frac{\eta}{\xi}\tau_{0a})\mathrm{e}^{E_n/kT} := \tau_{0n}\mathrm{e}^{E_n/kT}. \tag{2.61}$$

Now, lets denote $N^{\mathrm{eq}}(T)$ and $N(T)$ as the number of domains in the equilibrium and non-equilibrium states respectively at a given constant temperature T, and $\Lambda(T) = N(T) - N^{\mathrm{eq}}(T)$. On average, the rate of change in Λ is governed by the time constant τ_n and thus can be described within the standard relaxation model as:

$$\frac{d\Lambda(T)}{dt} = \frac{-1}{\tau_n(T)}\Lambda(T). \tag{2.62}$$

Considering now the effective domain density[2] $n(T)(= N(T)/L_x)$, the relaxation approximation of Eq. 2.62 can be rewritten as

$$\frac{\partial n(T,t)}{\partial t} = -\frac{1}{\tau_n(T)}\left(n(T,t) - n^{\mathrm{eq}}(T)\right), \tag{2.63}$$

For a constant rate (R) of change in temperature, Eq. 2.63 becomes:

$$\frac{\partial n(T)}{\partial T} = -\frac{1}{R\tau_n(T)}\left(n(T) - n^{\mathrm{eq}}(T)\right). \tag{2.64}$$

---

[2] see its definition in sec.2.7

After rearranging the terms, the above equation can be rewritten as

$$\frac{\partial n(T)}{\partial T} + p(T)n(T) = p(T)n^{\mathrm{eq}}(T), \tag{2.65}$$

where $p(T) = (R\tau_n(T))^{-1}$. The solution is

$$n(T) = e^{-f(T)} \int_{T_i}^{T} e^{f(T')} p(T') n^{\mathrm{eq}}(T') dT' + Ce^{-f(T)}, \tag{2.66}$$

where $f(T) = \int_{T_i}^{T} p(T')dT'$ and T_i is the initial temperature. The constant C is determined by the initial condition. When cooling starts at room temperature or above ($T_i = T_0$) the domain density is assumed to have the equilibrium value $n^{\mathrm{eq}}(T_0)$, and thus $C = n^{\mathrm{eq}}(T_0)$. Therefore, the domain density while cooling at constant rate, $R_{cooling}$ is

$$n_{cooling}(T) = e^{-f(T)} \int_{T_0}^{T} e^{f(T')} p(T') n^{\mathrm{eq}}(T') dT' + n^{\mathrm{eq}}(T_0)e^{-f(T)}. \tag{2.67}$$

When heating at constant rate $R_{heating}$ starting at a minimum temperature $T_i = T_{min}$, the initial value of the domain density is then equal to $n_{cooling}(T_{min})$. Hence the domain density while heating is calculated according to :

$$n_{heating}(T) = e^{-f(T)} \int_{T_{min}}^{T} e^{f(T')} p(T') n^{\mathrm{eq}}(T') dT' + n_{cooling}(T_{min})e^{-f(T)}. \tag{2.68}$$

Figure 2.9(a) shows the effective susceptibility curves that were generated[3] using Eq. 2.68 for different heating rates. The initial state at low temperature was reached while cooling at the rate of -0.1 K/s (green line) according to Eq. 2.67. From this figure, it is clear that while cooling, the domain density can not change quickly enough to maintain its equilibrium, and reaches a certain temperature (*saturation*) below which the domain density is dynamically frozen. In this state, the film has more domains than in the equilibrium state. Upon heating from a minimum temperature, the domain density relaxes toward equilibrium through the annihilation of excesses

---

[3] The calculations are made using MathCad 12

domains until a certain temperature (T_e) is reached, and then the change in domain density proceeds through the domain formation. At $T = T_e$ the average domain density is equal to its equilibrium value, that is $n(T_e) = n^{\mathrm{eq}}(T_e)$. T_e is determined by the heating rate R. Accordingly, the magnetic susceptibility of Eq. 2.54 is given by:

$$\chi(T) = \frac{1 - i\omega\tau_a(T)}{1 + \omega^2\tau_a^2(T)}\chi^{\mathrm{eff}}(T), \tag{2.69}$$

A curve generated using this model is plotted in Fig. 2.9(b) for heating rates of 0.3 K/s, 0.5 K/s and 0.7 K/s along with the magnetic susceptibility of Eq. 2.54 (when $\tau_n = 0$).

In equation 2.61, we defined τ_{0n} in term of τ_{0a} as ($\tau_{0n} = \alpha\tau_{0a}$), where $\alpha = \eta/\xi$. The calculated susceptibility peak temperature (T_p) and peak height depend on the relative value α. An illustrative graph of this dependence is presented in Fig. 2.10. In Fig. 2.11 the peak temperature and peak height are plotted as a function of $\log_{10}(\alpha)$ for different constant heating rates R. The susceptibility peak temperature changes linearly with the heating rate (R) with a slope $B(= \Delta T_p/\Delta R)$ that depends on the value of α, that is $B = B(\alpha)$. Figure 2.12 shows the calculated value of B as a function of $\log_{10}(\alpha)$. The calculated value of the relative change in peak height with R is also plotted in Fig. 2.12 as a function of $\log_{10}(\alpha)$.

When α is relatively small, $\alpha < 10^{3.3}$, the differences in the effective susceptibility, due to equilibration process, are most apparent at very low temperature and are hidden by the dynamical factor. In this case the model predicts a very small change in the peak temperature with R ($B \approx 0$). A very small change in the peak heights is also predicted for all heating rates in the range studied here (region ① in Fig. 2.11, and Fig.2.12). An example of this behavior is shown in Fig. 2.10(a). In region ② where $10^{3.3} < \alpha < 10^{4.4}$ as in Fig. 2.10(b), the peak shifts to lower temperature with increasing heating rate ($B < 0$). This is accompanied with a change in the peak height with R. The relative change in the peak height increases monotonically

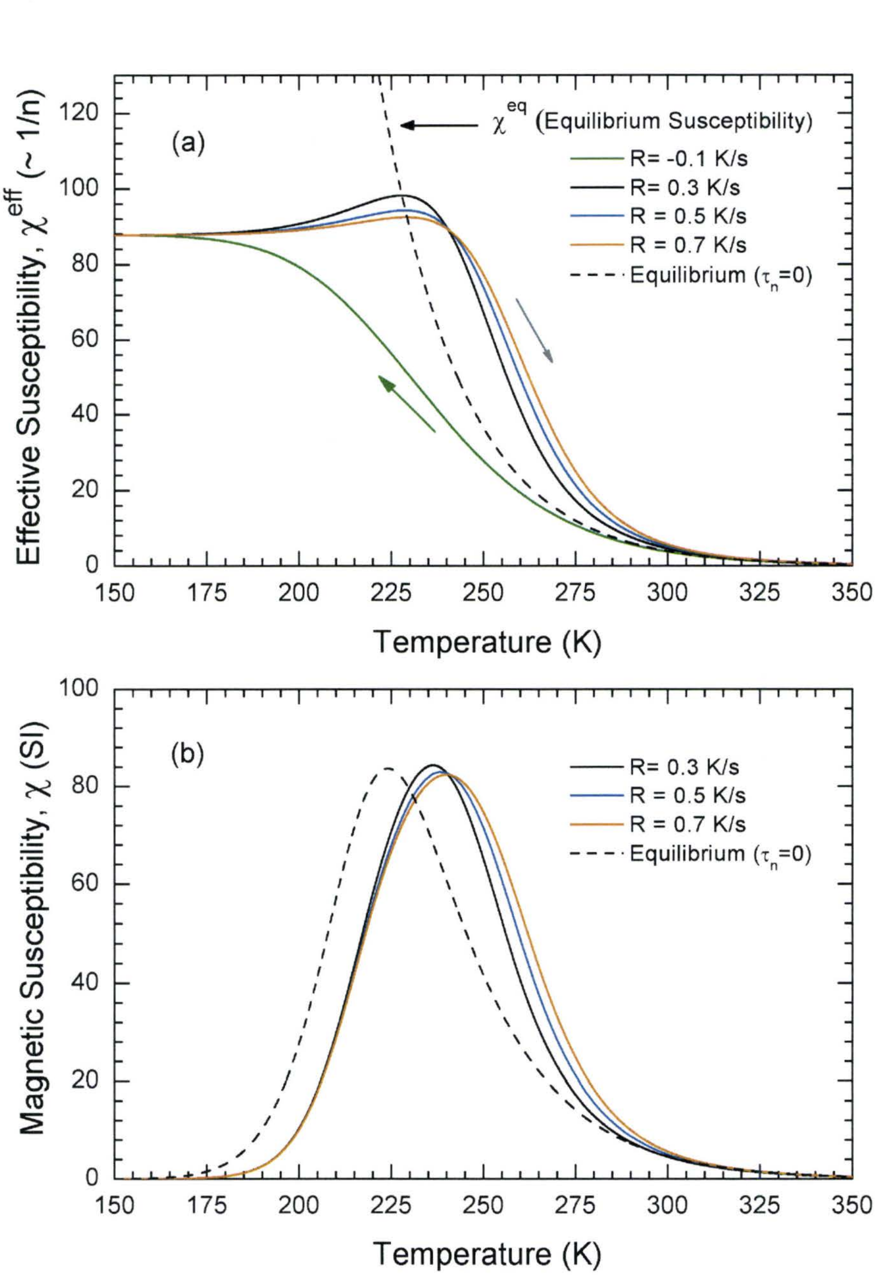

Figure 2.9: (a) *Model calculation of the effective susceptibility while heating at different constant rates. The green line represents the effective susceptibility while cooling at R = -0.1 K/s, and the dashed line represent the equilibrium susceptibility generated using Eq. 2.51 with* $A = e^{14.77}(SI)$ *and* $\kappa = 0.0446(K^{-1})$. *The nucleation time* τ_n *that has been used in this calculation is set using* $E_n = 2725(K)$ *and* $\tau_{0n} = 9 \times 10^{-4}(sec)$. (b) *Calculation of the magnetic susceptibility of Eq. 2.69 using* χ^{eff} *from part (a) and the activation energy* $E_a = 2725(K)$, $\tau_{0a} = 2.57 \times 10^{-9}(sec.)$, *and* $\omega = 2\pi \times 210(Hz)$.

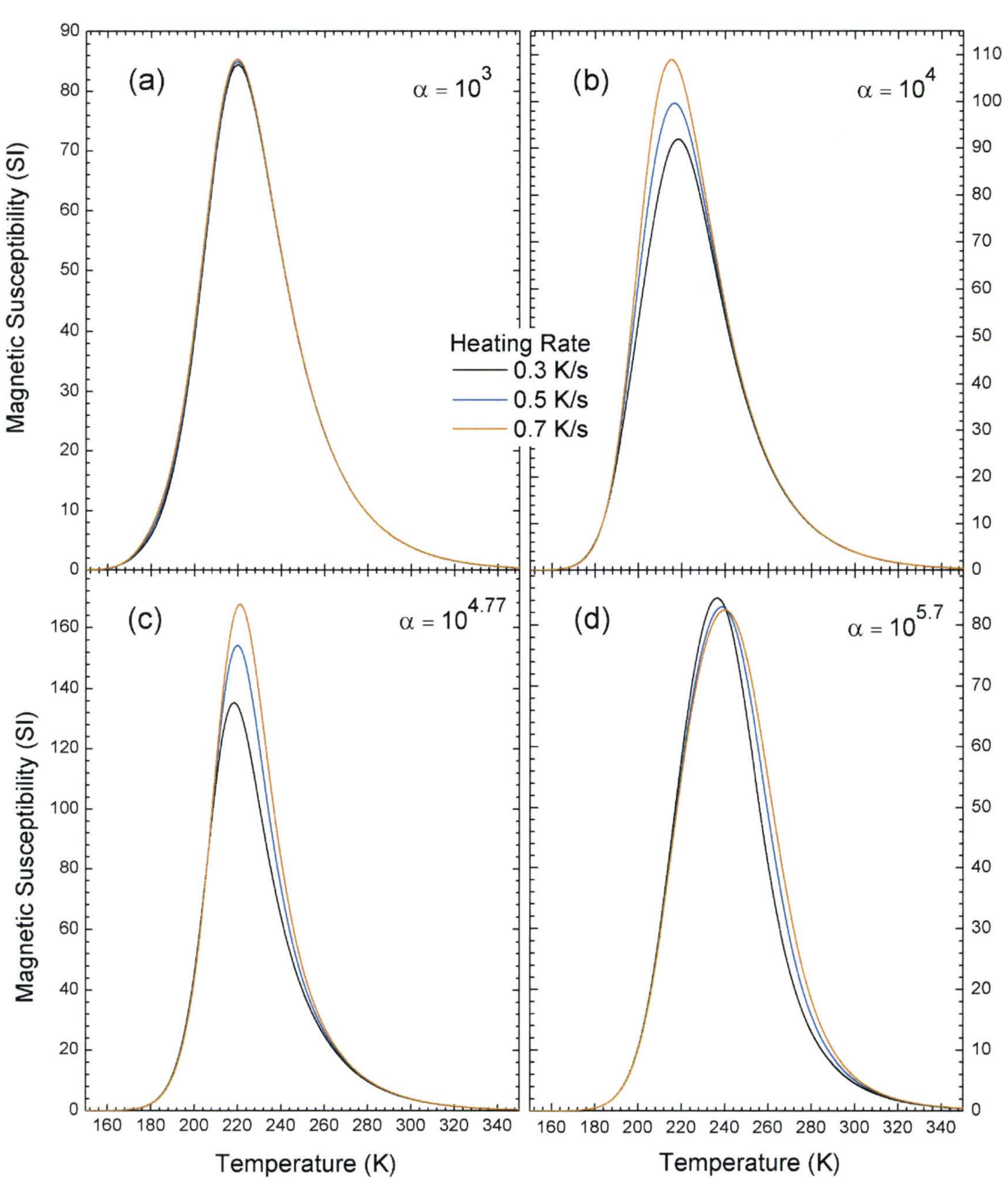

Figure 2.10: M*odel calculation of the magnetic susceptibility while heating at* $R = 0.3$ *K/s, 0.5 K/s, and 0.7 K/s for different value of* α ($\alpha = \tau_{0n}/\tau_{0a}$). *All other parameters are set to the same values that are used in the calculation presented in Fig. 2.9.*

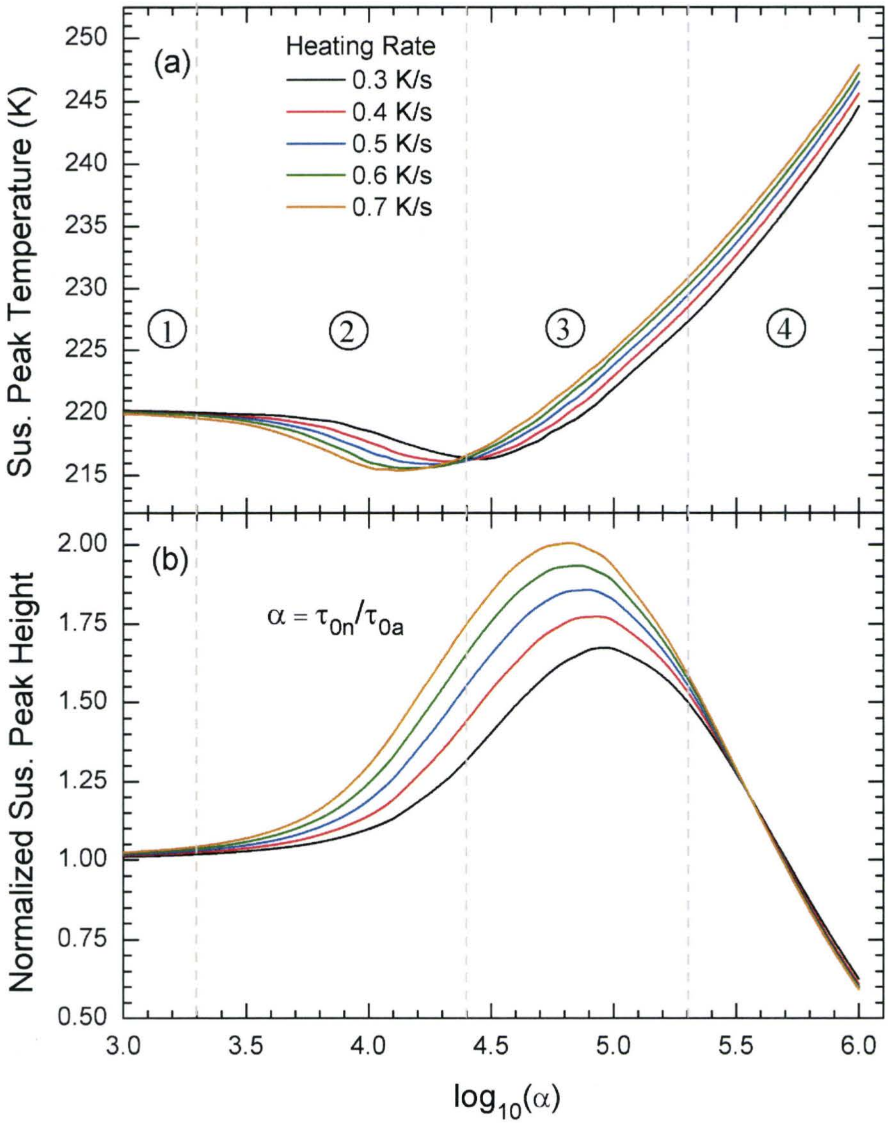

Figure 2.11: (a) *Calculated susceptibility peak temperature and* (b) *normalized susceptibility peak height as a function of* $\log_{10}(\alpha)$ ($\alpha = \tau_{0n}/\tau_{0a}$). *All other parameters that are used for this calculation are the same used in the calculation presented in Fig. 2.9.*

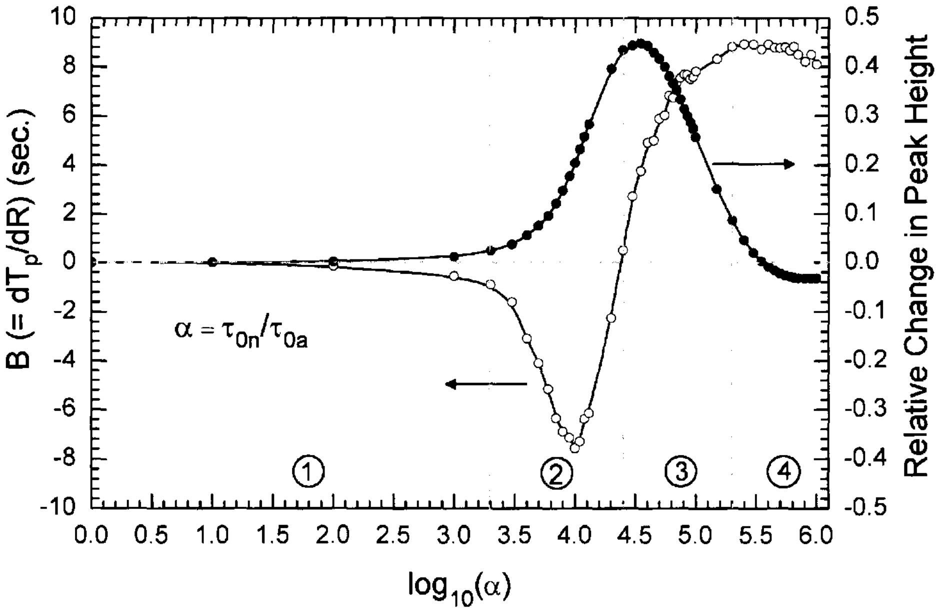

Figure 2.12: (a) *The rate of change in the susceptibility peak temperature with heating rate* R *(*$B = dT_p/dR$*), and the relative change in the susceptibility peak height with* R *as a function of* $\log_{10}(\alpha)$.

with α to reach a maximum value of 45% when $\alpha \approx 10^{4.4}$. In region ③ where $10^{4.4} < \alpha < 10^{5.3}$, as in Fig. 2.10(c), the peak shifts to higher temperature as R increases ($B > 0$). In this range, B increases with α up to a maximum value $B_{\max}$. The relative change in the peak heights decreases monotonically with α down to 10% when $\alpha \approx 10^{5.3}$. In the range where $10^{5.3} < \alpha \leq 10^6$, a negligible decrease in B with α is predicted, and the relative change in the peak height is within less than 10%. This is shown in region ④.

2.9.2 Domain Phase Transformation

As has been discussed in section 2.7, a series of domain phases are expected in perpendicularly magnetized ultrathin films as a result of the competition between the (ferromagnetic) exchange interaction and the (antiferromagnetic) dipolar interaction.

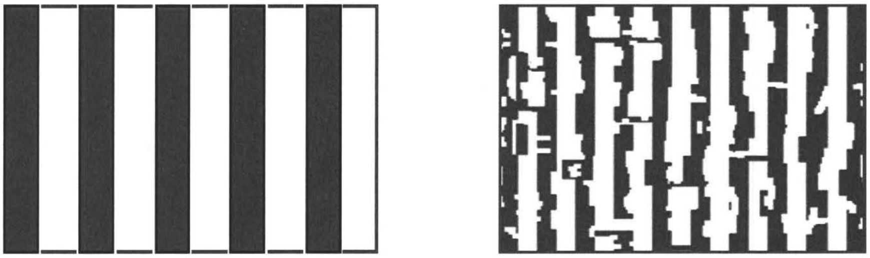

Order Stripe Phase *Delocalized Phase*

Figure 2.13: *A schematic graph shows the qualitative differences between the ordered strip phase (left) and the delocalized phase (right).*

In this study, domain phases are categorized into two types. Below a characteristic temperature T_O, an *ordered stripe* phase is the ground state in which domains are orientationally and positionally ordered (Fig. 2.13(left)). At a temperature above T_O one of the *delocalized* phases (Ising nematic, tetragonal phase) is expected to be the ground state (Fig. 2.13(right)). In this phase the orientational and/or positional order of the domains is lost due to domain wall segmentation that results from the fluctuation of the domain walls. The domain segments are free to align along a number of crystallographically defined axes, rather than a single axis as in the ordered stripe phase.

Numerical simulation show that the relaxation dynamics of the order stripe phase differs from that of the delocalized phases. A Monte Carlo study by Bromley *et al.* [24] has revealed that at $T > T_O$, the relaxation from magnetically saturated state to a tetragonal state occurs over a single short time scale by rapid decay of the magnetization to zero. However, at $T < T_O$ the relaxation toward the equilibrium "ordered stripe" state is found to occur over three time scales. At the very early stage, the relaxation proceeds over a short time scale by nucleation and growth of domains of spins with opposite orientation to the initial magnetization. At a later stage, the number of domains with opposite directions equilibrate over an intermediate time scale. Finally, the relaxation proceeds over a long time scale by the rearrangement of stripe domains in different regions of the sample, to align along a single axis. These regions with local orientations represent topological defects that are extremely slow to annihilate. In the previous section, we have discussed the first two processes and have modeled their influence on the behavior of the ac magnetic susceptibility that is recorded as a function of temperature.

The presence of the topological defects in the domain structure of the delocalized phase has an influence on the phase transition between the ordered stripe and delocalized phases. Indeed, numerical simulation studies by Cannas and co-workers [26, 27] have shown that upon rapid cooling from a temperature above the transition temperature T_O to a temperature below T_O, the system is quenched in a metastable delocalized Ising nematic state. They attributed this observation to the existence of large energetic barriers to the recombination of the high density of unbounded dislocations in the domain structure of the delocalized phase. Then they monitored t he relaxation of the quenched metastable state to the true equilibrium ordered stripe state. Their finding was that the system relaxes in two ways depending on the final temperature T' reached upon cooling. If T' is not too far below the ordered stripe to delocalized phase transition temperature T_O, the quenched state relaxes to the metastable nematic phase through a coarsening process, where domains of horizontal and vertical stripe orientation compete, and then by nucleation of the stable ordered stripe phase through desegmentation process. However, if T' is far below T_O the system relaxes through rearrangement of stripe domains along a single axis.

Because the magnetic system under the current investigation is a real magnetic system, consisting of Fe layers deposited on a 2 ML Ni/W(110) substrate, it does not correspond precisely to the numerically simulated system. As has been shown in previous studies [5, 35], this magnetic system has a twofold symmetry, which means that in equilibrium the domains will align along one direction, namely W[001] or, equivalently, the $[01\bar{1}]$ direction of the fcc Fe. The existence of the twofold symmetry in our sample makes it unlikely for the tetragonal phase to appear as one of the high temperature delocalized phases. Also, in an actual ultrathin film system, such as our sample, the competition between the short range exchange interaction and the long range dipole interaction ensures that the domain walls will not grow beyond a maximum width even when the effective perpendicular anisotropy approaches zero. In contrast, the magnetic system in the simulation studies mentioned above differs from our sample in many aspects. It is an Ising system on a square lattice with fourfold symmetry, which means the magnetic domains have two equivalent directions to align along. The existence of the fourfold symmetry permits the formation of mutually perpendicular stripe domains in the high temperature tetragonal phase. In Ising system, the domain wall width is temperature independent with an effective zero width. Another important difference is that the system studied by the simulations does not have structural defects which are the source for the domain wall pinning mechanism in our sample, and add to the internal energy of the system. Nonetheless, some important findings from these simulations along with the other theoretical studies [3, 13–16, 18–29] that are reviewed in Chapter 1 are expected to apply to the experimental study. For example, the dependence of the domain density on temperature, $n(T)$, and the evolution of domain phases in a real magnetic system should be, at least qualitatively, follow the prediction made from these theoretical studies. This is especially true at high temperature where $\omega\tau_a(T) \ll 1$, as the pinning of domain walls become ineffective. Also, in the temperature range where $\omega\tau_a(T) \ll 1$, the relaxation process involving domain segments reorientation along a single axis and/or annihilation of topological defects should be on the same time scale in both systems. However, in the low temperature range where $\omega\tau_a(T) > 1$, the domain wall pining by structural defects could increase the energy barrier that is required to overcome in the process of relaxation toward the equilibrium. This in turn would make the relaxation process of domain phase transformation proceeds more slowly than that of the simulated system.

In this work, we study the relaxation processes in an ultrathin Fe film magnetized perpendicular to its plane, by means of the magnetic ac susceptibility. The susceptibility is measured while heating the system from an initial temperature T_i. The initial state at low temperature, T_i ($< T_O$), is prepared by cooling the system from high temperature, T_d ($> T_O$) where the system is expected to be in the delocalized phase. If the system, upon cooling, is quenched in a metastable delocalized phase at $T = T_i$, then it may be possible to monitor the relaxation of this state to the stable ordered stripe state by means of ac the susceptibility. The time scale of the susceptibility measurement is set by the rate of change in temperature variation R, and thus the total time given to the system to relax to its equilibrium state is controlled by altering R. The presence of the topological defects in the domain structures in the delocalized phases, will affect the response of the domain walls to the applied magnetic field. The density of these defects depend on the total time given for the system to relax while heating. Therefore, the relaxation of the quenched delocalized state to the equilibrium state will manifest itself quantitatively in the susceptibility trace.

Chapter 3

Experimental Techniques

When studying the properties of ultrathin films with thickness of 10 atomic layers or less, the film must be kept free of contaminants during all stages of the experiment. Therefore, surface science experiments are normally carried out under ultrahigh-vacuum (UHV) conditions. In this study, ultrathin magnetic Fe films are prepared and characterized in an UHV system. The UHV system consists of a conventional UHV chamber equipped with an Auger electron spectroscopy (AES), and a low energy electron diffraction (LEED) apparatus for film structural characterization, and with electron beam heated evaporation sources for film deposition. The investigation of magnetic domain dynamics in perpendicularly magnetized ultrathin Fe film on top of a 2 ML Ni(111)/W(110) substrate presented in chapter 4 is made by the use the magnetic ac-susceptibility χ that is measured *in situ* by means of the surface magneto-optic Kerr effect (SMOKE). In this chapter, we review in some detail the basic physics behind these techniques and their experimental set-up. This study benefits from earlier growth and structure characterization studies [5, 40, 41]. Experimental procedures adopted from these studies will be reviewed in chapter 4. Expected contributions to the measured susceptibility are discussed in chapter 4 in terms of relevant experiments for their quantification.

3.1 UHV System

3.1.1 UHV Chamber Preparation

The experiments are carried out in an UHV chamber of Fig. 3.1 with a base pressure of 2 x 10^{-10} torr. The chamber is equipped with a mechanical rotary pump, a titanium sublimation pump (TSP) and ion pump. When pumping the chamber down from atmospheric pressure, the mechanical pump, with the use of a liquid nitrogen cold trap, is used for almost an hour to reduce the chamber pressure down to the range of 10^{-6} torr. At this stage, the ion pump is engaged after the fore-line to the mechanical pump is valved off . The ion pump traps the gas inside the system by ionizing the gas molecules. These ionized molecules are then accelerated by strong electric field to a thick titanium plate inside the pump and trapped. The ion pump is kept operating as the primary pump during and after a modest bake-out of the chamber. The chamber is baked out at around 150 °C for 12 - 24 h, so that the water vapor and the adsorbed gases on the surfaces inside the chamber desorb as much as possible, and then pumped away by the ion pump. After this step, and once the chamber has cooled down to a room temperature, the pressure inside the chamber will be in the range of 10^{-9} torr. At this stage, the titanium sublimation pump (TSP) is engaged to reduce the pressure even further to the range of 10^{-10} torr. The TSP consists of 3 filaments that made from an alloy of Titanium (Ti) and Molybdenum (Mo). When heating the filament to a high temperature, by the application of a high current, the Titanium is sublimated directly from the filament to the nearby walls of the chamber (at the very bottom of the chamber). The Titanium layer on the chamber walls combine with the active gases as the gas molecules strike the walls and stick to the side of the chamber. The TSP is used daily, at least once, to maintain a good UHV pressure.

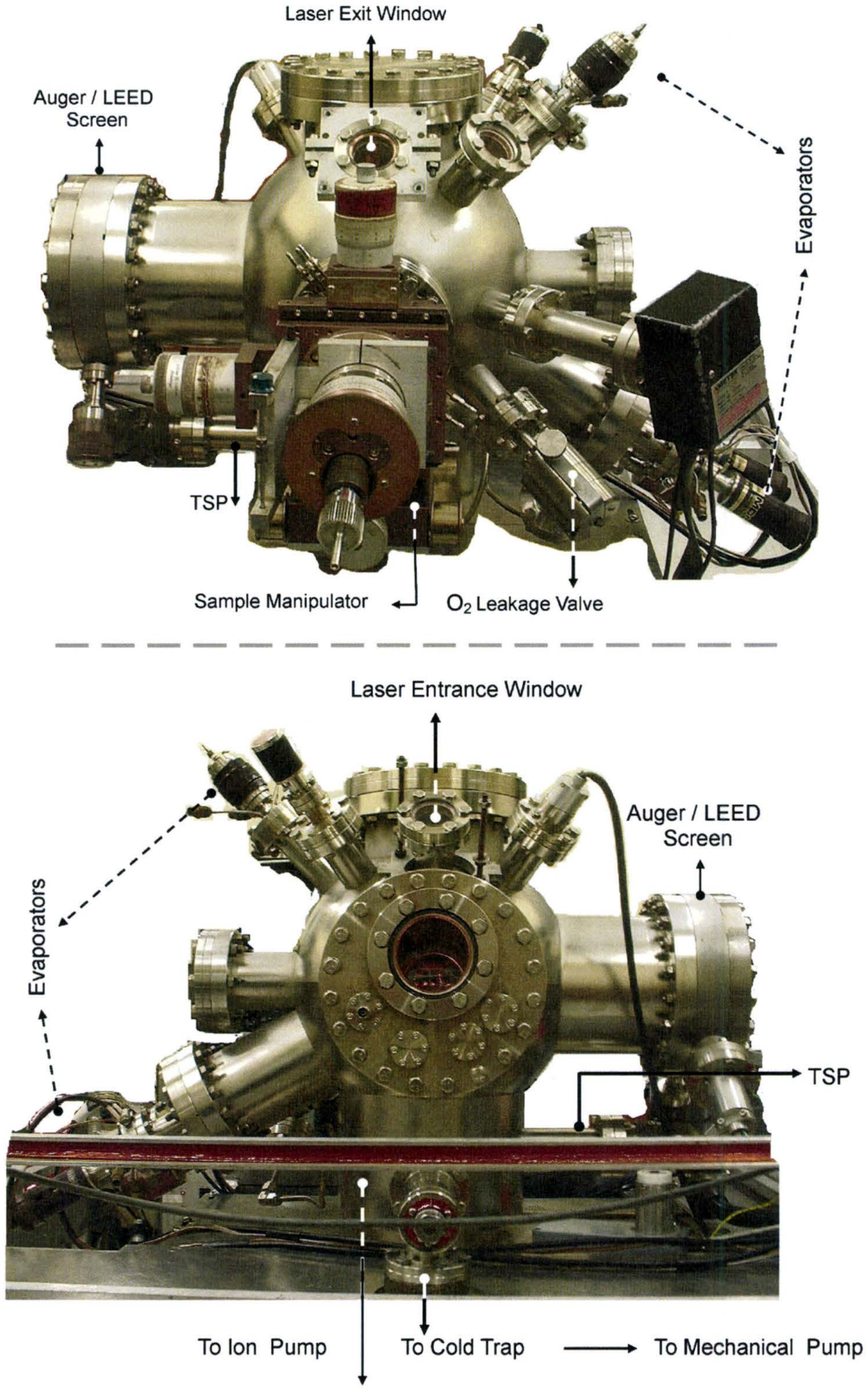

Figure 3.1: *Side-viewes of the UHV Chamber highlight the major components.*

Various instruments inside the chamber are operated at temperature higher than the bake-out temperature. Such instruments include the Auger/LEED electron gun, ion gauge filament, and the evaporators used for film deposition. These instruments have to undergo an extensive degas process so as to remove any remnant surface contamination that is left after the bake-out. This is simply done by heating the filaments of each instrument to high temperature, by the application of high current, for almost an hour.

3.1.2 Substrate Preparation

The bcc closed-packed W(110) substrate is chosen in this study to serve as the non-magnetic substrate. It was cut from a W single crystal to dimensions 1.1 x 0.8 x 0.2 cm^3, with a miscut less than 0.4° in the crystallographic [110] direction. Tungsten is chosen as a crystal substrate for few reasons. It has a very high surface free energy, making it likely that deposited material will wet it well for at least the first monolayer of the deposited material (this will be discussed in more detail in the next section). Secondly, it has very high melting point ($\sim$ 3700 K), which allows one to clean the surface by flashing (heating to high temperature, about 2600 K). Finally, a Ni buffer with the thicknesses of two or three monolayers is known to grow in a highly ordered (111) fcc structure on W(110) [74]. In this study, a 2 ML Ni buffer is used as a template for the subsequent growth of slightly strained fcc Fe.

The W(110) substrate is mounted on the sample holder that is connected to the manipulator (see Ref.[75] for a detailed design). The manipulator is capable of XYZ motions and 360^o rotation about the manipulator axis (Z-axis) and about the substrate surface normal. The sample can be moved and rotated at any position for various parts of the experiment: film deposition, Auger/LEED spectroscopy, and magnetic characterization. The sample temperature is measured using a W5%Re-W20%Re thermocouple embedded in the W(110) crystal. Temperature control is provided by cooling the sample holder with a copper braid extending to a liquid nitrogen reservoir and heating by radiation from a filament behind the substrate.

Prior to the film deposition, the W(110) substrate is cleaned and checked for any evidence of surface contaminants. Heating the substrate to high temperature ($\sim$2600 K) is sufficient to remove most of the contaminants from the surface of the W substrate. However, carbon contaminants bond very strongly to W, and are not removed by flashing. The presence of any carbon contaminants can be checked by Auger electron spectroscopy (AES) as will be discussed in section.3.3.

To clean the carbon from the W surface, the crystal is exposed to a partial pressure of 10^{-7} torr oxygen that reacts with surface carbon, forming carbon monoxide CO. The carbon monoxide is easily desorbed from the surface with flashing. The cleaning procedure is therefore a series of oxygen exposures followed by flashing to $\sim$2600 K. The carbon contamination is measured after each cycle by AES. The process is repeated until no evidence of carbon is detectable.

3.2 Film Preparation and Film Growth Modes

3.2.1 Film Growth Modes

Molecular beam epitaxy (MBE) technique is adopted for the preparation of the ultra-thin films for this study. The term epitaxy describes the orientation of the deposited crystal (Film) on another crystal (Substrate). Experimental observations have revealed three epitaxial growth modes as shown in Fig. 3.2. The layer-by-layer, or Frank-van der Merwe (FM), growth mode arises because the atoms of the deposited material are more strongly attracted to the substrate than they are to themselves. In this form of growth, the $(n+1)$th layer starts only after the nth layer has been completed. In case the deposited atoms are more strongly bound to each other than

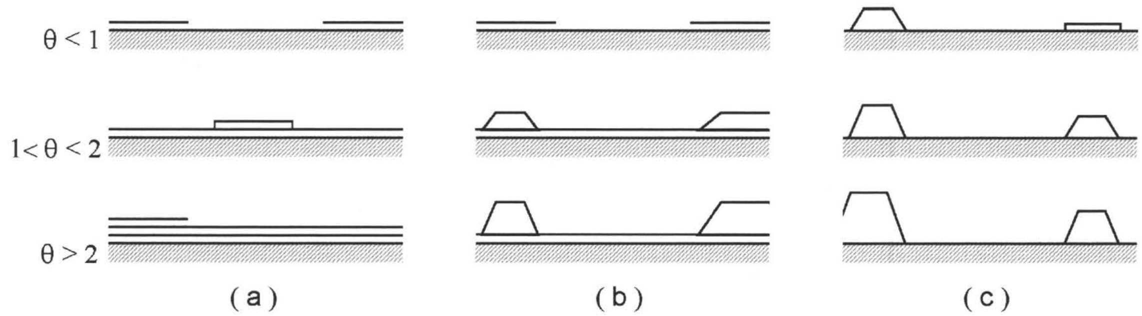

Figure 3.2: *Schematic representation of the three growth modes, as a function of the coverage* θ *in monolayer* (ML)*. (a) layer-by-layer, or Frank-van der Merwe growth, (b) layer-by-layer plus island, or Stranski-Krastanov* (SK) *growth and (c) island, or Volmer-weber* (VW) *growth. After [77].*

they are to the substrate, the island, or Volmer-Weber (VW) growth mode is observed. In this mode, the film grows as three-dimensional islands on the substrate. An intermediate case is the layer-by-layer plus island, or Stranski-Krastanov (SK), growth mode in which the film initially grows in a layer-by-layer fashion but then develops three-dimensional islands above a certain thickness.

Bauer [76] was the first to develop a thermodynamic criterion (Fig. 3.3) for the epitaxial growth mode. He found that the growth modes of thin films can be considered as a wetting problem, which is determined by the following energy difference

$$\triangle\sigma = \sigma_f + \sigma_i - \sigma_s, \tag{3.1}$$

where σ_s is the surface energy of the substrate, σ_i is the free energy of the substrate/film interface, and σ_f is the surface energy of the film. If $\triangle\sigma \leq 0$, the deposited atoms are more strongly bound to the substrate than to each other and the film tends to wet the substrate to minimize the total energy of the film/substrate system and layer-by-layer, or (FM) growth mode should be observed. If $\triangle\sigma > 0$, the island, or (VW) growth mode is favorable. The layer-by-layer plus island, or (SK) growth mode arises because the film energy may have a contribution such as strain energy which increases as the film thickness increases. Thus it is possible that below

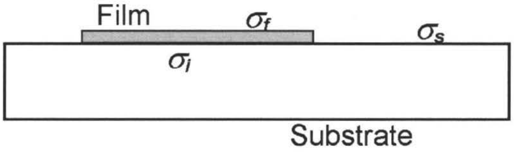

Figure 3.3: *Bauer's thermodynamic criterion for the growth mode.*

certain thickness the $\triangle\sigma$ is less than zero and then is larger than zero above this thickness.

In the above discussion, the film growth mode is determined assuming thermodynamic equilibrium. In fact, the film growth is a non-equilibrium kinetic process. The actual growth mode is influenced by the growth conditions, such as growth rate and substrate temperature, and the material parameters of the film/substrate system. Hence, by controlling these growth parameters, one can produce a layer-by-layer epitaxial film, even in non-wetting system.

3.2.2 Film Deposition

The ultrathin film is deposited using electron beam evaporation. A schematic of the evaporator used in this study is shown in Fig. 3.4. Evaporation of the source is achieved using electron beam heating. A ground-potential semi-circular tungsten filament is used to supply electrons. A high positive voltage is applied to a movable post holding the film material source rod, and accelerates the electrons to the rod where their energy is transfered to the source, melting and evaporating the tip.

The amount of the material being deposited is monitored by high-precision electrometer that is connected to the second aperture. The electrometer measures the current of ions hitting the second aperture, and this current is proportional to the flux of atoms leaving the evaporator. When depositing iron using a second aperture current of 1.5 nA, 1 monolayer is typically completed in 3-5 minutes depending on

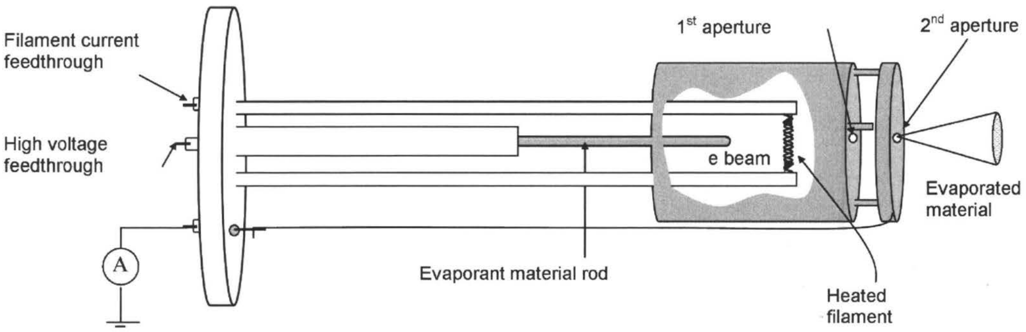

Figure 3.4: *A schematic diagram of electron beam evaporator.*

how well the source rod is centered behind the aperture. The calibration parameters, such as substrate position and deposition time for 1 monolayer are determined in advance in separate runs with use of Auger electron spectroscopy.

3.3 Auger Electron Spectroscopy

3.3.1 Auger Process

Auger electron spectroscopy (AES) is a powerful surface science technique that can be used for monitoring surface cleanless, growth modes, and thickness of ultrathin films. AES is based on a radiationless electron transition called the Auger effect [77]. In the Auger process, a core level of a surface atom is ionized by one electron from an impinging beam of high energy electrons (primary energy in the range of 2-5 keV). This is shown in Fig. 3.5(a) for the *KLL* Auger process. The ionized atom that remains after the removal of the core level electron is now in a highly excited state and relaxes to a lower energy state. The relaxation is achieved by filling the core hole with electron from outer level (L_1 level in the example of the Fig.3.5). The excess energy from the transition is either carried away by photon, or alternatively transfered to another outer level electron ($L_{2,3}$ level electron), with a characteristic

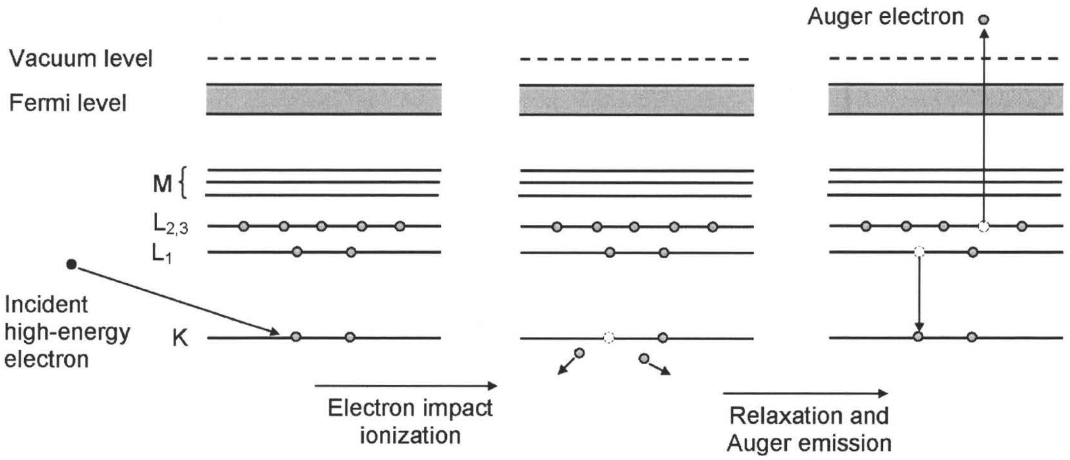

Figure 3.5: *Schematic representation of the KLL Auger process. (a) A high energy electron impacts an atom and (b) Ionizes the core K-level. (c) An outer L-level electron de-excites to K-level and the excess energy is carried out by another L-level electron: an Auger electron is emitted.*

kinetic energy, E_k $(= E_K - E_{L_1} - E_{L_{2,3}})$. The ejected electron is called an Auger electron. Clearly, the energy of the Auger electron depends only on the energy levels of the atom involved and not on the energy of the impinging electron creating the initial core hole, and thus the energy of the Auger electron is characteristic of the atom. Hence AES is element-specific technique.

Auger electrons generally have low energies in the range of (10-500 eV). The inelastic mean-free-path of such electrons is typically in the range of few atomic layers. Therefore, Auger electrons from atoms within only the first few layers will escape without significant loss of energy. This makes AES a surface-sensitive technique. It is used to check surface cleanless and to determine the chemical composition of deposited material.

Auger electrons are not the only electrons emitted from the sample surface when probed by a beam of primary electrons. Most of the the emitted electrons are inelastically scattered electrons from the primary beam. A plot of the number of electrons emitted from the sample surface with a given kinetic energy, $N(E)$, would display only a small peak at any particular Auger electron transition. In order to enhance the detection of the Auger electron peaks, the spectrum of $N(E)$ is differentiated by using a lock-in technique to produce $dN(E)/dE - E$ spectrum. In this way, most of the smooth background is removed leaving only features of Auger transitions.

In our AES apparatus, the secondary and the Auger electrons are collected by the hemispherical LEED/Auger screen (see Fig.3.8). A variable retarding potential-grid placed between the sample and the screen rejects any electrons with a kinetic energy below a selected energy. The retardation voltage on the grid is modulated by a small ac-voltage signal at a frequency ν of 4.7 kHz. The modulated AES signal is compared to the reference signal with of frequency ν, by lock-in detection. To record the $dN(E)/dE-E$ spectrum, only the signal at the second harmonic, 2ν is measured.

In a typical AES measurement, the retardation potential is varied over a narrow range of energy containing a spectral feature of the desired atomic species. For example, to check for carbon contamination on the tungsten substrate the AES ($dN/dE - E$) spectrum is measured in energy range of (170 -290 eV). This measured spectrum that is presented in Fig. 3.6 contains both the tungsten Auger peaks (170-220 eV) and the carbon Auger peak at 275 eV. By comparing the amplitude of the carbon peak (β) against the amplitude of the tungsten peaks (α), one can have an indication of the cleanliness level of the substrate. In this study, a ratio (β/α) of less than 10% indicates a clean substrate.

3.3.2 Characterization of Ultrathin Film Growth Modes and Thickness Calibration Using AES

The attenuation of Auger electrons can be employed to determine the mode of ultrathin film growth and calibrated film thickness. Many Auger electrons are lost

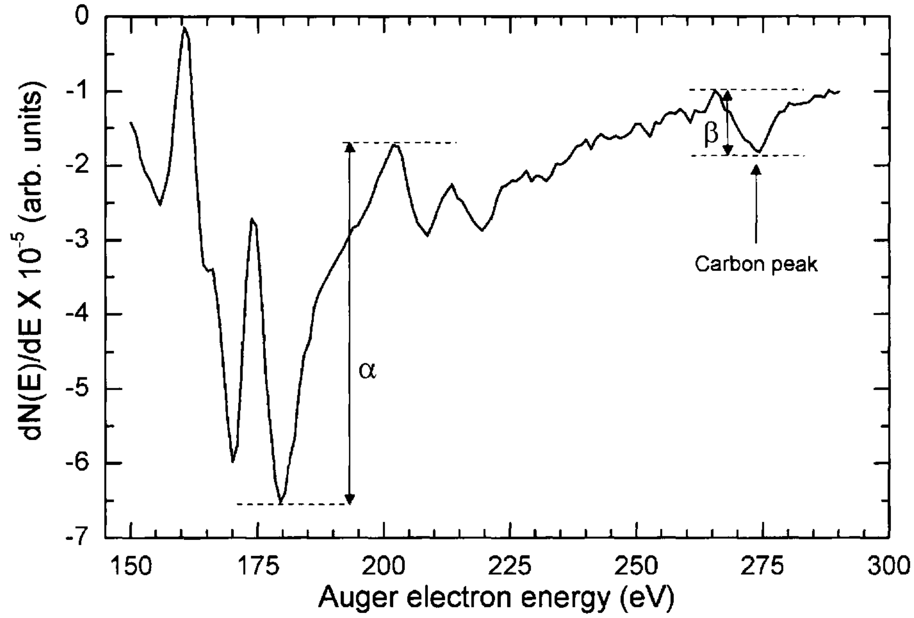

Figure 3.6: *Auger spectrum showing tungsten and carbon Auger features.*

due to inelastic scattering as the electrons escape into the vacuum. Let t_f represent the probability that an Auger electron emitted from a film atom will be transmitted through a layer of film atoms placed above it without an inelastic scattering event. For layer-by-layer, or FM growth, the Auger signal from n completed film-atom layers (I_f^n) is then given by [77]

$$I_f^n = I_f^1(1 + t_f + t_f^2 + \cdots + t_f^{n-1}) = \frac{I_f^1(1 - t_f^n)}{1 - t_f}, \tag{3.2}$$

where I_f^1 is the signal from the first monolayer without attenuation. For the substrate, the Auger signal is [77]

$$I_s^n = t_s^n I_s^0, \tag{3.3}$$

where I_s^0 is the signal from the clean substrate and t_s is the transmission coefficient for the elastic Auger electron from the substrate when it traverses a layer of film atoms. Now assuming n layers have been completed and a fraction θ of the surface

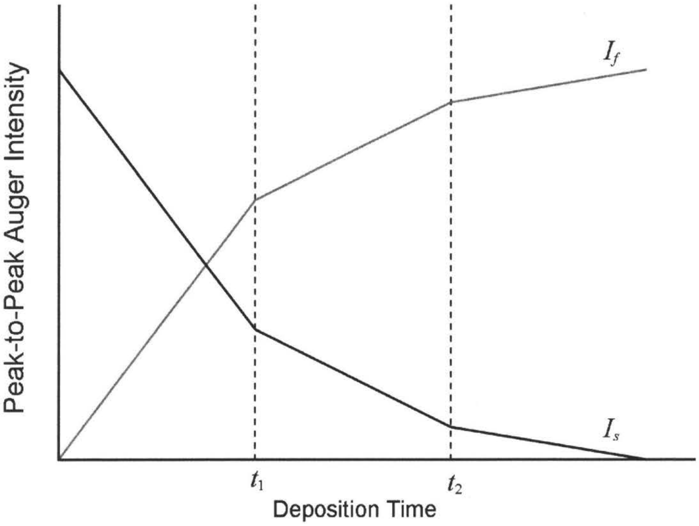

Figure 3.7: *Peak-to-peak Auger intensity of the film (I_f) and the substrate (I_s) as a function of deposition time. The breakpoints correspond to the completion of the first and the second monolayer for deposition time t_1 and t_2, respectively*

of the nth layer has been covered by the $(n+1)$th layer, the Auger signal for the film atoms, in this case, is [77]

$$I_f = I_f^n + I_f^1 t_f^n \theta, \tag{3.4}$$

and the Auger signal of the substrate atoms is then [77]

$$I_s = t_s^n I_s^0 + I_s^0 (t_s^{n+1} - t_s^n)\theta. \tag{3.5}$$

Eq. 3.4, and Eq. 3.5 show that the Auger signal for both the film atoms and the substrate atoms, respectively, changes linearly with coverage θ during the growth of a particular layer. Linear behavior will continue after the completion of this layer but at different slope. With increasing film thickness, the absolute difference in the slope between neighboring layers becomes smaller and smaller. Therefore, a plot of the peak-to-peak Auger intensity (I) of either the film or the substrate against the deposition time ($\sim$ coverage θ) should give linear segments separated by equally spaced breakpoints. These breakpoints appears upon completion of monolayers in layer-by-layer, or FM, growth (Fig. 3.7).

In case of island, or VW growth mode, the Auger signals vary slowly and continuously with the deposition time. In the case of layer-by-layer plus island, or SK growth mode, linear segments are observed until a certain thickness after which the Auger signal start varying continuously.

3.4 Low-Energy Electron Diffraction (LEED)

Low-energy electron diffraction (LEED) is another powerful technique for studying the structure of thin films and surfaces. As with all surface diffraction techniques, the analysis is based in terms of the reciprocal lattice.

In a typical LEED experiment (Fig. 3.8)(left), a monochromatic beam of electrons, at low energy (50-500 eV), is incident on a sample surface, usually normally. The electrons that are elastically scattered from the surface atoms are allowed to pass a retarding field analyzer (RFA) grids and hit a phosphor screen, where they produce bright spots whose intensity is proportional to the number of electrons in the corresponding beams. The diffraction pattern that is displayed on the screen can be observed through the Auger/LEED viewport window and can be recorded using a CCD camera. Two types of information can be obtained from LEED experiment. The LEED pattern can be quantitatively analyzed by recording the intensity (I) of an individual reciprocal lattice point as a function of the probe energy (E). The comparison of experimental $I(E)$ curve with the theoretical one, may provide accurate information on atomic positions on the surface [77]. Qualitative use of LEED is simply made by the analysis of the spot position to give information on the symmetry of the surface structure. As will be seen later, in the presence of a deposited film the qualitative analysis may reveal information about the size and rotational alignment of the film unit cell with respect to the substrate unit cell.

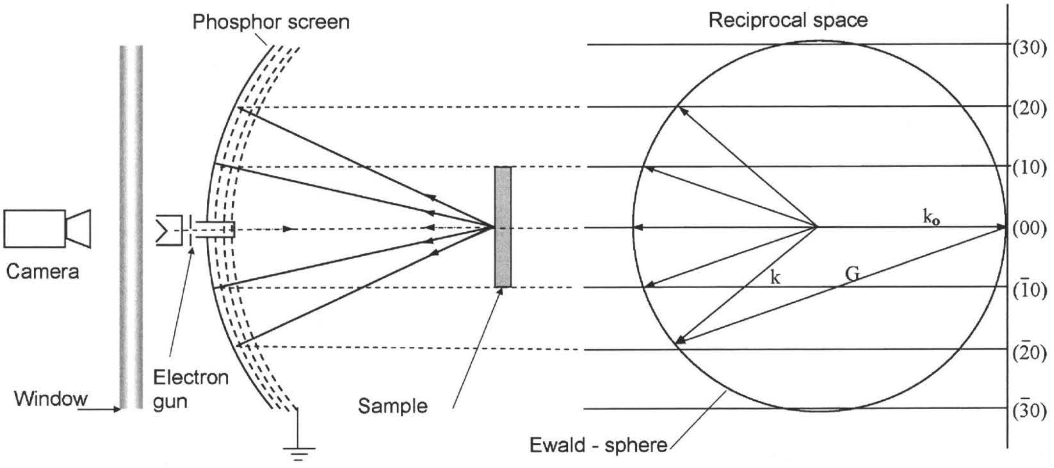

Figure 3.8: *A schematic representation of a typical experimental LEED setup (left) and the relationship between the LEED pattern displayed on the phosphor screen and reciprocal space (right).* $\boldsymbol{k}_0$ *and* $\boldsymbol{k}$ *are the incident and final wave vectors of the electrons and* $\boldsymbol{G}$ *is reciprocal lattice vector*

The diffraction pattern is directly connected to the reciprocal lattice by the diffraction condition [78–80]:

$$(\mathbf{k} - \mathbf{k}_0) = \mathbf{G}, \tag{3.6}$$

where $\mathbf{k}_0$ and $\mathbf{k}$ are the incident and final wave vectors of the electrons, and $\mathbf{G}$ is reciprocal lattice vector. This condition is graphically illustrated in Fig 3.8(right) using the Ewald sphere construction. The construction is made by placing a sphere of radius k_0 into the three-dimensional reciprocal lattice. The vector $\mathbf{k}_0$ begins at the center of the sphere and ends on a lattice point. The condition of Eq. 3.6 will be satisfied whenever another lattice point lies on the sphere, k. The vector $\mathbf{G}$ is a translation vector between those two reciprocal lattice points. If $\mathbf{a}_1^*$, $\mathbf{a}_2^*$, $\mathbf{a}_3^*$ are the primitive vectors of the reciprocal lattice, the vector $\mathbf{G}$ is written as

$$\mathbf{G} = \upsilon_1\mathbf{a}_1^* + \upsilon_2\mathbf{a}_2^* + \upsilon_3\mathbf{a}_3^*, \tag{3.7}$$

where $\upsilon_1, \upsilon_2, \upsilon_3$ are integers. The reciprocal lattice is related to the real space lattice via the relationship between the primitive vectors of both lattices as:

$$\mathbf{a}_1^* = 2\pi\frac{\mathbf{a}_2 \times \mathbf{a}_3}{\mathbf{a}_1 \cdot \mathbf{a}_2 \times \mathbf{a}_3} \qquad \mathbf{a}_2^* = 2\pi\frac{\mathbf{a}_3 \times \mathbf{a}_1}{\mathbf{a}_1 \cdot \mathbf{a}_2 \times \mathbf{a}_3} \qquad \mathbf{a}_3^* = 2\pi\frac{\mathbf{a}_1 \times \mathbf{a}_2}{\mathbf{a}_1 \cdot \mathbf{a}_2 \times \mathbf{a}_3}, \tag{3.8}$$

where $\mathbf{a}_1$, $\mathbf{a}_2$, $\mathbf{a}_3$ are the primitive vectors of the real space lattice. Thus from the diffraction pattern one may obtain direct informations about crystal structure in real space.

In LEED experiment, the impinging electron have low energies and thus the diffraction occurs in the range of a few atomic layers. Thus, the diffraction pattern mainly originates from two-dimensional periodicity of the surface. The periodicity in the direction normal to the surface is considered infinite ($\mathbf{a}_3 \to \infty$). The reciprocal lattice points along the surface normal are therefore infinitely dense ($\mathbf{a}_3^* \to 0$). This leads to reciprocal lattice rods instead of points. In this case, the two-dimensional diffraction condition is in the form [78–80]:

$$(\mathbf{k}^{\|} - \mathbf{k}_0^{\|}) = \mathbf{G}^{\|} = \upsilon_1\mathbf{a}_1^* + \upsilon_2\mathbf{a}_2^*, \tag{3.9}$$

where $\mathbf{k}^{\|}$ and $\mathbf{k}_0^{\|}$ being the projection of $\mathbf{k}$ and $\mathbf{k}_0$ on the surface, and $\mathbf{G}^{\|}$ is the surface reciprocal lattice vector.

As mentioned earlier, on qualitative level one can use the LEED pattern to determine the registration of film atoms with respect to the underlying substrate lattice. For example Fig. 3.9 shows a schematic representation demonstrating the relationship between image of the reciprocal lattice (LEED pattern) and real space surface for a commensurate superstructure. The grey spots in the LEED pattern are the reciprocal lattice points from substrate and the black spots are the extra spots associated with the deposited film atoms. Another example of LEED pattern image is shown in Fig. 3.10 for Ni/W(110) system. This system was utilized as a substrate in the magnetic studies of chapter 4. The Ni first monolayer on W(110) forms a highly strained 7x1 pattern [74, 81]. This means that along one direction of the film, the unit cell of the film is only commensurate with the substrate every seven unit cells of the substrate, but it is fully commensurate along the other direction.

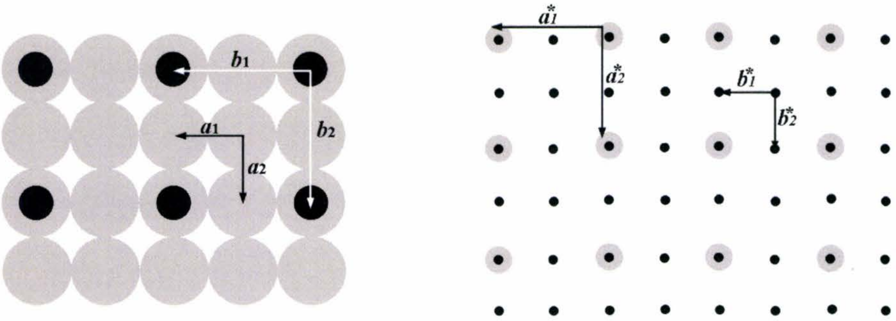

Real Space

Reciprocal Space
" Diffraction Pattern"

Figure 3.9: *A schematic representation illustrates the relationship between the real space lattice and the associate reciprocal lattice*

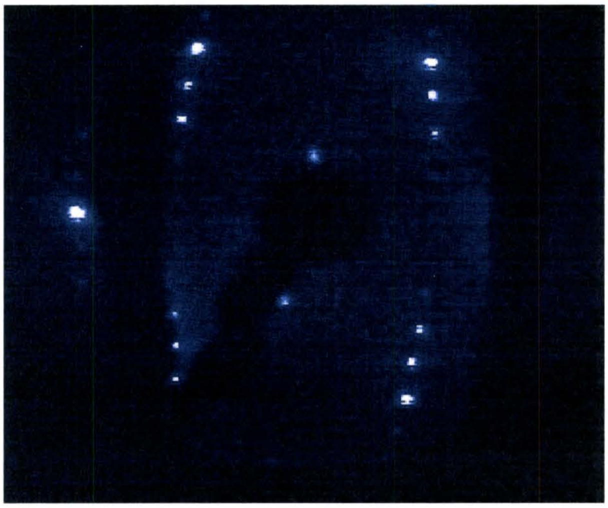

Figure 3.10: *7×1 LEED diffraction patterns of a 1 ML of Ni on W(110).*

3.5 Magnetic Measurements

To study the response to an applied magnetic field, the most common measurements that are made on magnetic materials are the magnetization hysteresis curve and the magnetic susceptibility. In the following, an introduction to these type of the magnetic measurement is given first. An explanation of the surface magneto-optic Kerr effect (SMOKE), the technique that has been used in this study for these measurements, then follows.

3.5.1 Background

Magnetization Hysteresis Curve

A magnetization hysteresis curve is produced by subjecting a magnetic sample to a changing, external magnetic field H and seeing how the magnetization of the sample M changes with the change of the magnetic field. Some materials are hard to magnetize. It takes a strong magnetic field to produce a given magnetization in such a material, and thus are called hard magnetic material. Other materials requires smaller field to produce the same magnetization in the sample and are called soft magnetic materials. A typical Magnetization hysteresis curve is shown in Fig. 3.11. As the external magnetic field is increased, the magnetization of the sample will increase until it reaches a saturation value M_s. If the magnetic field is subsequently decreased to zero there is a remnant magnetization M_r left in the sample, and then, if the field is reversed, the coercive field H_c is required to drive the remanent magnetization to zero. These features depend on a number of properties of the sample which determine the magnetic structure; among these are the strength of the exchange coupling between the magnetic atoms, and demagnetizing field which is related to the self energy and the magnetic anisotropy.

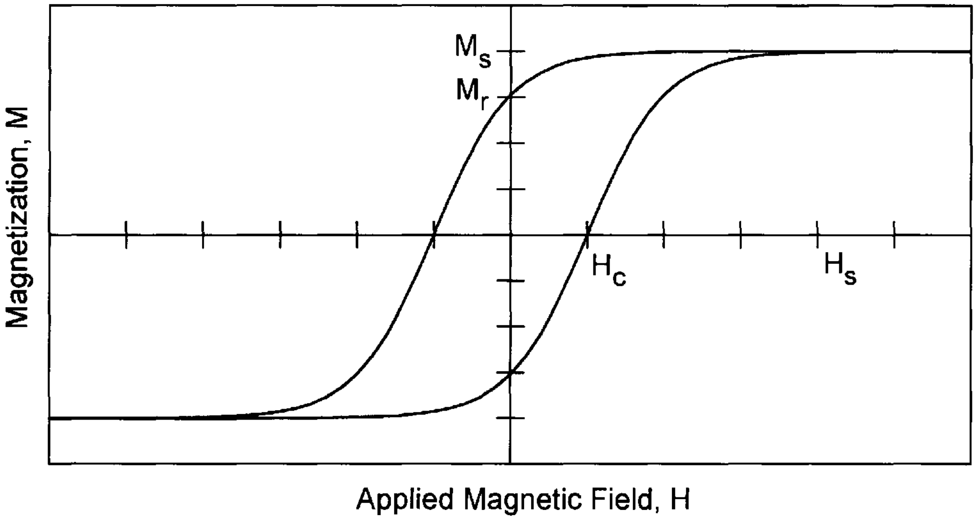

Figure 3.11: *A Typical hysteresis curve. M is the magnetization and H is the applied magnetic field.*

ac Magnetic Susceptibility

Magnetic susceptibility χ is a measure of the response of the magnetic material to an applied magnetic field. It is defined as the relative change of the magnetization δM to the change of the magnetic field δH:

$$\chi = \frac{\partial M}{\partial H}. \tag{3.10}$$

In theory, the linear susceptibility is the response to an infinitesimally small field. To first order χ is the slope of a hysteresis curve at zero field. In fact χ is a tensor quantity, but most often M and H are parallel and the only diagonal elements of χ are measured.

To measure the ac susceptibility, an ac magnetic field H_{ac} is applied to a sample and the resulting ac magnetic moment is measured. Because the induced sample moment is time-dependent, ac measurements yield information about the magnetization dynamics which are not obtained in dc measurements. For this reason, the ac susceptibility is often known as the dynamic susceptibility. When an ac magnetic field

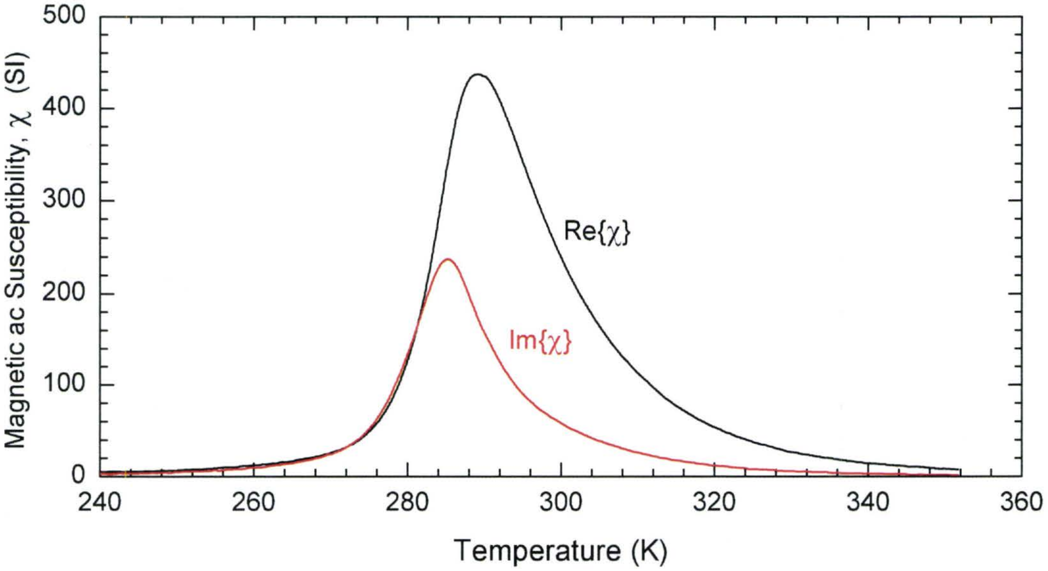

Figure 3.12: *A typical ac magnetic susceptibility measured of 1.5 ML Fe deposited on top of 2 ML Ni/W(110).*

is applied, the magnetization of the sample may lag behind the applied field. Thus, the ac magnetic susceptibility is composed of two components; an in-phase, or real component χ' and an out-of-phase, or imaginary component χ'' ($\chi = \chi' + i\chi''$). A typical ac magnetic susceptibility measurement of 1.5 ML Fe deposited on top of 2 ML Ni/W(110) substrate is shown in Fig. 3.12.

3.5.2 Surface Magneto-Optic Kerr Effect (SMOKE)

The magneto-optic Kerr effect (MOKE) is a common technique used to investigate the static and dynamic properties of a ferromagnetic sample. This effect is named after John Kerr who observed a rotation of the plane of the polarization of linearly polarized light when it is reflected from a polished magnetic iron plate in the presence of an external magnetic field. In the so-called *volume* MOKE, the thickness of the sample is greater than the penetration depth of the light. Thus only the magnetization of the sample (M) is responsible for the measured magneto-optic effect. But in

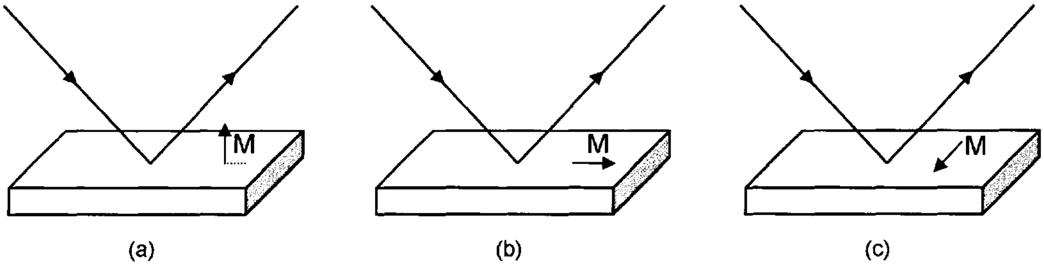

Figure 3.13: *Three basic configurations of Kerr effect: (a) Polar, (b) longitudinal, and (c) transversal*

the case that the thickness is smaller than the penetration depth of the light (100-200 Å), the thickness of the sample plays an important role to determine the size of the effect. This last case is termed the surface magneto-optic Kerr effect (SMOKE). Experiments utilizing the surface magneto-optic Kerr effect technique have contributed to substantial progress in the area of magnetism of ultrathin film structures. Such contributions are the understanding of ultrathin film critical phenomena ([82, 83] *and references therein*) and spin reorientation transition (SRT) phenomena ([35] *and references therein*). The technique is popular due to its high sensitivity, local nature, and experimental simplicity [84–86].

The Kerr effect can be measured using three different geometric configurations. These are the polar, longitudinal, and transverse configurations, which described three high-symmetry geometries as shown in Fig. 3.13. In the polar geometry, the magnetization direction is perpendicular to the film plane, thus the effect is sensitive to the perpendicular component of the magnetization. In the longitudinal Kerr effect, the magnetization is in the film plane and also in the plane of the incident light, and thus is sensitive to the in-plane component of the magnetization. In the transverse Kerr effect, the magnetization is also in the film plane but perpendicular to the plane of incident light.

3.5.3 Origin of Magneto-Optic Kerr Effect

The principle of the magneto-optic Kerr effect is depicted in Fig.3.14. Linearly polarized incident light obtains a Kerr rotation and a Kerr ellipticity upon reflection from a magnetized sample. Macroscopically, the effect can be described by the dielectric tensor ϵ, which contains off-diagonal terms. In the most general case, where the angle of the incident light with respect to the magnetization has an arbitrary direction, the dielectric tensor has the following form:

$$\epsilon = \epsilon_o \begin{pmatrix} 1 & iQ_z & -iQ_y \\ -iQ_z & 1 & iQ_x \\ -iQ_y & -iQ_x & 1 \end{pmatrix} \tag{3.11}$$

where $\boldsymbol{Q} = (Q_x, Q_y, Q_z)$ is the magneto-optic Voigt vector, which can be written as a function of the directional cosine of the magnetization vector. Linearly polarized light can be decomposed into left-handed circularly polarized light with a refractive index $n_L = n(1\text{-}(1/2)\boldsymbol{Q}\cdot\hat{\boldsymbol{k}})$, and a right-handed circularly polarized light with refractive index $n_R = n(1+(1/2)\boldsymbol{Q}\cdot\hat{\boldsymbol{k}})$, where n is the refractive index of the material and $\hat{\boldsymbol{k}}$ is the unit vector along the direction of light propagation. Therefore the two circular modes travel in the magnetized medium with different velocities and are attenuated differently. Thus, upon emerging from the magnetized medium after reflection, the two altered modes recombine to yield a rotated axis of polarization and ellipticity (see Fig.3.14). The rotation and ellipticity are called the Kerr rotation and the Kerr ellipticity, respectively. The Kerr rotation θ_K is the angle between the polarization plane of the incident light and the major axis a of the ellipse. The Kerr ellipticity is by definition $\epsilon_K = b/a$, where b is the minor axis of the ellipse. Consequently, both angles may combine to form the complex Kerr angle:

$$\Phi_K = \theta_K + i\epsilon_K. \tag{3.12}$$

The complex Kerr angle in ultrathin films can be calculated if the film thickness d is

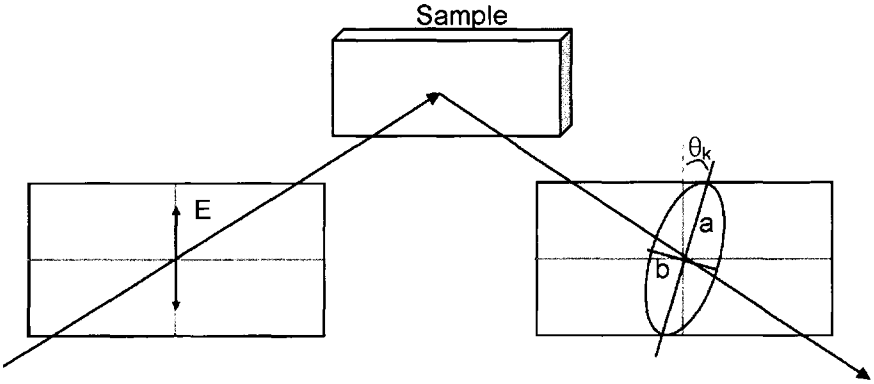

Figure 3.14: *Magneto-optic Kerr effect. Upon reflection of linearly polarized light from a magnetized sample, an elliptical polarization and rotation of the polarization plane occur.*

much smaller than the wave length λ of the incident light, that is the ultrathin film condition is satisfied [86]:

$$\frac{2\pi}{\lambda}|n|d \ll 1, \tag{3.13}$$

where n is the refractive index of the film. In this case, the Kerr angle for the longitudinal and polar Kerr effect is given respectively by [86]:

$$\phi_K^L = sin(\theta)\left(\frac{4\pi}{\lambda}\right)\left(\frac{n_{sub}}{1-n_{sub}^2}\right)Qd, \tag{3.14}$$

$$\phi_K^P = -cos(\theta)\left(\frac{4\pi}{\lambda}\right)\left(\frac{n^2}{1-n_{sub}^2}\right)Qd, \tag{3.15}$$

where θ is the incident angle of the light, and n_{sub} is the refractive index of the substrate.

3.5.4 SMOKE Measurement Techniques

A schematic illustration of SMOKE setup is shown in Fig. 3.15. Linearly polarized light from a HeNe laser passes through Glan-Thomson polarizer (P1) and UHV window (W1) and is incident upon the magnetic film surface. Subsequently it is reflected

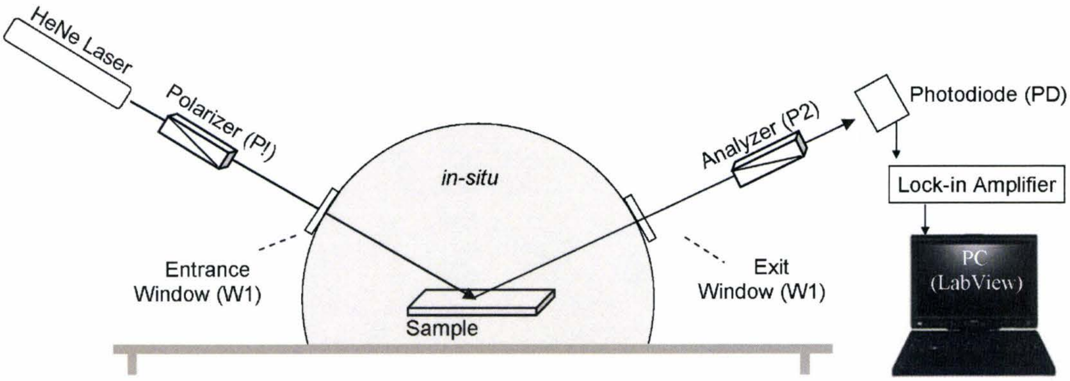

Figure 3.15: *Schematic illustration of SMOKE setup.*

from the magnetic film and passes through an exit UHV window (W2) and a second polarizer (P2) (The analyzer). The analyzer is oriented near extinction, so that only the magneto-optically rotated component of the polarization vector is transmitted. The change in the polarization state of the transmitted light is detected by the photodiode (PD) as a change in light intensity.

The intensity of the light passing through the two polarizer obeys

$$I(\theta) = I_{max}(\sin^2\theta + \epsilon), \tag{3.16}$$

where θ is the angle from extinction ($\theta = 0$ when the polarizers are crossed), I_{max} is the maximum intensity falling on the photodiode for a parallel polarizers, and ϵ is the extinction ratio. The extinction ratio, as may be evident from the above equation, is the proportion of the maximum intensity that passes through the crossed polarizers, and it is a measure of the quality of both polarizers. For a small rotation of the polarization ϕ_K ($\sim \delta\theta$), the relative change (*contrast*) in the dc intensity of the light transmitted from the analyzer is

$$\frac{\delta I}{I} = \frac{2\theta\phi_K}{\theta^2 + \epsilon}. \tag{3.17}$$

The contrast is maximized when the analyzer is set to an angle $\theta_m = \sqrt{\epsilon}$ from the extinction, and is given as

$$\frac{\delta I}{I} = \frac{\phi_K}{\sqrt{\epsilon}}. \tag{3.18}$$

Thus the extinction ratio ϵ is desired to be as small as possible to give the best sensitivity.

The UHV windows (W1, and W2) are composed of quartz which will become optically birefringent when put under stress. Thus they will introduce an ellipticity to the linearly incident light that is significantly increases the extinction which in turn affects the sensitivity of the measurement. This unwanted ellipticity can be compensated as follows [87]. The initial polarizer is first set to either S- or P- polarization state and the analyzer is set to extinction (minimum intensity) and the extinction ratio is measured. The initial polarizer angle is then changed by few tenths of a degree, and the analyzer is reset for the extinction. If the extinction ratio improves, the procedure is repeated. If degrades, the rotation is made in opposite sense. Iteration continues until a minimum is found in the extinction ratio (typically on the range of 10^{-7}-10^{-6}).

For the dc measurement of magnetic hysteresis curves the intensity is measured at constant temperature as a function of the applied magnetic field. The field in our apparatus can be applied either perpendicular to the plane of the film or in-plane along one direction by passing current through Helmholtz coils mounted about the sample. The field is allowed to vary quickly and the response is averaged over several field cycles.

The optical setup for the magnetic ac-susceptibility (χ) measurement is the same as for the dc measurement of the hysteresis curve. In this technique, the susceptibility is measured using a small oscillating (hence the term "ac") magnetic field produced by Helmholtz coils. The intensity at the photodiode is detected by a Lock-In amplifier, which measures the intensity only at the same frequency of the applied field. The use of the digital Lock-In allows a simultaneous measurement of the two components of the susceptibility: the real component (in phase of the applied field) and the imaginary component (out of phase of the applied field). For this study, the susceptibility is measured with the application of a small magnetic field of 2 Oe with modulation frequency of 210 Hz.

To optimize the signal-to-noise (S/N) ratio in the ac measurement, the analyzer is set to an angle $\theta = 10$ arcminutes[1] from the extinction [34]. This optimization angle is different from the one used in the dc measurements ($\theta = \sqrt{\epsilon}$). This is due to more complicated frequency-dependent signal-to-noise issues that arise in the ac technique. In the ac technique, the S/N ratio is a function of set angle that has a maximum at a certain angle. For more details of the optimization of the (S/N) ratio in the ac measurements, the reader is referred to [34, 88].

In this study, the susceptibility is expressed as a unitless quantity (in the SI unit system) by the calibration of the photodiode ac voltages to a corresponding rms ac modulation of magneto-optic rotation ϕ_{ac} ($\sim \Delta\theta$), which is proportional to the slope of Eq. 3.16

$$\phi_{ac} = \frac{\Delta I}{2\theta I_{max}}, \tag{3.19}$$

where ΔI is the ac intensity transmitted to the photodiode. This is then approximately converted to SI units of the susceptibility as

$$\chi = \left(\frac{4\pi}{1000}\right) \frac{M^{sat}}{H_a \phi_K^{sat} d} \phi_{ac}, \tag{3.20}$$

where M^{sat} is the saturation magnetization for the bulk Fe in cgs units, ϕ_K^{sat} is the Kerr rotation per monolayer at saturation evaluated from the static hysteresis curve, H_a is the applied field (in Oe), and d is the film thickness in monolayer. The prefactor of $(4\pi/1000)$ is to convert from the cgs to SI units.

To study the domain dynamics in perpendicularly magnetized ultrathin films, two types of susceptibility measurements are made. The susceptibility is measured

---

[1] After the completion of the experimental work of this study, Fritsch [88] has found the optimization angle for a new optical setup is $\theta = 24$ arcminutese

as a function of temperature while changing the temperature at constant rate (R), or at constant temperature as a function of time. The last type of measurement is made after reaching the temperature setpoint at a certain constant rate. Another possible susceptibility measurement (not made in this study) can be made at constant temperature as a function of time after the removal of applied dc field that drives the film to the saturation.

The sample temperature is varied by cooling the sample holder with a copper braid extending to a liquid nitrogen reservoir, and by heating with radiation from a filament behind the substrate. A homemade (PID) temperature controller is used for maintaining the sample temperature at setpoint (T_{set}) by controlling heating input in accordance with both a proportional and reset response from the temperature deviation ($T_{set}-T$). The rate of changing temperature is regulated to better than 0.05(K/s) in the range of [-0.1 - 1.0(K/s)](see Fig. 3.16). The temperature rate controller is the same as the temperature controller but with time varying temperature setpoint, $T_{set}(t)$, according to:

$$T_{set}(t) = T_0 + Rt, \tag{3.21}$$

where t is time, R is the heating/cooling rate and T_0 is the sample temperature at $t = 0$. In case of controlling the cooling rate (- value of R), the sample cooling rate is made larger than the desired cooling rate and then the heat input is determined by the temperature deviation ($T_{set}(t) - T$) to slow down the cooling to a constant rate. The maximum cooling rate that can be controlled with our apparatus is -0.1(K/s).

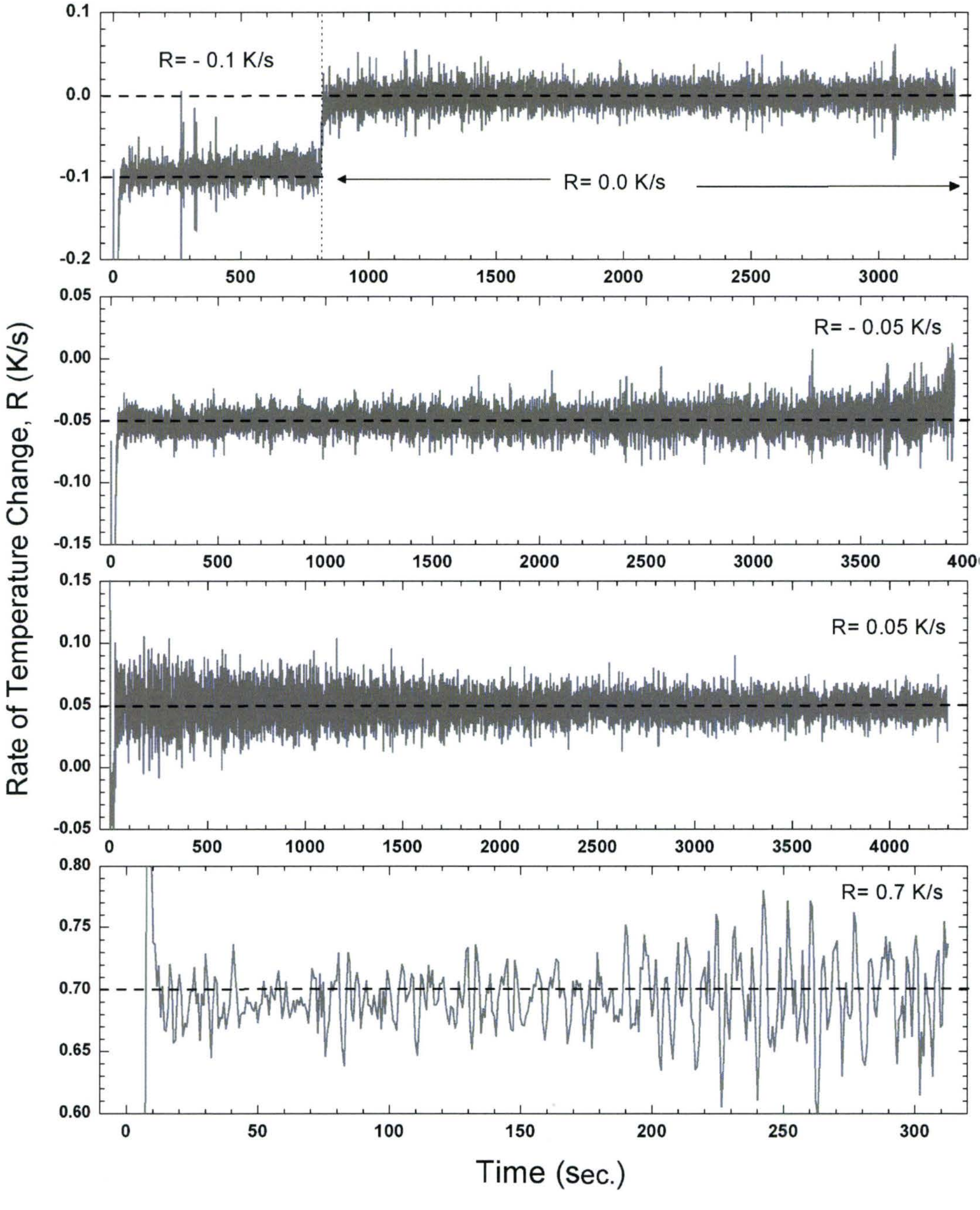

Figure 3.16: *Rate of changing temperature as a function of time. The figure at the top shows that the sample temperature was controlled to decrease at a constant rate of -0.1*(K/s) *down to a certain temperature at which the sample temperature is kept constant* $(R = 0(K/s))$. *Dashed line represents the average value of* R.

Chapter 4

Results and Discussion

4.1 Introduction

A stripe domain structure with alternating up and down domains has been predicted [14–16, 21, 22, 72] and observed [6, 30–32] in magnetic films possessing perpendicular magnetic anisotropy. Such systems exhibit various domain phases in different temperature regimes. At low temperature, the *ordered stripe* phase is the ground state. In this phase, the domains have both orientational and positional order. At higher temperature, fluctuations in the domain walls minimize the free energy by breaking the ordered domains into segments which may not be aligned along a single axis. Regions with local orientations represent topological defects in the domain structure that result in the loss of the orientational and positional order of the domains at high temperature range. A number of possible domain phases of this type (Ising nematic phase, tetragonal phase) are referred to as "delocalized phases".

Recent numerical studies [24, 26, 27] have suggested that the ordered stripe phase and the delocalized phases may be distinguished by their relaxation dynamics. This can be seen in two ways. Bromley *et al.* [24] found that if the ground state is the delocalized state, relaxation from a magnetically saturated state proceeds over a single short time scale by the rapid decay of the magnetization. However, if the ground state is the ordered stripe state, the relaxation from the saturated state exhibits three distinctive regimes; domain walls nucleation (or creation) that is characterized by a short time scale, domain density equilibration via domain growth and/or shrinkage that proceeds over an intermediate time scale, and finally a relaxation process that aligns domains along a common axis by the annihilation of topological defects in the domain structure. A similar signature is observed in numerical studies by Cannas *et al.* [26, 27] for moving between equilibrium phases across a phase transition. They found that when cooling the system from high temperature, where the delocalized phase is the equilibrium phase, to a low temperature where the ordered stripe phase is the equilibrium phase, the topological defects in the delocalized phase act as a pinning source for the phase transformation process. The quenched delocalized state is then found to relax very slowly to the truly equilibrium ordered stripe state, via two kinds of process that are indicative of a discontinuous transition.

The present work provides an experimental study of the relaxation processes in perpendicularly magnetized ultrathin fcc Fe/ 2 ML Ni(111)/ W(110) films by using the magnetic ac susceptibility. Previous studies [37–39] at frequencies of the order of 10^2 Hz have allowed a quantitative description of domain wall pinning mechanisms in these films. This study investigates relaxation mechanisms that proceeds over much longer time scales. Different time scales have been accessed by altering the constant rate of temperature variation, R, as the susceptibility is scanned. The susceptibility measurements are made as a function of temperature and/or time.

The following section will review the experimental procedure, and discuss the steps taken to remove systematic errors from the measurements.

4.2 Experiment

4.2.1 Film Preparation

Ultrathin Fe films were grown on a 2 ML Ni(111)/W(110) substrate and characterized in ultrahigh vacuum (UHV) system with a base pressure of better than 5×10^{-10} Torr. Prior to each film growth, the W(110) single crystal was cleaned by cycles of heating to over 1500 K in an oxygen atmosphere, and then flashing to 2500 K. Oxygen cleaning is especially effective for removing carbon, which is the major contaminant in W. No experiment proceeded unless no evidence of carbon was detectable. The 2 ML fcc Ni buffer is used to initiate an fcc growth of Fe films with a thickness of up to 3 ML, after which the Fe undergoes a gradual transformation to the bcc phase, which is completed by 12 ML [5].

Fe and Ni films were grown by molecular beam epitaxy (MBE) from pure wires and their thickness and quality were monitored by Auger electron spectroscopy (AES) and low-energy electron diffraction (LEED). The growth of the films and their structure are described in detail by Johnston *et.al.* [5]. The first layer of Ni was deposited on the W substrate at an elevated temperature of 550 K and was then annealed to 600 K for 2 minutes to ensure a flat, smooth atomic layer. A second Ni layer was deposited at substrate temperature of 390 K without further annealing. The 1 ML coverage was always verified by measuring the attenuation of the W AES signal in the 150-190 eV range, known to be 0.55 for 1 ML of Ni [5]. The Fe film was grown on the 2 ML Ni buffer at a substrate temperature of 360 K and was then annealed to 400 K for 2 minutes. The Fe evaporation rate was calibrated by Auger analysis of an experiment where a bcc Fe film is deposited directly onto the W(110) surface at room temperature. The evaporation time required for a completion of the bcc monolayer is τ_{bcc}, and corresponds to an attenuation of the W AES signal by 0.60 [5]. The time required for the deposition of Fe equivalent to one pseudomorphic fcc layer on Ni(111) is calculated as $\tau_{\mathrm{fcc}} = 1.3\tau_{\mathrm{bcc}}$ [5]. Film thicknesses were certain to within ±0.1 ML.

4.2.2 Magnetic ac-Susceptibility Measurements

In the present study, the ac-susceptibility measurements were made by using the surface magneto-optic Kerr effect (SMOKE) as follows. Linearly polarized light from a He-Ne laser passes through an UHV window, and is incident on the magnetized film at angle of 45° to the surface normal. At the same time, an oscillating magnetic field of frequency $\omega = 210$ Hz and a field amplitude of 2.0 Oe, is applied perpendicular to the film surface. Upon reflection from the film surface, the polarization state of the light is rotated due to the Kerr rotation produced by SMOKE. The reflected light passes through an exit UHV window and then a polarizer almost crossed with the incident polarization. The change in the polarization state results in a change in light intensity which in turn is detected as a change in output voltage from a photo-diode detector. A dual-phase lock-in amplifier is used to collect the change in photo-diode intensity at frequency ω, which is proportional to the complex magnetic susceptibility. The susceptibility measurements presented in this study are recorded either as a function of temperature while changing the temperature continuously at different constant rates (R), or as a function of time at constant temperature. In each case where the susceptibility was measured while heating, the sample was first cooled at a controlled rate of -0.1 K/s, starting at or above room temperature. Data as presented (measured in a sequence of points separated by 0.5 sec.) have been binned in 0.5 K increments, and converted approximately to SI units according to Eq. 3.20. For all experiments the earth's magnetic field was compensated down to better than 10^{-2} Oe.

4.2.3 Avoiding Systematic Errors

In practical experiments, there are a number of pertinent time scales other than the time scale that is set by the rate of change of temperature. One of these is the time constant of the lock-in amplifier. Lock-in amplifiers perform a finite-time Fourier transformation of a measured ac signal, *locked-in* to the reference signal at the reference frequency ω. The input signal (S_{in}) is combined with a normalized signal proportional to the reference signal $\mathrm{e}^{i\omega t}$. The output signal (S_{out}) from the lock-in can be calculated by:

$$S_{out}(t) = \frac{1}{\tau} \int_{t-\tau}^{t} e^{\frac{t'-t}{\tau}} e^{i\omega t'} S_{in}(t') dt', \tag{4.1}$$

where τ is the lock-in amplifier time constant. A short time constant allows the lock-in amplifier to track the input signal quickly but at the cost of displaying high frequency noise. A long time constant results in less high frequency noise in the output signal, but the measurement cannot follow rapid changes in the signal. The effect of the lock-in amplifier time constant on the measured susceptibility was investigated by measuring the susceptibility as a function of temperature while changing the temperature at a heating rate of 1.0 K/s [1], with the lock-in time constant set at different values between 0.5 (s) and 10 (s). The result of this investigation is presented in Fig. 4.1. As long as the time constant is $\tau \leq 2$ (s), the output signal is independent of τ. In all subsequent experiments, the lock-in time constant was set to the value of $\tau =$ 2 (s) in order to reduce noise.

In our apparatus, the sample temperature is measured using a W5%Re-W20%Re thermocouple embedded in the W(110) crystal. The sample heating was accomplished by radiation from a heated tungsten filament located behind the substrate. In the case of cooling, the sample is cooled by cooling the sample holder using a copper braid extending to a liquid nitrogen reservoir. If the cooling rate is larger than the desired

---

[1] 1.0 K/s is the largest heating rate that has been used in this study.

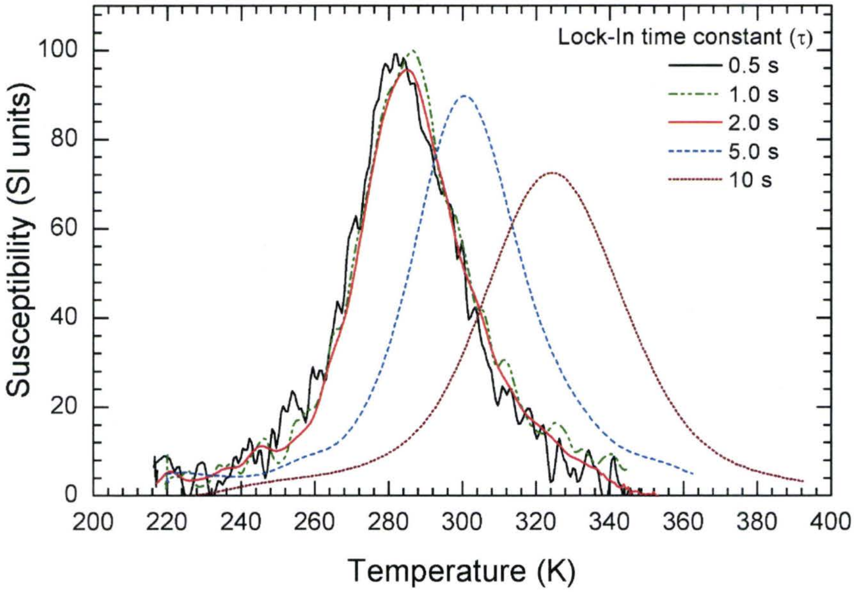

Figure 4.1: *Magnetic ac-susceptibility of a 1.5 ML Fe/2 ML Ni/W*(110) *film as a function of temperature while increasing the temperature at the rate of 1.0 K/s, measured at different lock-in time constants* τ

rate, the sample is heated to slow down the cooling to the desired cooling rate. The desired cooling rate, other than noted, was 0.1 K/s, which is the largest accessible constant cooling rate over the entire temperature range in which the susceptibility was measured.

The distance between the point at which the temperature is measured and that at which the magnetic response was measured is approximately 0.7 cm (Fig. 4.2). This may cause a difference between the actual film temperature and the measured temperature since thermal conduction through the substrate requires a certain time. For an experiment with a constant rate of change in temperature, this will effectively shift the temperature scale. Calculation of the thermal time constant τ_{th} will quantify this effect. This can be done by solving the heat equation:

$$\frac{\partial T}{\partial t} = \frac{k}{C_v \rho} \frac{\partial^2 T}{\partial x^2}, \tag{4.2}$$

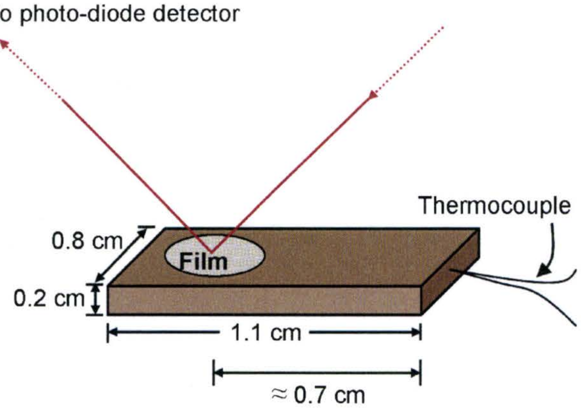

Figure 4.2: *A Schematic graph shows the size of W substrate and the relative positions of the two points at which the temperature and the magnetic response are measured.*

where k is the thermal conductivity, C_v the specific heat, and ρ the mass density of W. The temperature at position x at a given time t is then

$$T(x,t) = T_0 + \sum_n D_n \sin(\frac{(2n+1)\pi}{2l}x) \exp(\frac{-t}{\tau_{th}(n)}), \tag{4.3}$$

where T_0 is the initial temperature, l the total length over which the temperature is distributed, and D_n is a constant with index n. The thermal time constant $\tau_{th}(n)$ is given by:

$$\tau_{th}(n) = \frac{4lC_v\rho}{(2n+1)^2\pi^2 k}. \tag{4.4}$$

By substituting the material constants of tungsten, the largest thermal time constant would be in the order of 0.1 s. Therefore, the shift in the temperature scale would be $R\tau_{th} \approx 0.1$ K for a heating rate of 1.0 K/s. This is well within the reproducibility of the measurement of the susceptibility which is discussed in the next paragraph.

Reproducibility is a common standard for scientific data. If experimental or descriptive data cannot be reproduced within an acceptable error, under identical conditions, then they are generally discarded. This is especially true in this study since the susceptibility trace is measured many times at a different rates of change in temperature. If the trace measured at a given rate is not reproducible, it would not be possible to go any further in the experiment. Figure 4.3 shows the degree to which the susceptibility measurement is reproducible. Figure 4.3(a) shows three repeated measurements of the susceptibility trace measured while heating at a rate of 0.2 K/s, and Fig. 4.3(b) shows the susceptibility peak temperature that is plotted as a function of the order of the measurements. This should make it clear that differences in the susceptibility traces that are measured at different rates of change in temperature are not a result of the irreproducibility of the measurements. Furthermore, the temperature errors due to thermal conduction are an order of magnitude smaller.

Another possible systematic error in our experiments is that the film quality degrades with time. The films were prepared and characterized *in situ* with a base pressure in the range of 10^{-10} Torr. Pressure at this extremely low level allows for several hours of experimental time before contamination sets in and possibly changes the film properties. The total time for many susceptibility measurements from a single film was between 4 and 6 hours, depending on the type of the experiment. The results of an investigation of the dependence of the susceptibility traces on the film age are shown in Fig. 4.4. In Fig. 4.4.(a), the susceptibility peak temperature is plotted as a function of elapsed time before the susceptibility measurement was made from 1.5 ML Fe/ 2 ML Ni/W(110) film while heating at rate of 0.1 K/s. Fig. 4.4.(b) replots the data of Fig. 4.3 as a function of the film age. It is clear that the contamination has a strong effect on the film properties, but *not* for experiments that are completed in less than 6 hours.

In conclusion these systematic errors have a minor effect or are insignificant.

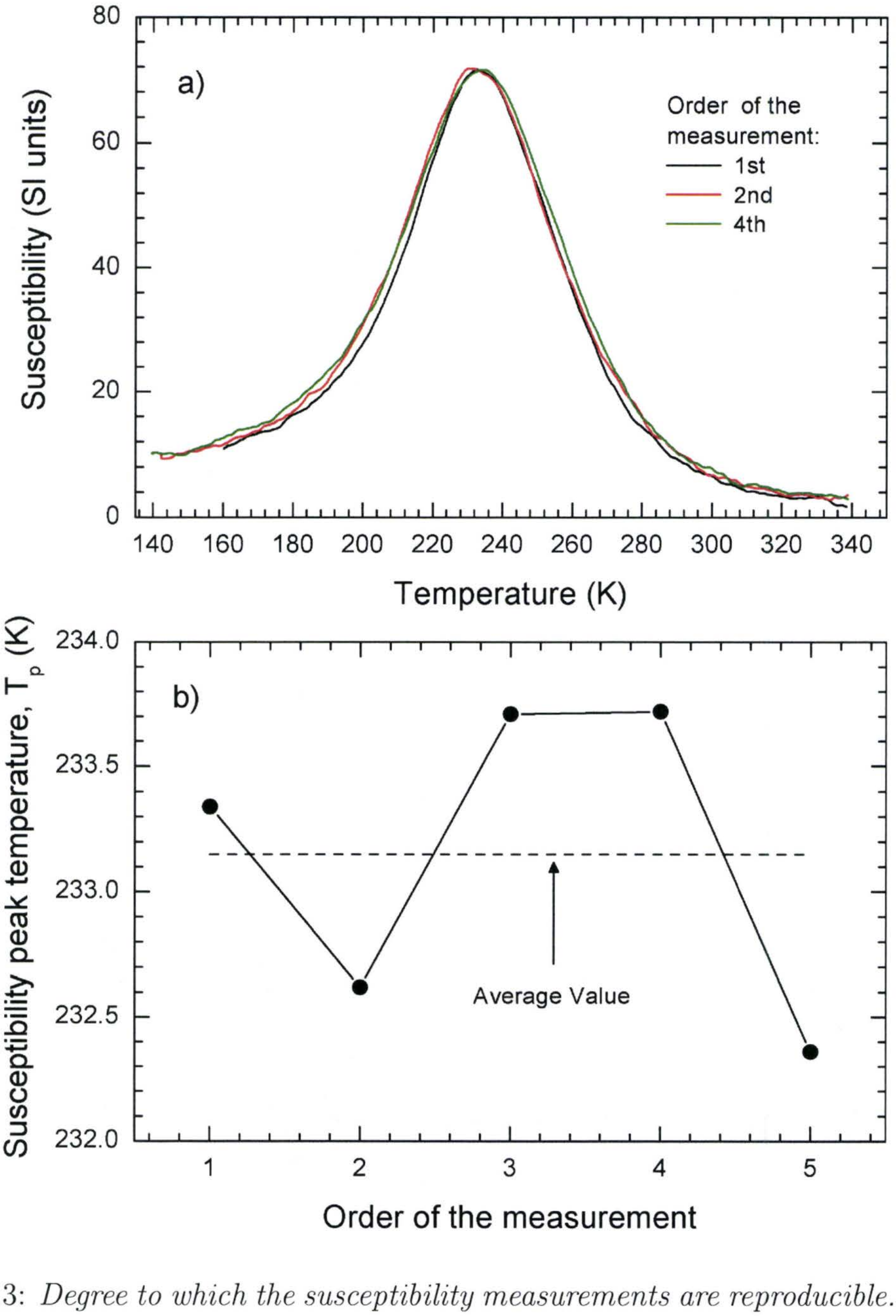

Figure 4.3: *Degree to which the susceptibility measurements are reproducible. (a) three repeated measurements of the magnetic ac-susceptibility as a function of temperature measured while heating at rate of 0.2 K/s, and (b) susceptibility peak temperature, (T_p) as a function of the order of the susceptibility measurements.*

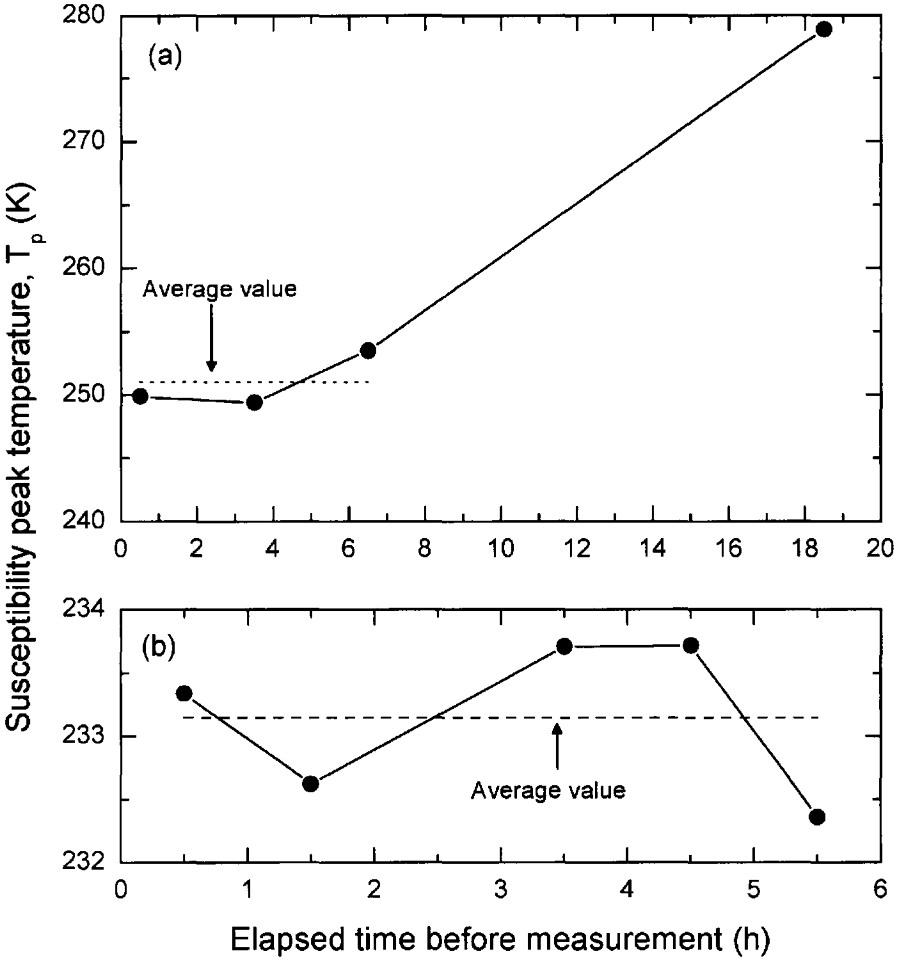

Figure 4.4: *Susceptibility peak temperature, T_p as a function of elapsed time before the measurement was made from (a) 1.5 ML Fe/ 2 ML Ni/W(110) while heating at a rate of 0.1 K/s and from (b) 2.0 ML Fe/ 2 ML Ni/W(110) while heating at a rate of 0.2 K/s.*

4.3 Results and Discussion

In this study, the susceptibility measurements were made from ultrathin film Fe, grown on a 2 ML/ Ni(111)/W(110) substrate, with thicknesses smaller than 2.2 ML. This is to eliminate any contribution that might arise from the spin reorientation transition observed with a thickness greater than 2.2 ML [35]. Figure 4.5 shows the two components, real and imaginary parts, of the complex magnetic ac-susceptibility measured from 1.25 ML Fe/ 2 ML/Ni/W(110) film, whereas Fig. 4.6 shows only the real part of the susceptibility measured from 1.75 ML Fe/ 2 ML/Ni/W(110). The imaginary part of the susceptibility measured from this film is shown in the appendix along with the complex susceptibility of other films studied here. The susceptibility was measured using an applied field with an amplitude of 2.0 Oe and frequency of 210 Hz, and is recorded as a function of temperature while changing the temperature at constant heating rate (R). In each case where the susceptibility was measured by heating from low temperature, the sample was first cooled from 360 K at a rate of R = -0.1 K/s. The susceptibility measurements were made in an arbitrary order of R. Figure 4.7 shows the susceptibility peak temperature (T_p) plotted as a function of the heating rate (R) for different thicknesses, and Fig. 4.8 shows the corresponding variation of the susceptibility full width-at-half-maximum (FWHM) with R.

Having presented some of the results, the discussion will be divided into two parts. In the first part, I will discuss qualitatively the dependence of the susceptibility on the film thickness, while in the second part, I will discuss the dependence of the susceptibility on the heating rate, which is the main subject of this study.

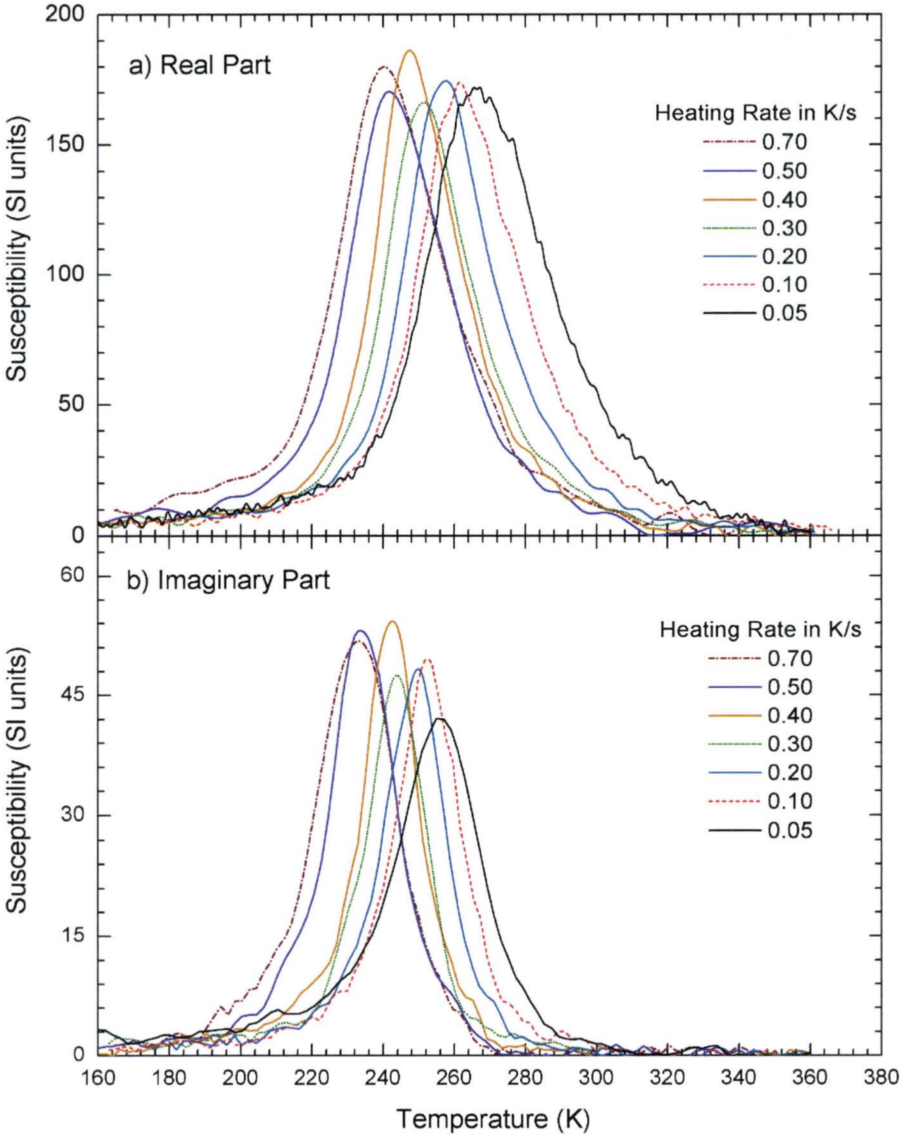

Figure 4.5: *The ac magnetic susceptibility of 1.25 ML Fe/ 2 ML Ni/W*(110) *film as a function of temperature while changing the temperature at different heating rates. Both the* (*a*) *real and* (*b*) *imaginary parts of the susceptibility are shown.*

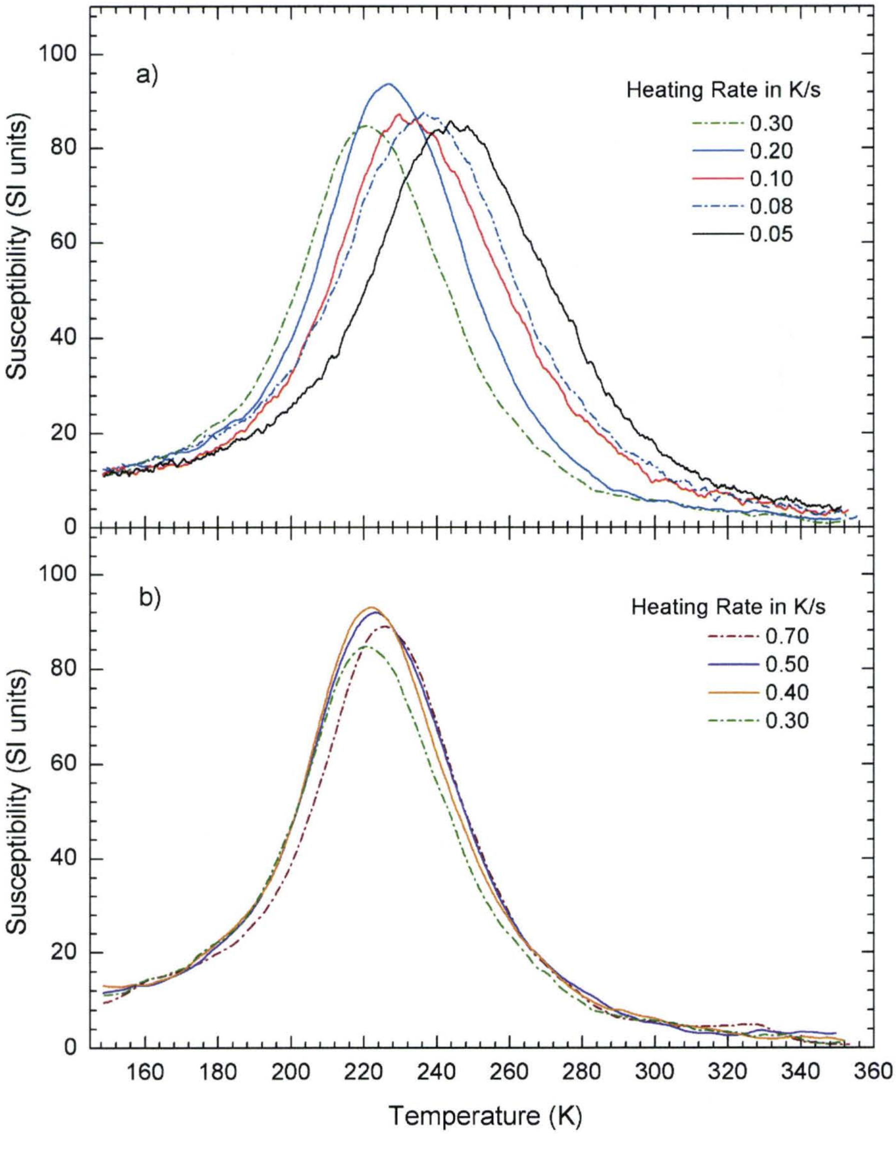

Figure 4.6: *The real part of the ac magnetic susceptibility of 1.75 ML Fe/ 2 ML Ni/W(110) film as a function of temperature, measured at different heating rates. In (a) the susceptibility trace shifts to lower temperature as the heating rate increases up to* $R_C = 0.3(K/s)$. *For* $R > 0.3(K/s)$ *the trace starts to shift to higher temperature as shown in (b).*

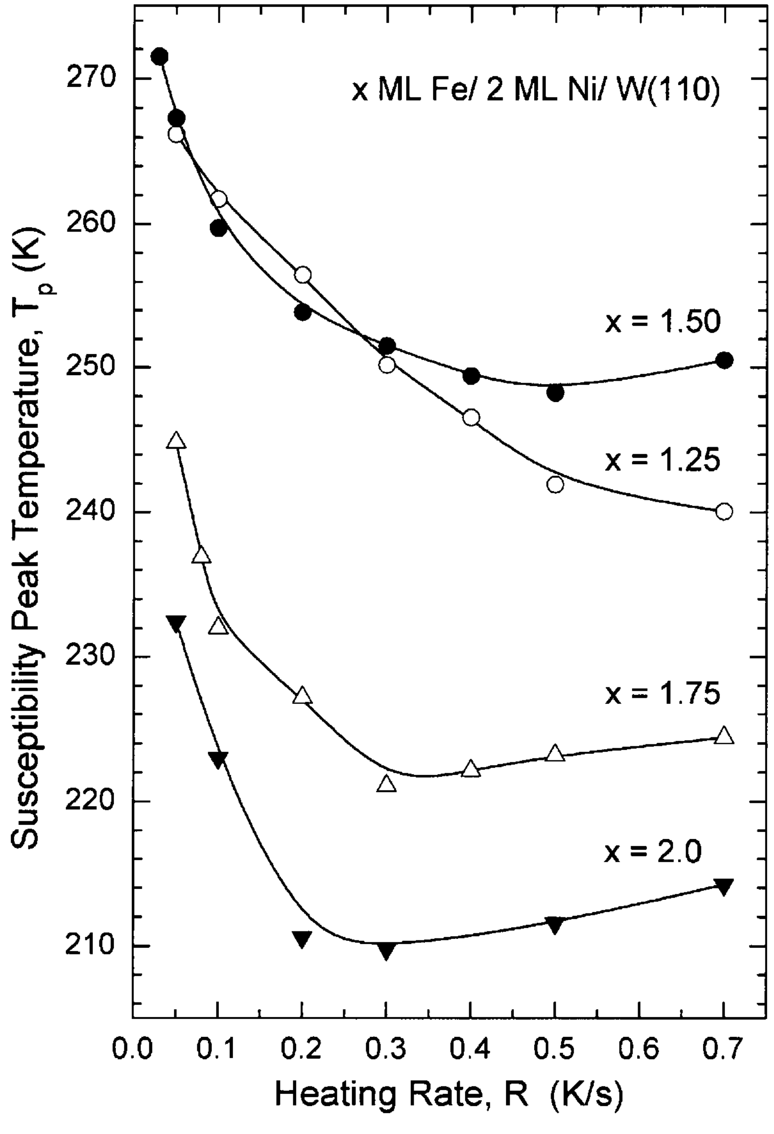

Figure 4.7: *Peak temperature of the real part of the susceptibility as a function of the heating rate R for different film thicknesses (x in monolayer, ML). Solid line serves as guide to the eyes.*

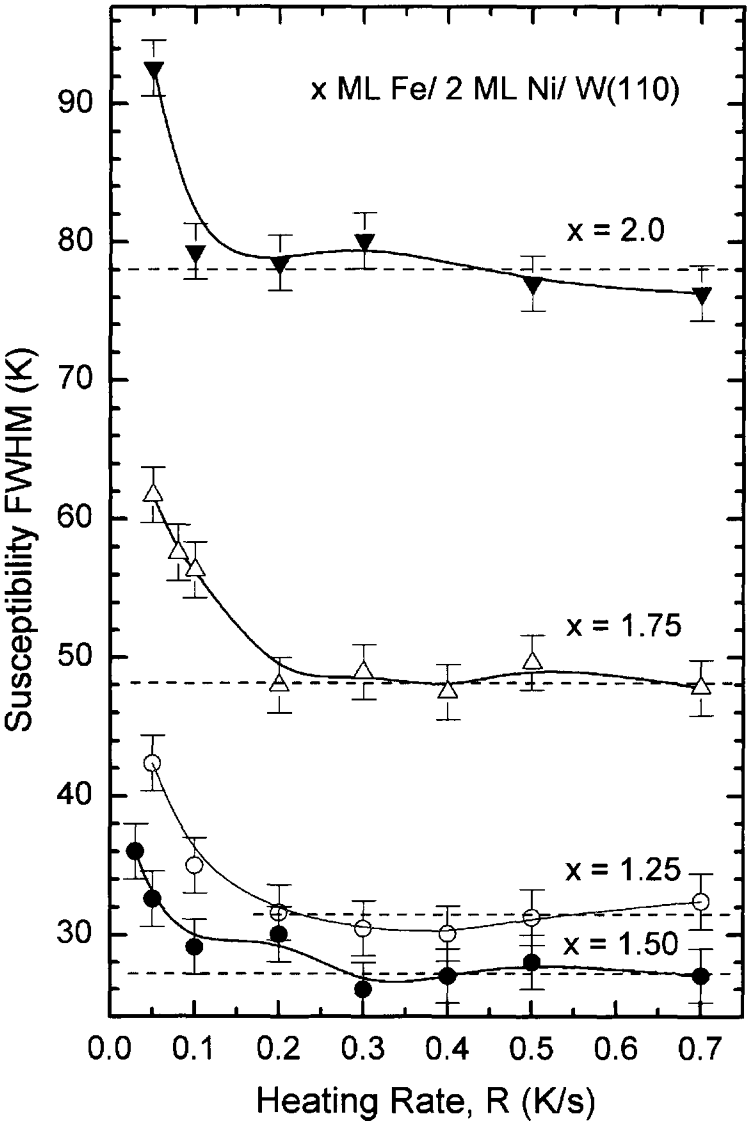

Figure 4.8: *Full-width-at-half-maximum of the real part of the susceptibility as a function of the heating rate R for different film thicknesses (x in monolayer, ML). Solid line serves as guide to the eyes.*

4.3.1 Thickness Dependence Of The Susceptibility

In comparison with a previous study [38], the susceptibility curve peaks at lower temperature for film thickness range studied here (see Fig. 4.9(a)). However, the susceptibility peak temperature, with the exception of data from 1.25 ML film, follows the same trend as thickness increases, that is the peak temperature decreases as thickness increases. This trend can be explained by the domain wall pinning mechanism. As has been shown in section 2.8, the peak should occur at a temperature according to the condition:

$$\omega\tau_{0a}\exp(\frac{E_a}{k_B T}) \approx 1, \tag{4.5}$$

where ω is magnetic field frequency and E_a is the "activation" energy needed for a microscopic section of domain wall to escape from a pinning site when a magnetic field is applied [37, 38, 43]. In section 2.8, it has been argued that the pinning may be caused by the variations in domain wall energy due to the variations in domain wall thickness at monolayer steps, as this can represent a large proportion of the total thickness. As the film thickness increases, the relative size of monolayer steps to the thickness becomes less. This in turn results in a smaller activation energy. Indeed, Venus *et.al* [37] have found that the variation of the activation energy with the film thickness is very well described with Eq. 2.56 (see Fig. 4.9). This is in agreement with the theory of Bruno *et al.* [43]. This implies the condition of Eq. 4.5 holds at lower temperature for a thicker film. Unfortunately, the analysis made by Venus *et.al* [37] cannot be followed in this study since very few points are available (square symbols), and the films studied here were prepared independently and thus have a different microscopic structure which changes the domain wall pinning [37, 38].

The shift of the susceptibility curve to lower temperature with thickness is associated with a broadening of the curve. Figure 4.8 illustrate the dependence of the susceptibility FWHM (a quantitative measurement of the broadening) as a function

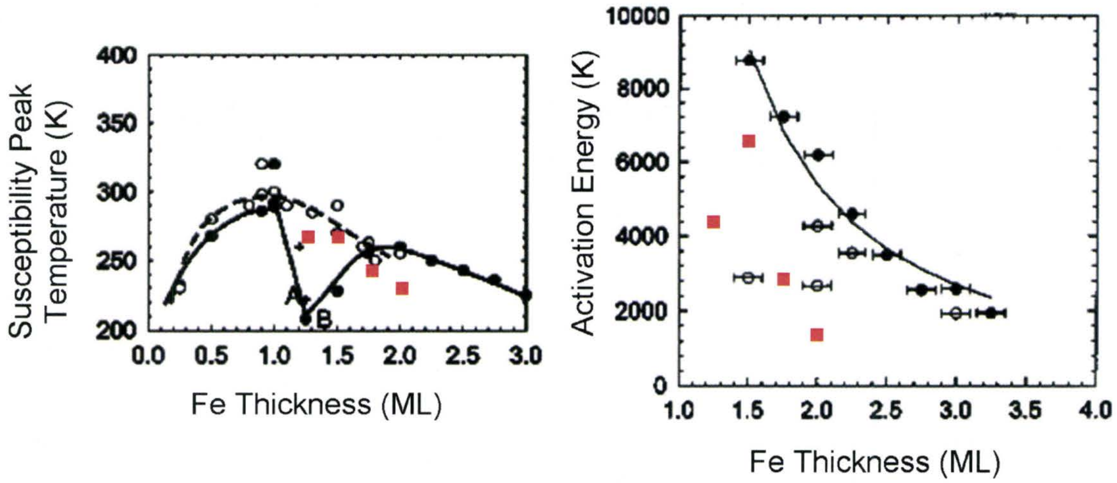

Figure 4.9: (*a*) *Peak temperature of the real part of the susceptibility is plotted as a function of the Fe thickness. Open circles and solid circles are data from Ref. [38] and Ref. [35] respectively (the graph is taken from Ref. [38]).* (*b*) *The activation energy E_a as a function of Fe thickness. Solid circles are data for films prepared with successive deposition, open circles are data for independently prepared films. Solid line is a fit to Eq. 2.56 (the graph is taken from Ref.[37]). Squares symbols are data from current study obtained by fitting Eq. 2.57 and Eq. 2.54 to the susceptibility curves measured while heating at constant rate of 0.05 K/s.*

of heating rate for thickness range studied here. According to the simple model of ac-susceptibility of Eq. 2.54, the increase in the susceptibility FWHM with thickness, again with the exception of data for 1.25 ML film, can be attributed to the decrease in both the phenomenological parameters κ given by Eq. 2.58, and the activation energy E_a given by Eq. 2.56. Smaller κ ($\propto d^{-3/2}$), and $E_a (\propto d^{-3/2})$ result in a smaller rate of decrease of the susceptibility on both sides of the peak, and thus a wider curve. Fitted values of the parameter κ are shown in Fig. 4.10 as a correlation plot with $\ln(A)$ according to Eq 2.59. The values of κ and A are obtained by fitting Eq. 2.57 to the susceptibility at high temperature where $\omega\tau_a \ll 1$.

As will be seen in the following sections, the film with Fe thickness of 1.25 ML departs from other films not only in the thickness dependence of the peak temperature

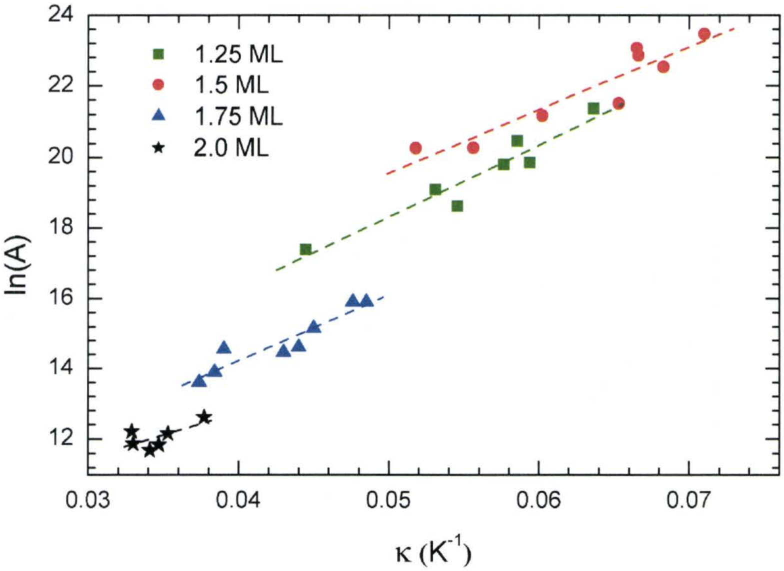

Figure 4.10: *A correlation plot of* $\ln(A)$ *against* κ. *The values of* A *and* κ *are obtained by fitting Eq. 2.57 to the susceptibility at high temperature where* $\omega\tau_a \ll 1$. *Green symbols are for data in Fig. 4.5, and blue symbols are for those shown in Fig. 4.6. The dashed line serves as guide to the eyes.*

and FWHM, but in all aspects. This departure might be linked to the cross-over region with the effective magnetic anisotropy $K_{\text{eff}}(= K_s/d - \Omega)$ in this range of thickness[2]. For thickness $d < 1$ ML, the surface is created and thus K_{eff} increases with thickness as $K_s \sim d$ (*surface is proportional to the thickness in this range*). For thickness $d > 1$ ML the effective anisotropy decreases with thickness as $K_{\text{eff}} \sim 1/d$. This could lead to complex domain phases that make the film of 1.25 ML behave differently.

4.3.2 Relaxation Of The Domain Density

The susceptibility measurements from 1.75 ML Fe/ 2 ML Ni/W(110) film, illustrated in Fig. 4.6, show that below the heating rate R of 0.3 K/s, the trace shifts to lower temperature as the heating rate increases. However, for a heating rate above the rate

---

[2] For more detail about the effective anisotropy, see sections 2.6.3 and 2.7

of 0.3 K/s, the susceptibility trace starts to shift to higher temperature as R increases. As a quantitative measurement of the susceptibility shift with R, Fig. 4.7 shows the dependence of the susceptibility peak temperature (T_p) on the heating rate, R, for the four samples studied here. The results of Fig. 4.7 show that there is a critical heating rate R_c below which the peak temperature T_p decreases with R, and above which T_p increases with R. This critical rate, R_c, depends on the film thickness, and decreases monotonically with increasing thickness. R_c is not observed in the experimental range of R for the 1.25 ML film. Taking together, these results suggest that there are at least *two mechanisms with opposite effects*; the first makes the entire susceptibility trace shift to low temperature as the heating rate increases while the second makes the trace shift in the opposite direction. The relative importance of the two mechanisms depends upon the film thickness.

In section 2.9.1, we have proposed a model that describes the effect of the relaxation process of domain density equilibration on the susceptibility when the constant heating rate is changed. The model predicts different behavior depending on the value of the time constant τ_n ($=\tau_{0n}\exp(E_n/kT)$). This time constant is defined in term of the relaxation time constant, τ_a that describes the activated motion of domain walls between pinning sites in response to an applied magnetic field. The relation was

$$\tau_n(T) = \alpha\tau_{0a}\exp(\frac{E_a}{kT}), \tag{4.6}$$

where $\alpha(=\eta/\xi)$ is the ratio between the average separation between nucleation sites (η), and the Barkhausen steps size (ξ). The experimental results of Fig. 4.5, 4.6, and 4.11 along with Fig. A.1 presented in the appendix, show that the peak amplitude is nearly independent of the heating rate, R. According to Fig. 2.12, this is consistent with the model only in region ①, where the peak temperature depends on R as $B = dT_p/dR \approx -10^0$, or in region ④, where $B \approx +10^1$. The data in Fig. 4.7 are consistent with the latter, as estimate of B taken from the data at large R gives

$B = 8$ (s) for the 1.75 ML film and $B = 13$ (s) for the 2.00 ML film. This suggests that the change in the susceptibility peak temperature due to the domain density equilibration process, will follow the relation:

$$T_p(R) = BR + \text{constant} \tag{4.7}$$

where B is a positive constant that depends on the value of α.

4.3.3 Relaxation Of A Quenched High Temperature Domain Phase

A second mechanism must cause the susceptibility peak temperature to decrease with R at small R. In order to investigate this mechanism further, additional experiments were performed. Figure 4.11(b) shows the real part of the ac susceptibility measured from a 1.5 ML Fe/ 2 ML Ni/W(110) film during cooling at rate of $R = -0.1$ K/s and -0.05 K/s. For the sake of comparison, the susceptibility measured at a series of heating rates[3], from a different sample with the same thickness is presented in Fig. 4.11(a). Although the range of R available for cooling is limited, it is clear that the differences in traces for $R = -0.05$ K/s and -0.10 K/s is very small and are likely negligible. In any case, there is a distinct asymmetry in the behavior of the heating curves with the corresponding cooling curves. The peak position and shape for the cooling curves is most similar to those of the heating curves measured at $R \geq 0.3$ K/s.

For reasons that will be discussed later, the heating curve measured at $R \geq 0.3$ K/s have almost the same full width-at-half-maximum (FWHM), whereas those measured at smaller rates have FWHM that increases as the heating rate decreases. This behavior has been observed for all heating curves measured from the four films with

---

[3] It is the same experiment from which the peak temperature T_p is extracted and plotted as a function of R in Fig. 4.7 for the film of 1.50 ML Fe.

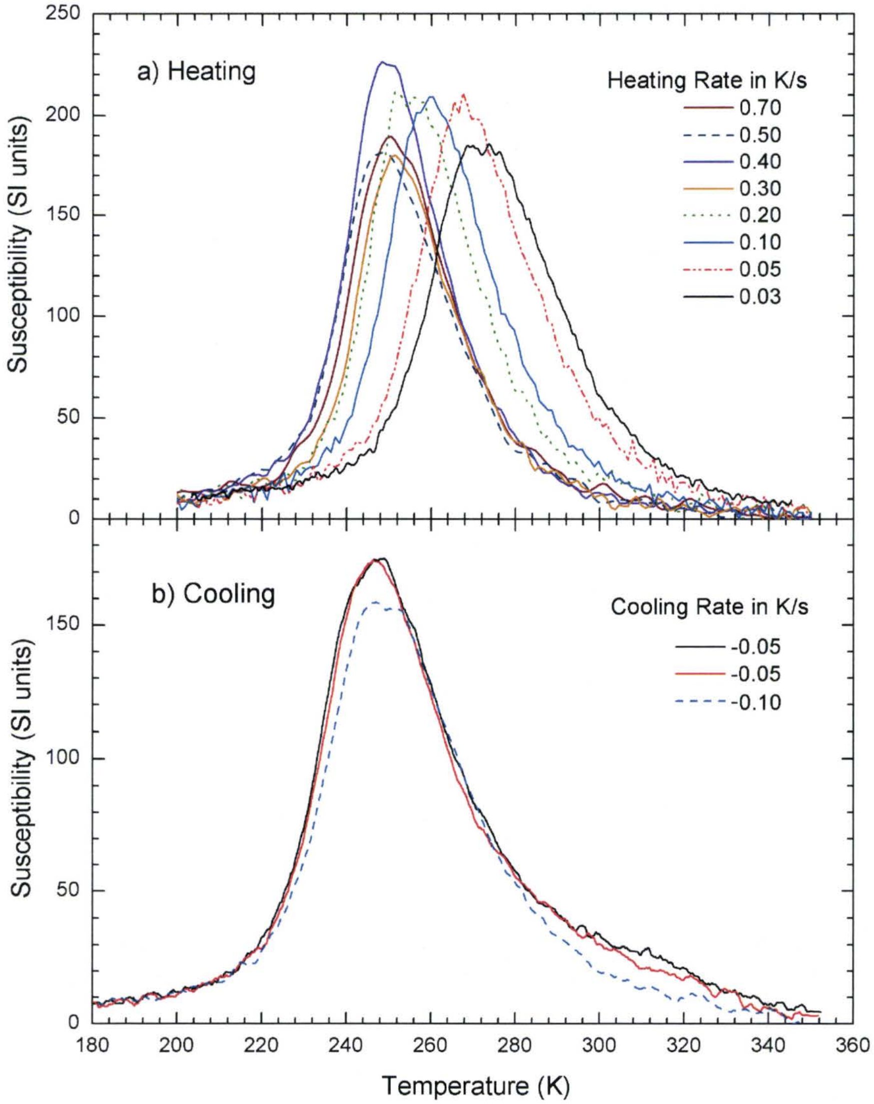

Figure 4.11: *The ac magnetic susceptibility of 1.5 ML Fe/ 2 ML Ni/ W*(110) *film as a function of temperature while changing the temperature at different constant rates R. a) Measurements for heating the film. b) Measurements for cooling the film. There are two traces measured at when R = -0.05 K/s to indicate th degree of repreducibility.*

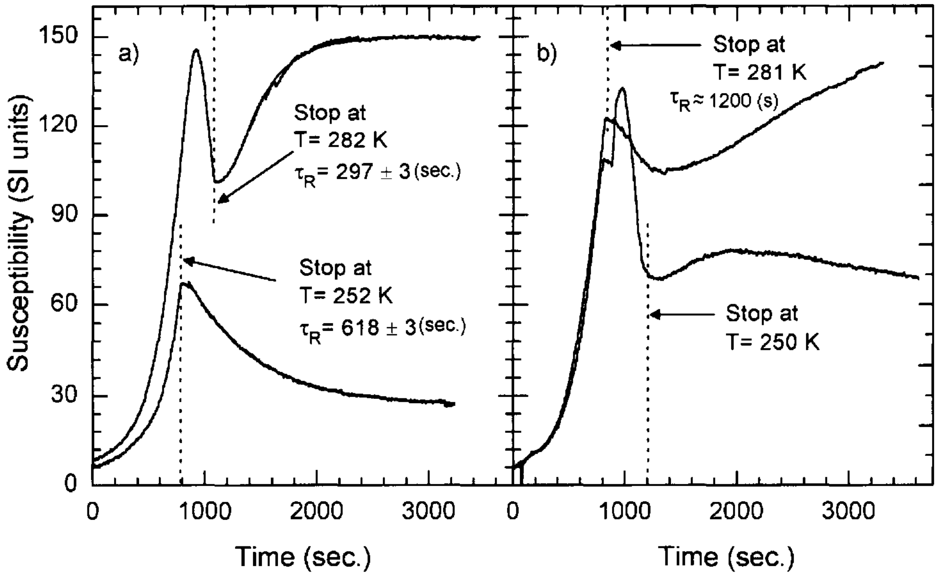

Figure 4.12: *Magnetic susceptibility measurement from 1.5 ML Fe/ 2 ML Ni/* W(110) *film as a function of time. a) The sample temperature is controlled to increase at a constant rate of* $R = 0.1K/s$ *to a specific temperature; below the peak temperature and above the peak temperature. The susceptibility is then monitored as a function of time at those constant temperatures. b) The susceptibility measurement as a function of time at the same temperatures but when reached upon cooling at a rate of* $R = -0.1K/s$. *In the case of heating, the initial state at* $t = 0$ *is reached upon cooling at a constant rate of* $R = -0.1K/s$. *Red solid line represent fitting to the simple exponential decay and growth.*

different thicknesses as seen in Fig. 4.8.

To access even longer time scales, the following experiment on a third sample of 1.5 ML Fe/ 2 ML Ni/ W(110) has been performed: the susceptibility was measured as a function of temperature and time while heating or cooling at constant rate, until a predetermined temperature was reached. At that point, the temperature was held constant and the susceptibility was monitored as a function of time. The results of such an experiment are presented in Fig. 4.12. In Fig. 4.12(a), the measurement was made after heating is stopped at a temperature below and above the peak temperature, whereas in Fig. 4.12(b) shows the results of the corresponding cooling

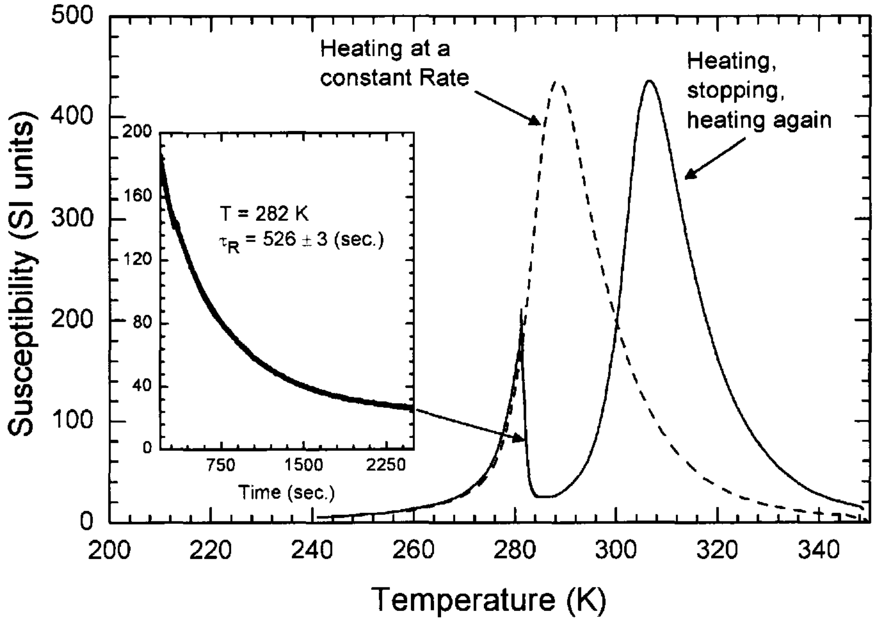

Figure 4.13: *Magnetic susceptibility of a 1.5 ML Fe/ 2 ML Ni/ W*(110) *film as a function of temperature. The dashed curve represents measurement while heating at 0.3 K/s and the solid curve is for the measurement while the temperatures was controlled to change in three stages; heating at R = 0.3 K/s, stopping at 282 K for almost 45 min., and heating again at the rate of R = 0.3 K/s. The inset shows the susceptibility as a function of time at T = 282 K, and the red line represents fitting to a simple exponential decay*

experiment. After heating to 252 K (which is below the peak temperature), the susceptibility relaxes to a lower value by a simple exponential decay with $\tau = 618 \pm 3$ (s). After heating to 282 K (which is above the peak temperature), the susceptibility relaxes to a higher value but with much smaller relaxation time $\tau = 297 \pm 3$ (s). When the same temperatures were reached upon cooling, the relaxation is in the same direction as for heating but proceeds over much longer time scales. Rough estimates of the relaxation times after cooling are $\tau \approx 5000$ (s) at 250 K and $\tau \approx 1200$ (s) at 281 K. These results are entirely consistent with Fig. 4.11(a), and show that the system always relaxes toward curves measured with smaller values of R.

A final experiment on a different sample of 1.5 ML Fe/ 2 ML Ni/ W(110) is presented in Fig. 4.13. In this experiment, two type of measurements are made. The susceptibility was measured as a function of temperature while changing the temperature at constant heating rate of $R = 0.3$ K/s (dashed curve), then the sample is cooled down once more at $R = -0.1$ K/s to the same initial temperature ($\approx$ 240K). In the second measurement, the sample temperature is increased in three stages: the temperature was initially increased at a rate of $R = 0.3$ K/s up to $T = 282$ K, and the relaxation of the susceptibility was monitored as a function of time at this constant temperature as indicated in the inset. When the relaxation was almost complete, the heating at $R = 0.3$ K/s was then resumed. The shift in the curve shows that the system relaxes from a state that produces a susceptibility peak at lower temperature to one with a peak at higher temperature. The experiment also indicates that the amount that the susceptibility curve shifts does not depend on the heating rate itself, but rather on the total time that has been elapsed during heating.

The results presented in Fig. 4.11 - Fig. 4.13, taken together with the recent numerical studies [24, 26, 27] suggest a slow relaxation from "a nonequilibrium" delocalized state to an ordered stripe phase, as was introduced in section 2.9.2. Starting at high temperature the sample is in one of the delocalized domain states in which the domains may not be aligned along a single axis, and have a high density of dislocations in their structure. Upon cooling, the system enters the temperature range where the equilibrium phase is the ordered stripe phase. The system responds on two different time scales. On a long time scale, the system relaxes from the delocalized state to the stable ordered stripe state as in Fig. 4.12(b). This relaxation is very slow, presumably because it is difficult for the relatively small dipole energies to reorient the domain segments to a common axis and/or to annihilate the topological defects in the domain structure [24, 26, 27]. Another way to see this is the negligible difference between the cooling traces at the rate of -0.1 K/s and -0.05 K/s in Fig. 4.11(b). On other hand, the system adjusts its average domain density with temperature. Analysis in the previous section suggests that the time scale of this process is much shorter than the time scale of the domain phase transformation.

The very slow relaxation in domain phase transition during cooling suggests that when the system is quenched to low temperature, it is in a quenched high temperature, delocalized phase. Upon heating, the relaxation from this state to the ordered stripe phase proceeds much more quickly as can be seen in Fig. 4.12(a), although still with a time constant on order of hundreds of seconds. The asymmetry in the relaxation time constant for cooling and heating may explained as follows. When cooling, domains are annihilated from the delocalized phase, by breaking up existing domains. In this way, more dislocations in the the domain structure are created. This works against the establishment of the ordered stripe phase, and makes the relaxation very slow. When heating, domains are being created. They can be created directly in the ordered stripe phase, since it has lower energy. The created ordered stripe phase then grows (coarsens) and displaces the quenched high temperature, delocalized phase. A schematic graph illustrates this process is shown in Fig. 4.14. This scenario for the creation of ordered stripe phase is similar to the recent simulation by Cannas *et al.* [26, 27]. Their simulation shows that this can occur in two ways. When the system is quenched to a low temperature T' far below the phase transition temperature T_O, the ordered stripe phase slowly coarsens in a background of the Ising nematic phase. When T' is not far below T_O, the system relaxes to the stable ordered stripe phase through a sudden nucleation and coarsening of stripe domains in a background of a strongly metastable Ising nematic phase. In both cases there is a coexistance of the two phases; the ordered stripe and the delocalized phases.

Another scenario of the establishment of the ordered stripe phase is possible. The quenched high temperature delocalized state has a high density of topological defects. It is then possible that the relaxation from the quenched high temperature, delocalized

Figure 4.14: *A schematic graph illustrate the growth of the ordered stripe phase in a background of the quenched high temperature, delocalized phase. The enclosed area by dotted curve represents the area that is swept by the advancement of the complex domain interface between ordered stripe and delocalized phases.*

state to the ordered state proceeds via the reduction in a more homogeneous density of defects as the domains grow and merge together upon heating.

For reasons that will be discussed later, the susceptibility of the quenched high temperature delocalized phase and that of the stable ordered stripe phase are distinguished by a shift in a temperature. As the system is taken to high enough temperature, the delocalized state becomes the equilibrium state once more. The strong thermal fluctuations do not allow the ordered stripe phase to exists as a metastable phase, as the system moves quickly to the delocalized phase [26, 27]. Therefore the sequence repeats upon cooling once again.

To test this interpretation, the relaxation process of the domain phase transformation upon heating is modeled as an activated process with time constant τ_R that follows an Arrhenius law:

$$\tau_R(T) = \tau_{0R} \exp(\frac{E_R}{kT}), \tag{4.8}$$

where E_R, according to the first scenario, is an activation energy associated with the advancement of a complex domain interface between ordered stripe and delocalized phases (see Fig.4.14). According to the second scenario of a continuous transition, E_R represents the kinetic energy barrier to creating the ordered stripe phase. Figure 4.13 shows that the relaxation depends upon the elapsed time, not directly on the heating rate R. The total number of time constants (t_{eff}), that have elapsed while heating from the initial temperature T_i up to the peak temperature T_p, can be defined as:

$$t_{\text{eff}}(R) = \int_0^{t_p(R)} \frac{dt}{\tau_R} = \int_{T_i}^{T_p(R)} \frac{dT}{R\tau_R(T)}. \tag{4.9}$$

Using the susceptibility peak temperature as a marker for the relaxation suggests

$$T_p(R) = T_0 - \Delta \exp(-t_{\text{eff}}(R)), \tag{4.10}$$

where T_0 is the peak temperature when the relaxation to the ordered stripe state is complete, and Δ is a constant giving the total peak shift between a pure quenched high temperature, delocalized phase and a pure equilibrium ordered stripe phase.

In the previous section, we discussed the change in the peak temperature with R due to the relaxation process of domain density. This effect is small in the data from the film of 1.5 ML Fe in Fig. 4.7. Therefore, an approximation can be made by assuming only the relaxation process of domain phase transformation of Eq. 4.10 that causes the change in peak temperature for this film.

According to Eq. 4.10, a plot of $\ln(T_0 - T_p)$ vs t_{eff} has a slope of -1, and intercept of $\ln\Delta$. There are three adjustable parameters in this description, τ_{0R}, E_R, and T_0. For a given choice of τ_{0R}, E_R and T_0 are linked by the requirement that the slope is -1. Using this constraint, the least squares fit to the experimental peak temperature determines a value of E_R, T_0, and Δ. As shown in Fig. 4.15(c), the residuals of the least squares fit depends on the order of magnitude of τ_{0R}, placing a lower limit of $\tau_{0R} \approx 10^0$, but is insensitive to larger values.

The two experimental relaxation times in Fig. 4.12(a), coupled with Eq. 4.8 allow an independent estimate of $\tau_{0R} = 0.7$ s, and $E_R = 1735$ K. This value of τ_{0R} is

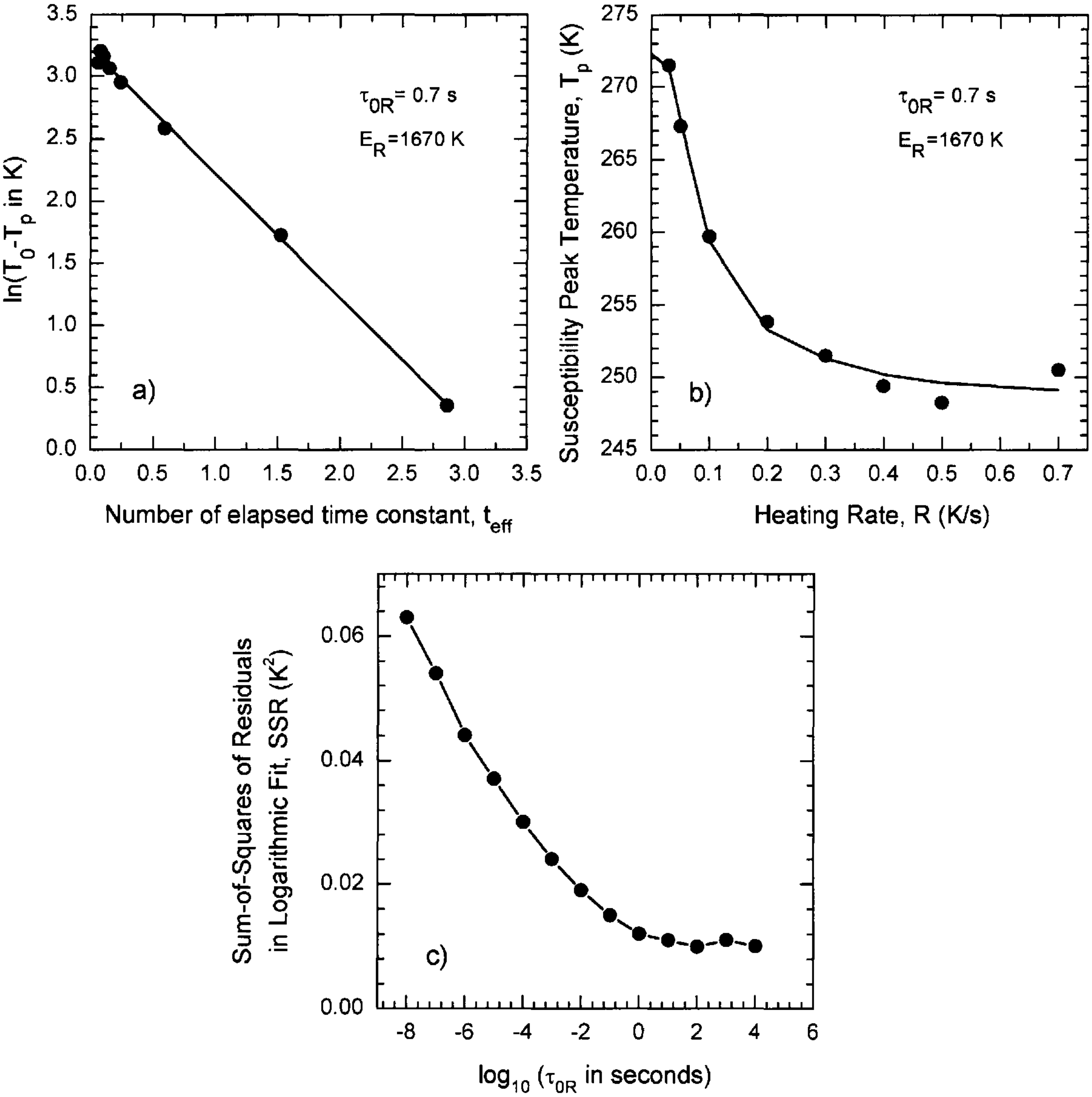

Figure 4.15: *Fit of the relaxation of the susceptibility peak temperature to Eq. 4.10. a) Peak temperatures plotted against* t_{eff} *as defined in Eq. 4.9, assuming* $\tau_{0R} = 0.7$ *s.* $E_R = 1670$ *K is the fitted value of the activation energy for the phase transformation. b) The same fit as in a), plotted against the heating rate, R. c) The sum-of-square residuals (SSR) of the logarithmic fit as a function of* $\log_{10}(\tau_{0R})$

entirely consistent with the fitting, and was used for the plot in Fig. 4.15(b) to give $T_0 = 272.27$ K, $\Delta = 24.79$ K, and a value of $E_R = 1670$ K. This fitted value of E_R is in very reasonable agreement with the experimental estimate. At first glance, one might think that the value of τ_{0R} is too large. However, it is reasonable when it is interpreted as an attempt frequency of about 1 Hz for a macroscopic domain rearrangement that occurs through a correlated action of many microscopic Barkhausen areas, each of which has an attempt frequency of the order of 10^9 Hz.

The numerical studies by Cannas and co-worker [26, 27] predict a coexistence of delocalized and ordered stripe phases as the system relaxes toward the equilibrium ordered stripe phase. Our results do not support this scenario, for the following reason. According to our model, the susceptibility measured at $R = 0.7$ K/s represents a state that is only 7% relaxed from the initial high temperature delocalized state, whereas, the susceptibility measured at $R = 0.03$ K/s represents a state that is 97% relaxed to the low temperature ordered stripe state. The peak of the susceptibility of these two states is separated by 20 K. Therefore, if there is a mixed state of both delocalized and ordered stripe domains, then the susceptibility measured at intermediate value of R would exhibit a double-peaked structure, which is not observed in this study. The progressive shift in the susceptibility peak temperature with R could be rather related to the relaxation of a distributed property, such as nonequilibrium density of domain dislocations and/or domain wall curvature that are characterstice of high temperature state from which the quench occurred.

To conclude this section, we would like to emphasize that the decrease in the peak temperature of the susceptibility at small R is incompatible with a relaxation of domain density within a single domain phase. They are compatible with a phase change with slow dynamics from high temperature delocalized phase to the low temperature ordered stripe phase. These dynamical measurements of the domain phase transformation are in essential agreement with simulations of Bromley *et. al* [24] and of Cannas *et. al* [26, 27] who found a very long time scale for the establishment of the stripe ordering of domains.

4.3.4 Competition Between The Two Relaxation Mechanisms

The changes of the susceptibility peak temperature with heating rate (R) in Fig. 4.7 suggests that two mechanisms are involved; one which dominates at large R, and another that dominates at small R. These have been identified as an activated change in the domain density, as discussed in section 4.3.2, and a relaxation from a quenched delocalized state, as discussed in section 4.3.3. The first process has been described by Eq. 4.7, while the other has been modeled by Eq. 4.10. Combining these two equations to account for both mechanisms, gives

$$T_p(R) = T_0 - \Delta \exp(-t_{\text{eff}}(R)) + BR. \tag{4.11}$$

For a given choice of $\log_{10}(\tau_{0R})$, the least squares fit to the experimental peak temperature in Fig. 4.7 determines a value of E_R, T_0, Δ, and B. In Fig. 4.16 the sum-of-square residuals (SSR) of the least square fit is plotted as a function of $\log_{10}(\tau_{0R})$ for two films of 1.50 ML and 1.75 ML Fe [4]. The fit gives a value of 10^0 s for τ_{0R} for all films except the film of 1.25 ML Fe, where $\tau_{0R} = 10^{-1}$ s. Figure 4.17 shows the peak temperature T_p as a function of the heating rate R for the four films, along with the fitted curves produced according to Eq. 4.11 using the best-fit parameters summarized in Table 4.1. The error of each parameter was determined by varying it while all other were held constant, to find where the square of residuals increased by 1. Sample graphs showing the error calculation of each parameter are shown in the appendix.

The film of 1.25 ML Fe is different as has been discussed in in section 4.3.1. It has a large negative value of B which is not supported by the model, and a time constant

---

[4] SSR vs $\log_{10}(\tau_{0R})$ for films with 1.25 and 2.00 ML Fe have different y-scale and thus it better to be presented in a separate graph. This graph is presented in the appendix

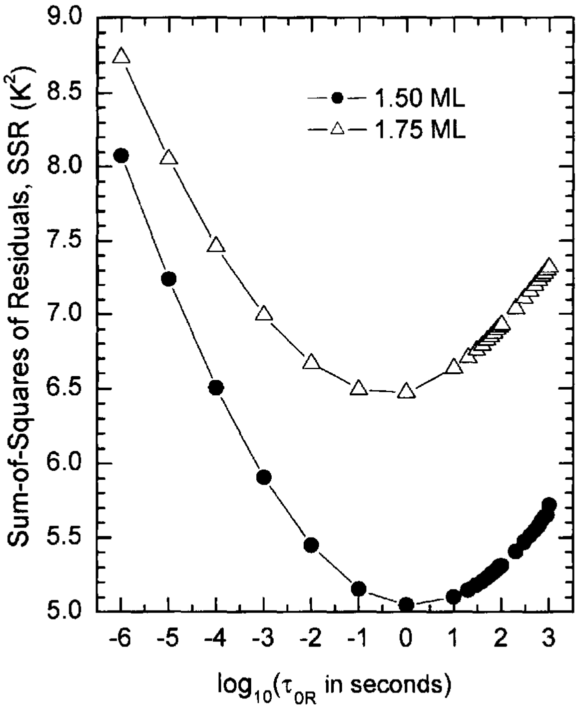

Figure 4.16: *The sum-of-squares residuals (SSR) as a function of* $\log_{10}(\tau_{0R})$ *shows a best-fit value of* $\tau_{0R} = 1.0$ s *for the films with Fe thickness of 1.50 ML and 1.75 ML.*

$\tau_{0R} = 10^{-1}$ s, one order of magnitude smaller than others. This shows that there is no convincing evidence that two mechanisms are needed for this film. However, when the term $T_p(R) \sim BR$ is excluded (i.e, assuming $B = 0$), the fitting gives a reasonable value of $\tau_{0R} = 10^0$ s, but with other parameters that are not consistent with those of other films. Together, this might be due to a complicated domain phase that is associated with the cross-over region in the effective anisotropy K_{eff}. In the following sections, no further discussion will be made about this film.

For the film of 1.50 ML Fe, the fitting gives a small value of $B = 2.67 \pm 1.8$ s that is consistent with the analysis made in section 4.3.3 where the term $T_p(R) \sim BR$ was not considered. This value of B is associated with a value of $\tau_{0R} = 10^0$ s, that is entirely consistent with the experimentally calculated value of 0.7 s. Hence, the finding of section 4.3.3 is confirmed and refined.

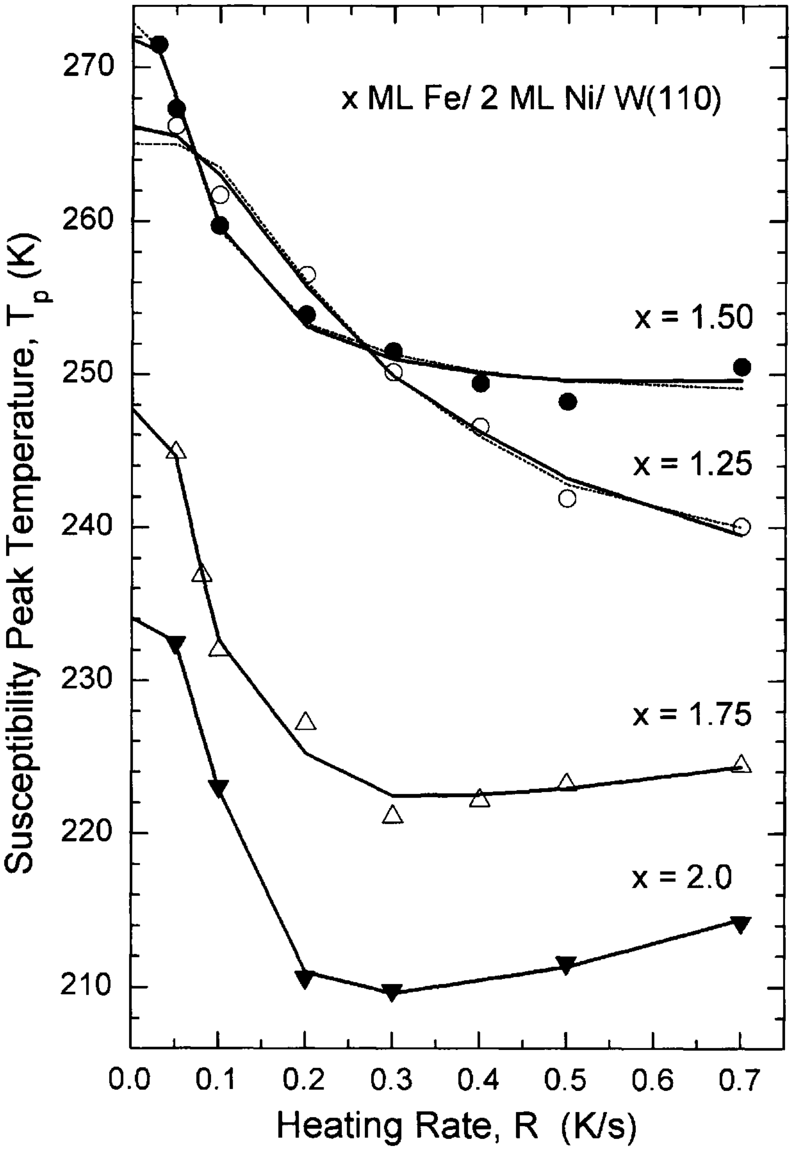

Figure 4.17: *Least square fitting of the susceptibility peak temperature to the relaxation model of Eq. 4.11 (solid lines) and Eq. 4.10 (dotted lines).*

Table 4.1: *Best-fit parameters for the data shown in Fig. 4.17 according to Eq. 4.11. For a comparison, the best-fit parameters according to Eq. 4.10 are listed for the films with Fe thickness of 1.25 ML and 1.50 ML.*

Fe thickness, d (ML)	$\log_{10}(\tau_{0R})$ (s)	E_R (K)	T_0 (K)	Δ (K)	B (sec.)
1.25	-1.00±0.03	1860±15	266.15±0.5	21.78±0.5	-11.33 ±1.0
	0.00±0.02	1230±10	265.05±0.5	31.68±0.5	assumed = 0
1.50	0.00±0.02	1560±15	271.82±0.6	26.04±0.5	02.67 ±1.2
	$\log_{10}(0.7)$	1670±15	272.27±0.5	24.79±0.5	assumed = 0
1.75	0.00±0.02	1390±10	247.74±0.5	33.75±0.4	10.95 ±1.0
2.00	0.00±0.01	1270±08	234.07±0.5	38.05±0.3	20.96 ±1.0

The large positive value of B for the films with thickness of 1.75 ML and 2.00 ML show the need of considering the two mechanism. These fitted value are consistent with order of magnitude predicted in section 4.3.2.

The next two sections analyse the quantitative interpretation of the finding of this section for the films of thicknesses $d > 1.25$ ML.

4.3.5 Quantitative Analysis of Relaxation of The Domain Density

The fitting results of the previous section make it clear that including a term $T_p(R) \sim BR$ is consistent, and even necessary to properly describe the data. It is not yet obvious that this term must represent the effect of relaxation of the domain density, as outlined in section 2.9.1. For that purpose, a quantitative comparison of the fitted value of B and those predicted by the model of domain density relaxation is required.

Since the effects of this process are seen at large R, where the system is in the quenched high temperature, delocalized phase, it would be best to use as input for the calculation of $\chi(T)$, parameters describing this phase as $R \longrightarrow 0$. This is not possible because the data at small R are dominated instead by the relaxation to the ordered stripe phase. Instead, a compromise solution is to use $\chi_c(T)$ measured at $R = R_c$. The choice of R_c is made so that it is large compare to the time scale of the relaxation process of the phase transformation and at the same time is small compare to the time scale of the relaxation process of the domain density equilibration. An estimation of the required parameters can then be made by fitting the data of $\chi_c(T)$ to the simple model of the ac susceptibility given by Eq. 2.54 and Eq. 2.57, or

$$\chi(T) = \frac{A\exp(-\kappa T)}{1+\omega^2\tau_a^2(T)}. \tag{4.12}$$

In section 2.9.1, it has been argued that the energy barrier, E_n involved in the domain wall growth and/or shrinkage mechanism is the same as the energy barrier, E_a involved in the domain wall motion between pinning sites in response to an applied magnetic field. Also, it is shown that the time constant τ_{0n} is linearly related to the time constant τ_{0a} with a factor of proportionality $\alpha(=\eta/\xi)$, where η is the average distance between nucleation sites and ξ is the size of the Barkhausen step. Therefore fitting Eq. 4.12 to the susceptibility curve χ_c, leaves only one free parameter, α. Figure 4.18 shows the fits to Eq. 4.12 used to establish the fitted parameters used for each thickness in Table 4.2. Fitting procedures are discussed in details in Ref. [37, 38], and briefly outlined in next section

When heating at a rate $R > R_c$ the effect of the relaxation of the domain density becomes more important. Thus, it is more accurate to describe the measured susceptibility at $R > R_c$ via the Eq. 2.69, or

$$\chi(T) = \frac{\chi^{\text{eff}}(T)}{1+\omega^2\tau_a^2(T)}, \tag{4.13}$$

where $\chi^{\text{eff}}(T)(\sim 1/n(T))$ is the solution of Eq. 2.64 that describes the relaxation process in domain density:

$$\frac{\partial n(T)}{\partial T} = -\frac{1}{R\alpha\tau_a(T)}\left(n(T) - n^{\text{eq}}(T)\right). \tag{4.14}$$

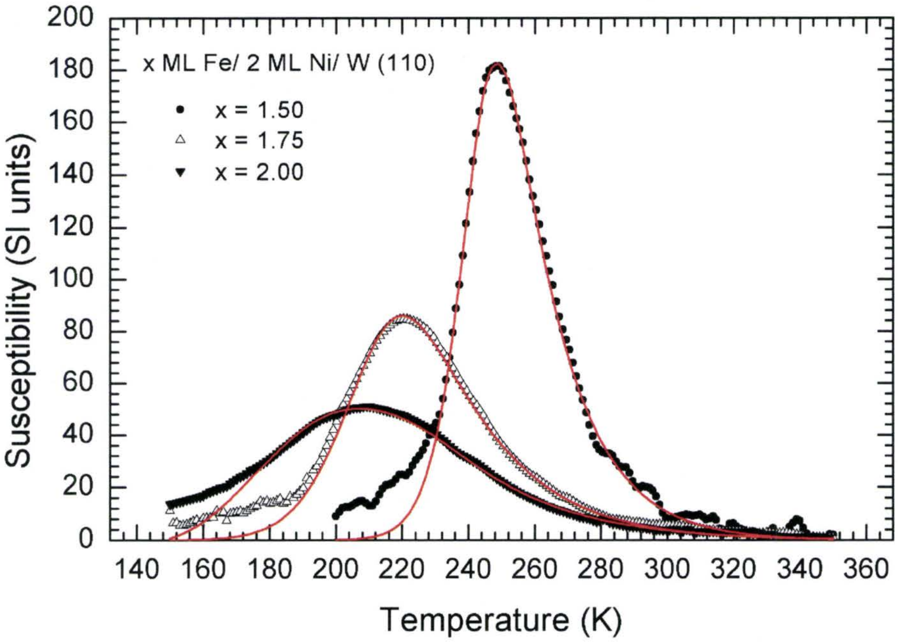

Figure 4.18: *The real part of the ac magnetic susceptibility of x Fe/ 2 ML Ni/W(110) of thicknesses x=1.50, 1.75, and 2.00 ML, measured at heating rate $R = R_c$ = 0.5, 0.3, and 0.3 (K/s) respectively. Solid lines results from fitting Eq. 4.12 to the data.*

As seen in section 2.9.1, the susceptibility peak temperature changes linearly with the heating rate R with a slope B that depends on the value of α. The relative change in peak height with R also depends on the value of α. Figure 4.19 plots both these parameters as a function of $\log_{10}(\alpha)$. Only the curves that are produced when $\alpha \approx 10^{5.5}$ are consistent with the experimental curves since they give a peak height variation of $\approx$ 10%, and a change in peak temperature that increases as R increase (i.e, $B > 0$). Using this single value of α, one can calculate the time constant τ_{0n} from the relation $\tau_{0n} = \alpha\tau_{0a}$, and find the slope B from Fig. 4.19. In table 4.2, we list the value of τ_{0n} and B. The calculated value of B should be compared to those fitted empirically in Table. 4.1.

The value of B calculated according to the model of the domain density relaxation process is within 10%-20% of the fitted value, despite approximations on finding

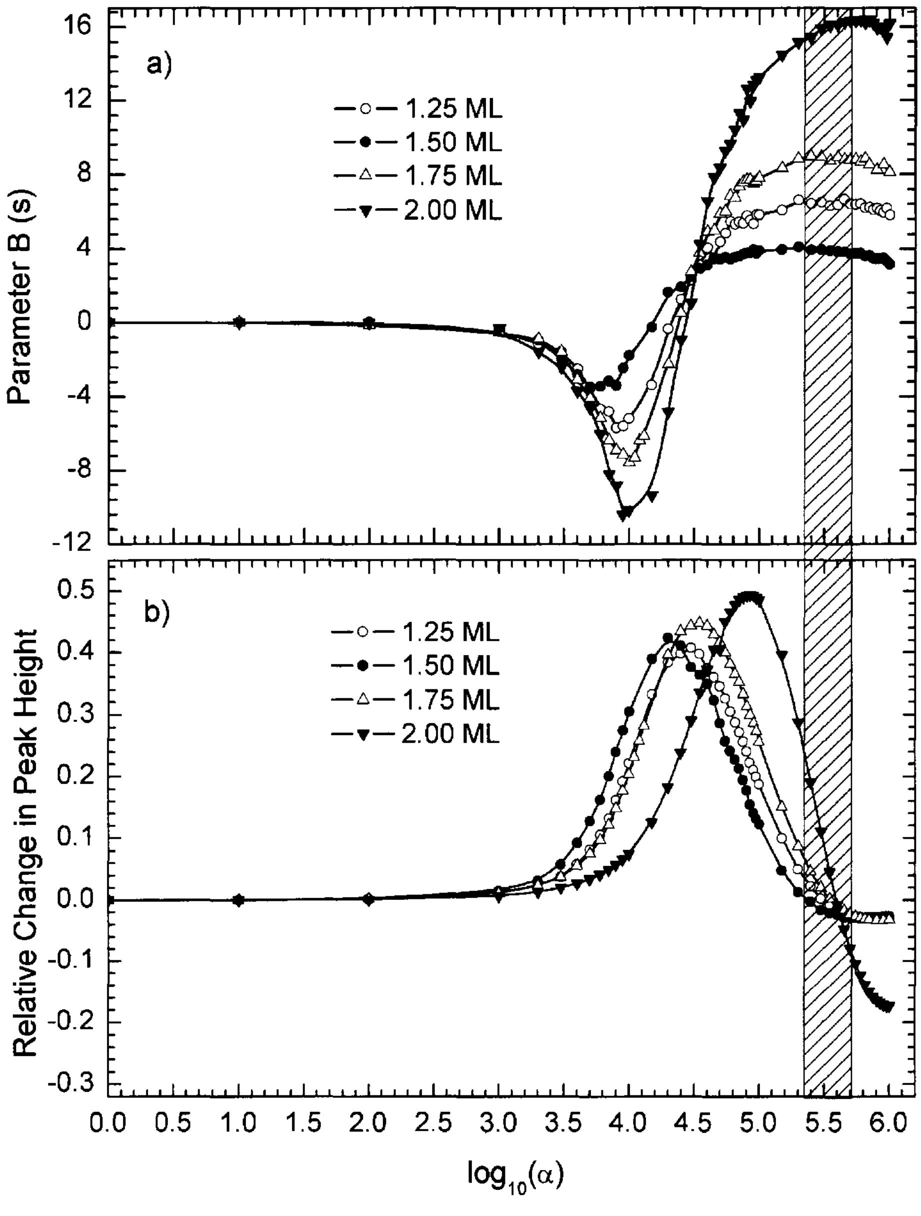

Figure 4.19: *a) The rate of change in the susceptibility peak temperature with heating rate* R $(B = dT_p/dR)$ *and b) the relative change in peak heights with* R *as a function of* $\log_{10}(\alpha)$*, where* $\alpha = \tau_{0n}/\tau_{0a}$.

Table 4.2: *Calculated relaxation time* τ_{0n} *and* B*, according to the relaxation of the domain density, along with those parameters describing* χ_c *and used in the calculation.*

Fe thickness, d (ML)	τ_{0a} (sec.)	$E_n = E_a$ (K)	κ (K^{-1})	Calculated B (sec.)	$\tau_{0n} = \alpha\tau_{0a}$
1.50	1.18×10^{-15}	6694	0.069	3.95 ±0.5	3.73×10^{-10}
1.75	2.57×10^{-09}	2725	0.044	8.91 ±0.5	8.12×10^{-04}
2.00	1.36×10^{-06}	1320	0.032	16.06 ±0.5	4.30×10^{-01}

parameters at R_c. Another way to see this consistency is by the comparison between the relative ratio of calculated and fitted values of B. Table 4.3 lists these ratios with respect to the value for the 2 ML film. The ratios show a consistent scaling.

The very good consistency between the empirical fitted values of B and those calculated based on the relaxation model of the domain density, in sec. 2.9.1, provides strong evidence that the activated change in domain density is the cause of the increase in the susceptibility peak temperature at large R. This process proceeds over a time scale that is set by the rate of change in temperature, R. The analysis in this section reveals a single value of $\alpha = 10^{5.5}$. This confirms the assumption of this model, that this is due to domain wall movement during density changing . However, using a single value of α gives a wide range of τ_{0n} related to a wide range of τ_{0a}. This makes it difficult to interpret τ_{0a}^{-1} as a fundamental "attempt frequency" for a Barkhausen step. Order of magnitude changes in τ_{0a} for small changes in film thickness are not consistent with this. Therefore, τ_{0a} seems to be more an adjustable parameter that sets the temperature range of the susceptibility peak temperature T_p via the relation $\omega\tau_a = 1$ [37]. However, since $\alpha \approx 10^{5.5}$ confirms that the time scale for the change in domain density is much shorter than that of the relaxation of domain phase transformation.

From α, one can also get an estimate value of the characteristic length $\eta (= \alpha\xi)$.

Table 4.3: *Relative B ratios with respect to the value for the 2 ML Fe film.*

Fe thickness, d (ML)	Calculated	Fitted
2.00	1.00	1.00
1.75	0.55	0.52±0.11
1.50	0.25	0.13±0.10

Previous studies [37] on the same system provided an estimate of the Barkhausen step $\xi = 580 \pm 90$Å. This gives an estimate value of $\eta = 18.3$ mm, which is orders of magnitude too large to represent the average separation of nucleation sites. The source of this discrepancy is not obvious.

4.3.6 Characterization Of The Quenched High Temperature, Delocalized State.

In the following we intend to characterize the quenched high temperature, delocalized state and the ordered stripe state. To do so, only data of 1.5 ML film are analyzed since the effect of the domain density relaxation process is small (small B) and can be ignored for the present purpose. Accordingly, the susceptibility can be described by the simple model of Eq. 4.12. At high temperature, domain walls are freely moving in response to the applied magnetic field and the susceptibility at the high temperature range is described according to $\chi = A\exp(-\kappa T)$ [35–38]. At low temperature, the walls are more likely pinned and their motion is thermally activated with activation energy E_a. The parameter κ was originally defined in the content of the ordered stripe phase, as in section 2.8, to characterize the induced changes in domain wall spacing upon the application of a magnetic field perpendicular to the film surface. Empirically, it can be extracted from the linear fit of the high temperature tail of the susceptibility when plotted on semilogarithmic scale against temperature T. Figure 4.20(b) shows the fitted value of κ against the heating rate, R. The activation energy of the pinning sites can be extracted by linear fitting of the data at low temperature from $\ln(A\exp(-\kappa T)/\chi(T) - 1)$ vs. $1/T$ plot.

The fitted value of E_a, as shown in Fig. 4.20(b), does not follow a clear trend but rather fluctuates around the average value of approximately 6270 (K). This is consistent with the fact that the pinning of the domain walls is expected not to vary with the heating rate since it is a property of the film and the defects in the film structure [37, 38].

On the other hand, the parameter κ shows a clear trend with the heating rate. Roughly speaking it initially increases rapidly before reaching a plateau region when $R > 0.2$ K/s. Comparing Fig. 4.20(a) to Fig. 4.7 and Fig. 4.8, there is a clear correlation between κ and the susceptibility peak position and width. It is clear that κ changes in moving from the ordered stripe phase (small κ) to the quenched delocalized phase (large κ). This change in κ shifts the peak temperature and reduces the FWHM, and allows the phase transformation to be followed via the measurement of the susceptibility.

The following is a speculative explanation of the finding that the quenched delocalized phase has larger κ than of the ordered stripe phase. The application of an oscillating magnetic field causes the domain walls to move and thus the domain width to vary, creating a net magnetization and a measurable susceptibility. At a given temperature, the phenomenological parameter κ measures the domain walls response to an applied magnetic field. Thus, it is related to the domain stiffness. Larger κ means smaller susceptibility, which this in turns means domains are magnetically stiffer. The delocalized state has a high density of dislocations in the domain structure and might have many regions of different orientations of domain segments. When this phase is quenched at low temperature where the ordered stripe phase is the stable

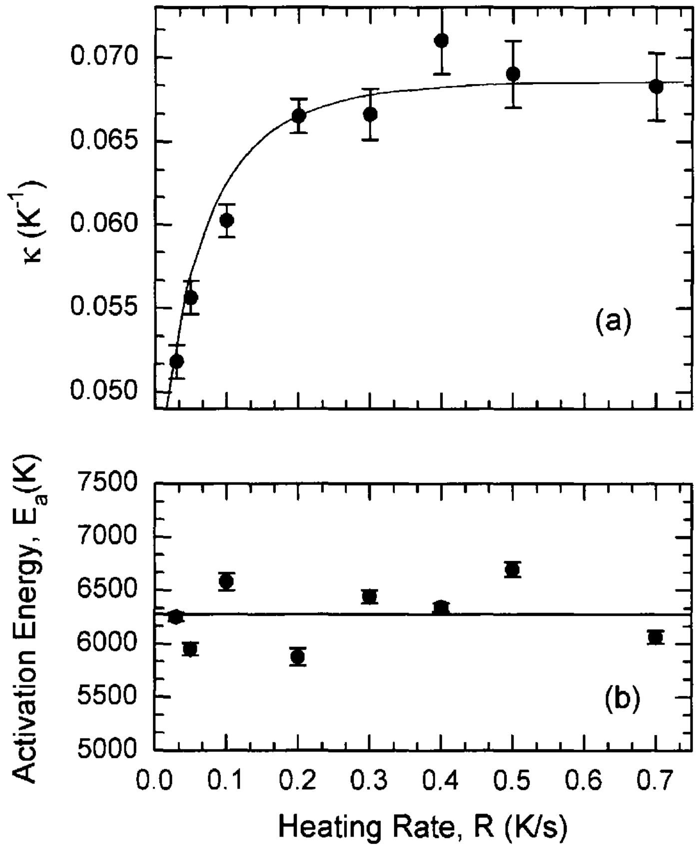

Figure 4.20: *The fitted values of* a) *the stiffness constant* κ *and* b) *the activation energy* E_a *extracted by fitting Eq. 4.12 to the suscpetibility curves of 1.5 ML Fe/ 2 ML Ni/W(110). The solid line is a guide for the eyes*

state, the presented topological defects will hinder the expansion and contraction of neighboring domains. These additional interactions will significantly raise the elastic energy compared to that of stable ordered stripe phase. This makes the quenched delocalized phase stiffer, and gives a smaller susceptibility even if the average domain density is similar in both phases. These consideration are consistent with the experimental finding and could explain why the peak of the susceptibility of the quenched delocalized state is shifted to lower temperature.

Chapter 5

Summary and Concluding Remarks

In this work, the relaxation processes in perpendicularly-magnetized ultrathin Fe/ 2 ML Ni/ W(110) films have been experimentally investigated using the ac magnetic susceptibility. Earlier studies [37–39] provided a quantitative description of local domain wall pinning mechanism in these films. This study aimed to investigate relaxation mechanisms that proceed over a much longer time scale. Different time scales for relaxation have been accessed by altering the constant rate of temperature variation, R, as the susceptibility was measured. The main result of this work is the recognition and quantification of two relaxation mechanisms; the first which dominates at small R but does not depend on R itself, while the other dominates at large R and directly depends on R. The relative importance of the two mechanisms was found to depend upon film thickness.

When quenching the film from high temperature where one of the delocalized domain states is the equilibrium state, to a temperature where the ordered stripe domain state is the equilibrium, there is a clear evidence that the system is trapped in a nonequilibrium delocalized state. This was indicated by the observation of an extremely slow relaxation ($\tau_{0R} \sim 0.3 - 1.4$ hours) in the susceptibility when the cooling was stopped and monitored at constant temperature, and from the negligible difference between susceptibility traces at a cooling rate of -0.1 K/s and -0.05 (K/s) measured from the film of 1.5 ML Fe. Upon heating, the magnetic susceptibility curve changes shape and peak position as a function of time, with a time scale on the order of hours. The peak position relaxes according to activated dynamics with a fundamental time constant $\tau_{0R} \approx 1$ s and activation energy $E_R \sim 1200 - 1600$ (K) depending upon film thickness. The fundamental time scale $\tau_{0R} \gg \tau_{0a} \sim 10^{-9}$ (s) suggests mesoscopic rearrangement of the domains that involves the co-ordinated action of many local microscopic Barkhausen steps. The relaxation is accompanied by the reduction in the magnetic domain stiffness of the domain system, as realized by the change in the parameter κ in $\chi(T) \sim Ae^{-\kappa T}$. Together, these results are consistent with the relaxation and removal of a significant density of domain pattern defects and dislocations that have been trapped by quenching. These dynamical measurements of domain transformation are in essential agreement with the numerical studies [24, 26, 27], where a very long time scale for the stripe ordering of domains by the removal of defects is found.

The second relaxation mechanism has an intermediate time scale. The susceptibility peak temperature increases as R increases. This is essentially because during heating, the domain density lags the equilibrium domain density because of activated dynamics for domain growth and/or shrinkage. The activation energy, E_n of this process is found to be the same as the activation energy, E_a of the domain wall pinning process. The relaxation time constant τ_{0n} is linearly related to the relaxation time constant, τ_{0a} as $\tau_{0n} = \alpha\tau_{0n}$, where the proportionality factor α is related to the average separation of domain nucleation sites. Our results provide a single value of $\alpha \approx 10^{5.5}$. The effect of domain density relaxation process was described by the positive rate (B) of change in peak temperature with the heating rate. Our analysis show that B increases monotonically with the film thickness, d, following the decrease in the activation energy E_n from 6694 K for $d = 1.5$ ML to 1320 K for $d = 2.00$ ML.

In this study, the behaviour of the film of 1.25 ML Fe is found to depart from other films in all aspects. This may be because this thickness falls in a range where the effective anisotropy changes from a dependence on d to a dependence on $1/d$. We have not attempted a quantitative analysis of this transition, which remains an interesting subject for future work. Such work can be carried out by extending the experiments of this study to samples with thickness in submonolayer regime, and look at the possible effect due to the percolation process between islands.

Another possible extension of this work can include experiments to find the phase transtion temperature T_O, below which the ground state is the ordered stripe phase, and above which the delocalized phase is the ground phase. In a recent numerical study by Bromley [24], the relaxation from magnetically saturated state to the equilibrium delocalized state is found to proceed over a short time scale by rapid decay of the magnetization. In contrast, when the equilibrium state is the ordered stripe state, the relaxation was found to proceed over three distinct time scales. One of these is a very long time scale that is associate with the removal of the topological defects in the domain structure. In this study, we have found that the measurement of the magnetic susceptibility is sensitive to relaxation dynamics on a number of time scales. Taken these findings together, one may investigate the thickness-dependence of the phase transition temperature, T_O. One possible experiment can be done by monitoring the relaxation of the ac susceptibility at different constant temperatures, after the removal of applied DC magnetic field that drives the system to a saturated state.

Finally, the findings of this thesis have been published and/or submitted to the journal Physical Review B. A first paper [89] is concerned with the very slow relaxation process of a quenched high temperature delocalized phase to the low temperature ordered stipe phase (section 4.3.3). Data included in this paper are only those measured from the 1.5 ML film since the effect of the second relaxation process of the domain density is negligible in this film. In the second paper [90], we include the second relaxation mechanisim of the domain density by extending the analysis of the first paper to the thicker films with Fe thickness of 1.75 ML and 2.00 ML (sections 4.3.2 and 4.3.5).

Appendix A

Additional Figures

This appendix contains the following figures

Figure A.1 shows the complex ac magnetic susceptibility measured from 2.0 ML Fe/ 2.0 ML Ni/ W(110) film.

Figure A.2 shows the imaginary part of the susceptibility measured from the films of Fe thickness of 1.75 ML and 1.50 ML. The real part are shown in main body of the text.

Figure A.3 shows the sum-of-squares residuals from the fitting of the susceptibility peak temperature of the 1.25 ML and 1.75 ML Fe films, according to Eq. 4.11.

Figure A.4 and **Fig. A.5** show sample graphs illustrating the error calculation in the best-fit parameters describing the change in the peak temperature of Fig. 4.17 according to Eq. 4.11..

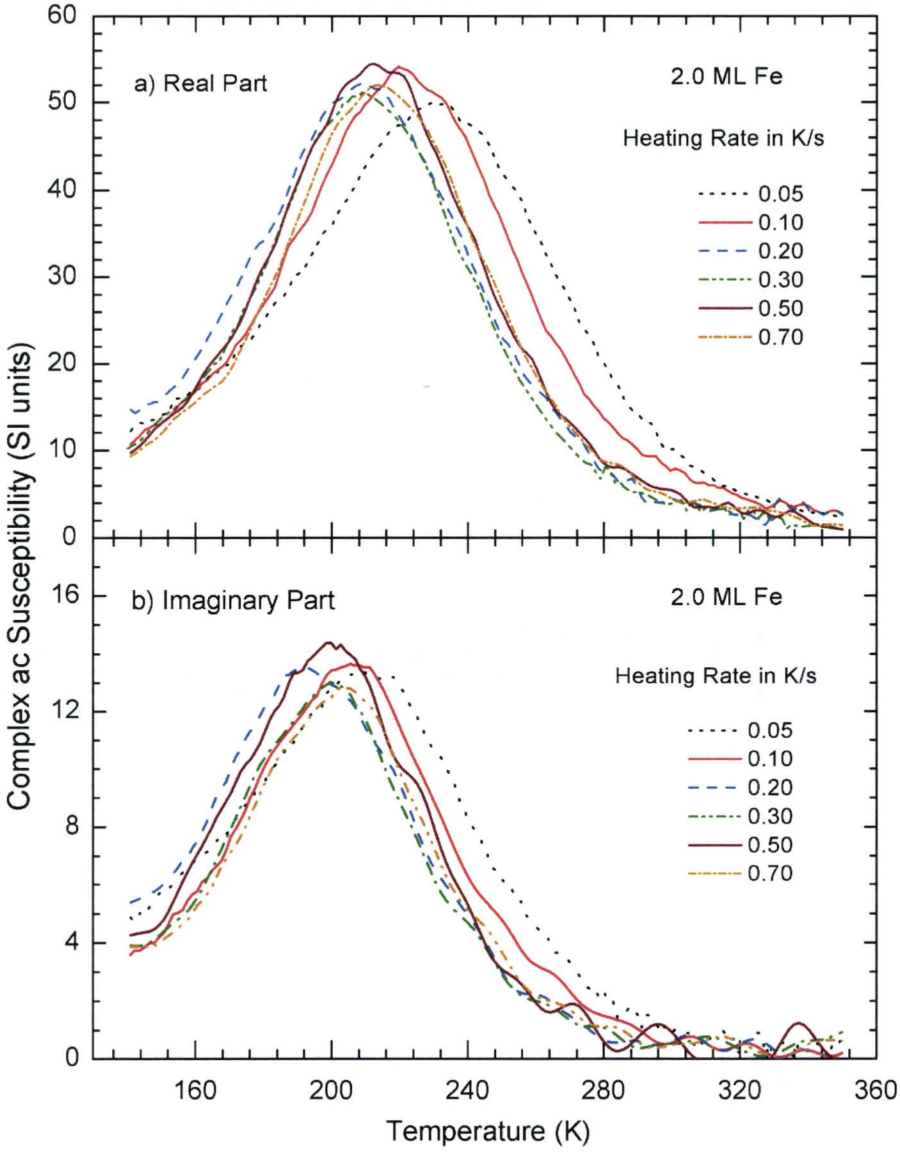

Figure A.1: *The complex ac magnetic susceptibility of 2.00 ML Fe/ 2 ML Ni/W(110) film as a function of temperature while changing the temperature at different heating rates, R.*

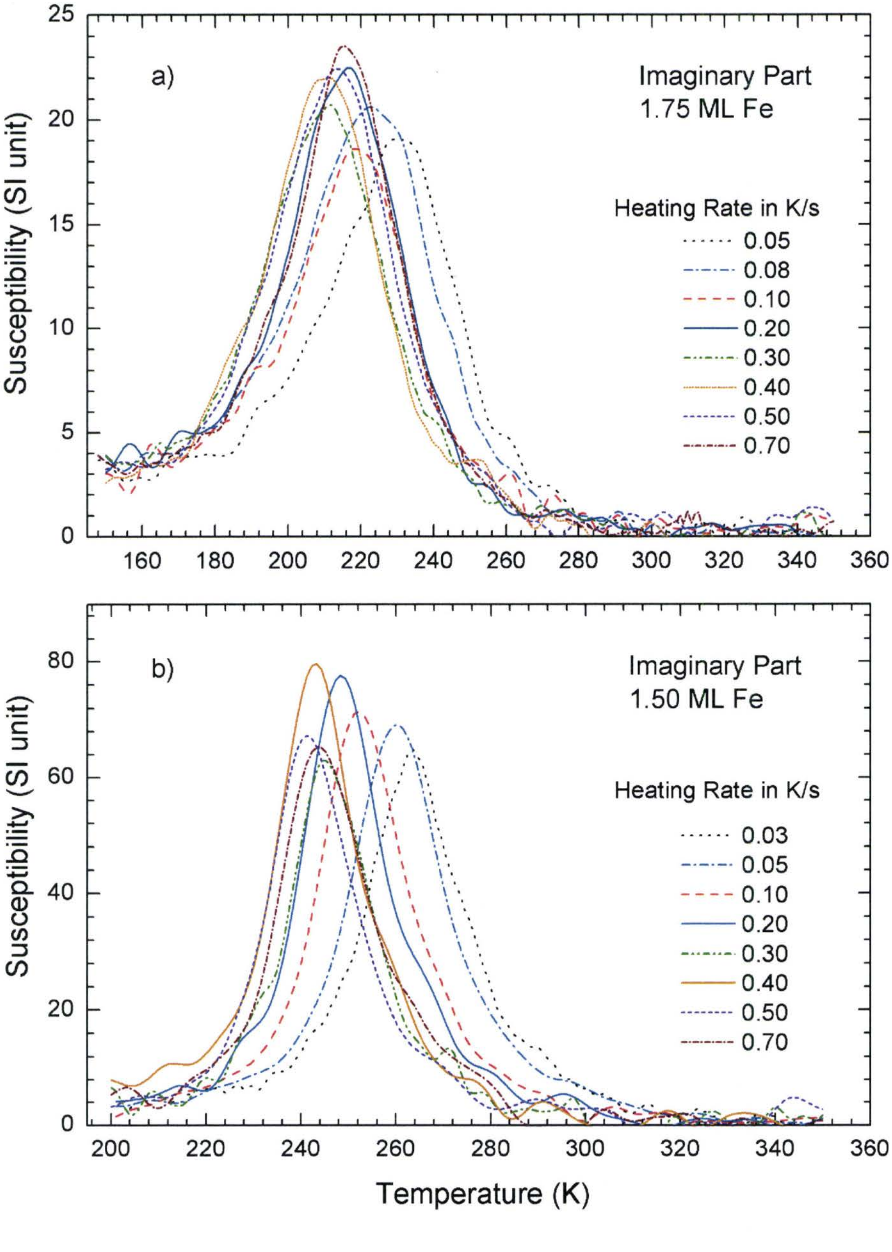

Figure A.2: *The imaginary part of the complex ac magnetic susceptibility of Fe/ 2 ML Ni/W(110) films with Fe thickness of (a) 1.75 ML and (b) 1.50 ML measured at different heating rates, R.*

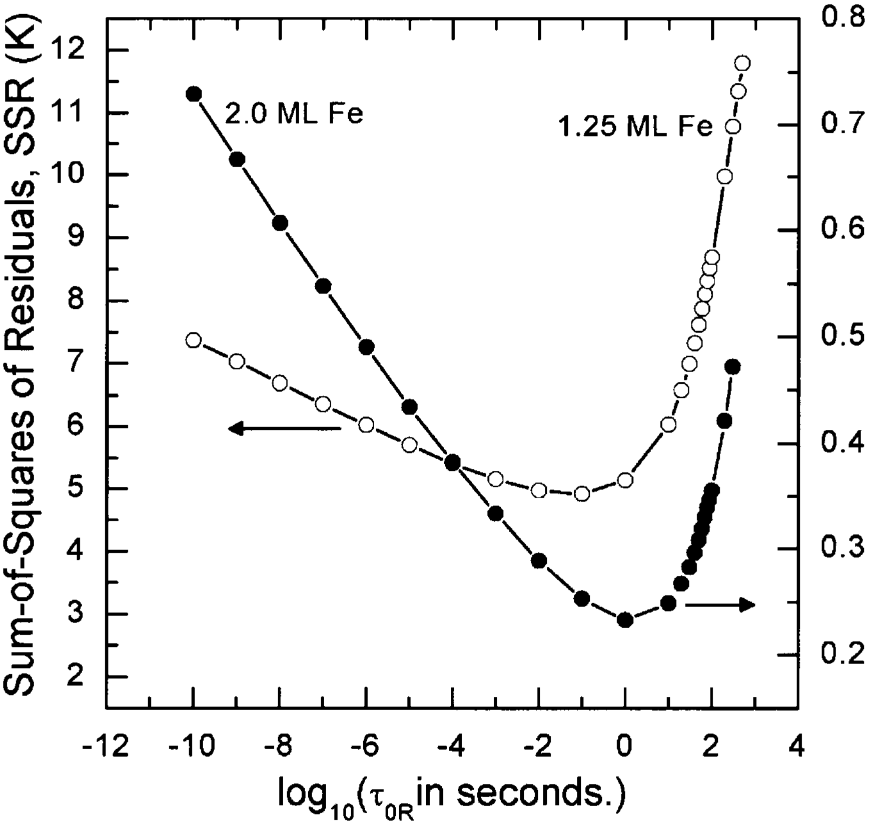

Figure A.3: *The sum-of-squares residuals* (SSR) *as a function of* $\log_{10}(\tau_{0R})$ *for the films with Fe thickness of 1.25 ML and 2.00 ML. Best fit value of* τ_{0R} *for the film of 1.25 ML Fe is* 10^{-1}*, one order of magnitude smaller than* $\tau_{0R} = 10^0$ *of other films. A possible interpretation of this is given in the main body of the text.*

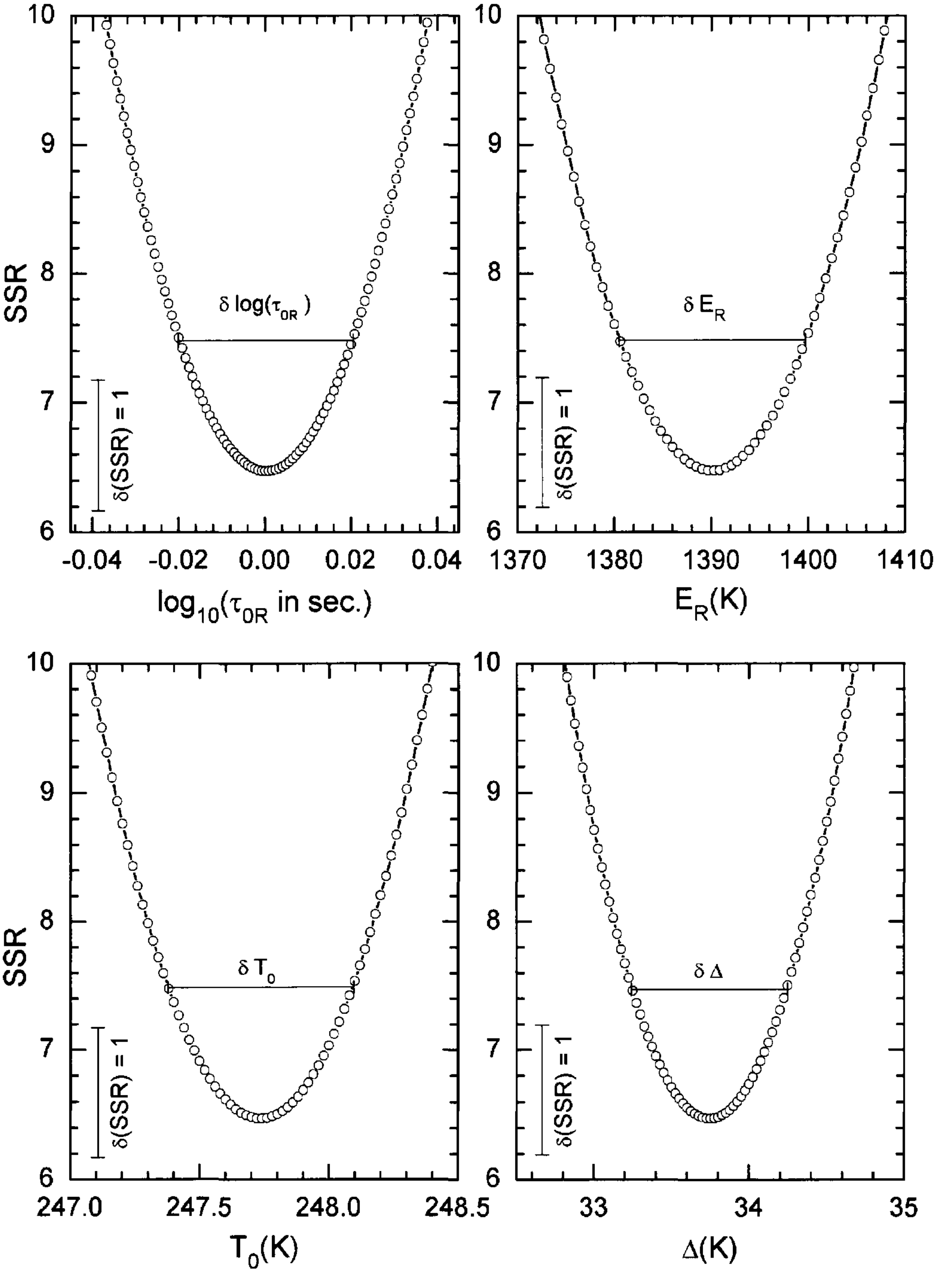

Figure A.4: *Error calculation in the best-fit parameters describing the change of the susceptibility peak temperature with the heating rate, R of Fig. 4.17 according to Eq. 4.11. This calculation is made using data from the film of 1.75 ML Fe.*

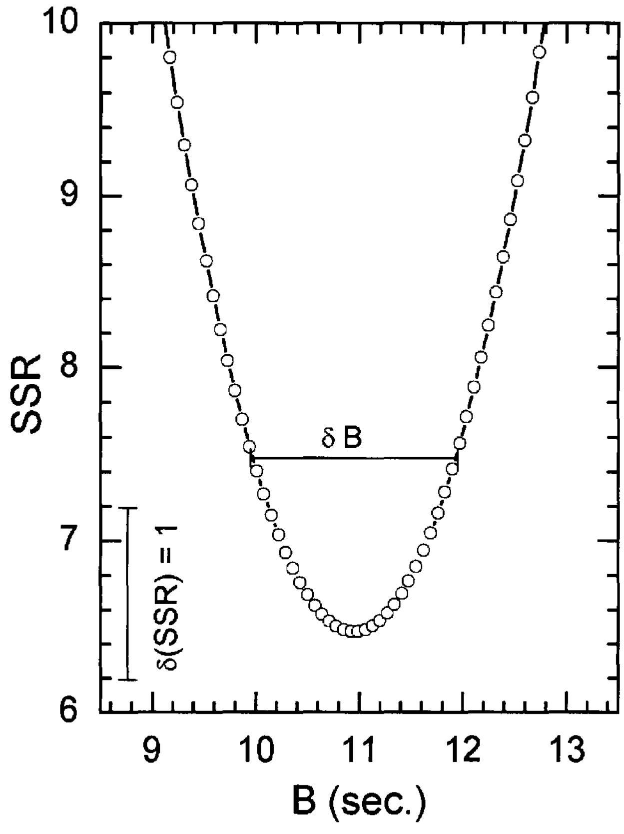

Figure A.5: *Error calculation in the parameter B. As in Fig. A.4, the data used in this calculation are relevant to the film of 1.75 ML Fe*

Bibliography

[1] M. N. Baibich, J. M. Broto, A. Fert, F. Nguyen Van Dau, F. Petroff, P. Etienne, G. Creuzet, A. Friederich, and J. Chazelas, *Phys. Rev. Lett.* **61**, 2472 (1988).

[2] S. S. P. Parkin, N. More, and K. P. Roche, *Phys. Rev. Lett.* **64**, 2304 (1990).

[3] K. De'Bell, A. B. MacIsaac, and J. P. Whitehead, *Rev. Mod. Phys.* **72**, 225 (2000).

[4] T. L. Jones and D. Venus, *Surf. Sci.* **302**, 126 (1994).

[5] H. L. Johnston, C. S. Arnold, and D. Venus, *Phys. Rev. B* **55**, 13221 (1997).

[6] O. Portmann, A. Vaterlaus, and D. Pescia, *Nature* **422**, 701 (2003).

[7] A. Berger and H. Hopster, *Phys. Rev. Lett.* **76**, 519 (1996).

[8] B. Heinrich and J. F. Cochran, *Adv. Phys.* **42**, 523 (1993).

[9] H. P. Oepen, H. P. Oepen, M. Speckmann, Y. Millev, and J. Kirschner, *Phys. Rev. B* **55**, 2752 (1997).

[10] Y. Millev and J. Kirschner, *Phys. Rev. B* **54**, 4137 (1996).

[11] D. Pescia and V. L. Pokrovsky, *Phys. Rev. Lett.* **65**, 2599 (1990).

[12] D. P. Pappas, K.-P. Kmper, and H. Hopster, *Phys. Rev. Lett.* **64**, 3179 (1990).

[13] J. P. Whitehead and K. DeBell, *J. Phys.: Condens. Mater* **6**, L731 (1994).

[14] A. Kashuba and V. L. Pokrovsky, *Phys. Rev. Lett.* **70**, 3155 (1993).

[15] A. B. Kashuba and V. L. Pokrovsky, *Phys. Rev. B* **48**, 10335 (1993).

[16] Ar. Abanov, V. Kalatsky, V. L. Pokrovsky, and W. M. Saslow, *Phys. Rev. B* **51**, 1023 (1995).

[17] R. Allenspach and A. Bischof, *Phys. Rev. Lett.* **69**, 3385 (1992).

[18] A. B. MacIsaac, J. P. Whitehead, M. C. Robinson, and K. DeBell, *Phys. Rev. B* **51**, 16033 (1995).

[19] A. B. MacIsaac, K. De'Bell, and J. P. Whitehead, *Phys. Rev. Lett.* **80**, 616 (1998).

[20] I. Booth, A. B. MacIsaac, J. P. Whitehead, and K. De'Bell, *Phys. Rev. Lett.* **75**, 950 (1995).

[21] B. Kaplan and G. A. Gehring, *J. Magn. Magn. Mater.* **128**, 111 (1993).

[22] B. Kaplan, *J. Magn. Magn. Mater.* **288**, 178 (2005).

[23] P. Politi, *Comments Condens. Matter Phys.* **18**, 191 (1998).

[24] S. P. Bromley, J. P. Whitehead, K. De'Bell, and A. B. MacIsaac, *J. Magn. Magn. Mater.* **264**, 14 (2003).

[25] L. C. Sampaio, M. P. de Albuquerque, and F. S. de Menezes, *Phys. Rev. B* **54**, 6465 (1996).

[26] S. A. Cannas, M. F. Michelon, D. A. Stariolo, and F. A. Tamarit, *Phys. Rev. E* **78**, 051602 (2008).

[27] S. A. Cannas, M. F. Michelon, D. A. Stariolo, and F. A. Tamarit, *Phys. Rev. B* **73**, 184425 (2006).

[28] S. A. Cannas, D. A. Stariolo, and F. A. Tamarit *Phys. Rev. B* **69**, 092409 (2004).

[29] M. Casartelli, L. DallAsta, E. Rastelli, and S. Regina, *J. Phys. A* **37**, 11731 (2004).

[30] A. Vaterlaus, C. Stamm, U. Maier, M. G. Pini, P. Politi, and D. Pescia, *Phys. Rev. Lett.* **84**, 2247 (2000).

[31] O. Portmann, A. Vaterlaus, and D. Pescia, *Phys. Rev. Lett.* **96**, 047212 (2006).

[32] N. Saratz, T. Michlmayr, O. Portmann, U. Ramsperger, A. Vaterlaus and D. Pescia, *J. Phys. D: Appl. Phys.* **40**, 1268 (2007).

[33] C. Won, Y. Z. Wu, J. Choi, W. Kim, A. Scholl, A. Doran, T. Owens, J. Wu, X. F. Jin, H. W. Zhao, and Z. Q. Qiu, *Phys. Rev. B* **71**, 224429 (2005).

[34] C. S. Arnold, M. Dunlavy and D. Venus, *Rev. Sci. Instrum.* **68**, 4212 (1997).

[35] C. S. Arnold, H. L. Johnston, and D. Venus, *Phys. Rev. B* **56**, 8169 (1997).

[36] C. S. Arnold, M. Dunlavy, D. Venus, and D. P. Pappas, *J. Magn. Magn. Mater.* **198**, 465 (1999).

[37] D. Venus, C. S. Arnold, and M. Dunlavy, *Phys. Rev. B* **60**, 9607 (1999).

[38] M. J. Dunlavy and D. Venus, *Phys. Rev. B* **62**, 5786 (2000).

[39] D. Venus and M. J. Dunlavy, *J. Magn. Magn. Mater.* **260**, 195 (2003).

[40] D. Sander, A. Enders, C. Schmidthals, J. Kirschner, H. L. Johnston, C. S. Arnold, and D. Venus, *J. Appl. Phys.* **81**, 4702 (1997).

[41] H. L. Johnston, *Ph.D Thesis,*(McMaster University 1997).

[42] C. S. Arnold, and D. Venus, *IEEE Trans. Magn.* **34**, 1039 (1998).

[43] P. Bruno, G. Bayreuther, P. Beauvillain, C. Chappert, G. Lugert, D. Renard, J. P. Renard, and J. Seiden *J. Appl. Phys.* **68**, 5759 (1990).

[44] P. Rosenbusch, J. Lee, G. Lauhoff, and J. A. C. Bland, *J. Magn. Magn. Mater.* **172**, 19 (1997).

[45] B. Raquet, R. Mamy, and J. C. Ousset *Phys. Rev. B* **54**, 4128 (1996).

[46] B. D. Cullity, *Introduction To Magnetic Materials.* Addison-Wesley, (1996).

[47] S. Chikazumi: *Physics of Ferromagnetism.* Oxford University Press Inc., New York (1997).

[48] R. C. O'Handley: *Modern Magnetic Materials, Principles and Applications.* Jons Wiley and Sons, Inc. (2000)

[49] P. Weiss, *J. Phys..* **6**, 661 (1907)

[50] K. Yosida, *Theory of Magnetism.* Springer-Verlag, Berlin (1996).

[51] W. Heisenberg, *Z. Physik..* **49**, 619 (1928).

[52] P. J. Jensen, S. Knappmann, W. Wulfhekel, and H. P. Oepen, *Phys. Rev. B* **67**, 184417 (2003).

[53] H. B. Callen, and E. R. Callen, *J. Phys. Chem. Solids* **27**, 1271 (1966).

[54] E. R. Callen and H. B. Callen, *J. Phys. Chem. Solids* **16**, 310 (1960).

[55] E. C. Stoner, *Proc. Roy. Soc. (London)* **A169**, 339 (1939).

[56] E. C. Stoner, *Rept. Progr. Phys.* **11**, 43 (1947).

[57] F. Brailsford, *Physical Principles of Magnetism.* D. Van Nostrand Company Ltd., London (1966).

[58] G. H. O. Daalderop, P. J. Kelly, and M. F. H. Schuurmans, *Ultrathin Magnetic Structure Vol. I.* Edited by B. Heinrich and J. A. C. Bland, Springer-Verlag, Berlin (1994)

[59] M. A. Howson, *Contemp. Phys.* **35**, 347 (1994).

[60] F. Bloch, *Z. f. Phys.* **74**, 295 (1932).

[61] L. Néel, *Compt. Rend.* **241**, 533 (1955).

[62] N. D. Mermin and H. Wagner, *Phys. Rev. lett.* **17**, 1133 (1966).

[63] M. Bander and D. L. Mills, *Phys. Rev. B* **38**, 12015 (1988).

[64] Z. Q. Qiu, J. Pearson, and S. D. Bader, *Phys. Rev. Lett.* **67**, 1646 (1991).

[65] H. J. Elmers, J. Hauschild, H. Höche, and U. Gradmann, *Phys. Rev. Lett.* **73**, 898 (1994).

[66] H. J. Elmers, J. Hauschild, G. H. Liu, and U. Gradmann, *J. Appl. Phys.* **79**, 4984 (1996).

[67] F. Huang, M. T. Kief, G. J. Mankey, and R. F. Willis, *Phys. Rev. B* **49**, 3962 (1994).

[68] Yi Li and K. Baberschke, *Phys. Rev. Lett.* **68**, 1208 (1992).

[69] M. Weinert, and A. J. Freeman, *Phys. Rev. B.* **38**, 23 (1983).

[70] L. Néel, *J. Phys. Rad.* **15**, 376 (1954).

[71] B. Heinrich, and J. A. C. Bland, *Ultrathin Magnetic Structure Vol. I.* Springer-Verlag, Berlin (1994)

[72] Y. Yafet and E. M. Gyorgy, *Phys. Rev. B.* **38**, 9145 (1988).

[73] R. Czech, and J. Villain,, *J. Phys.: Condensed Matter* **1**, 619 (1989).

[74] K. -P. Kämper, W. Schmitt, G. Güntherodt, and H. Kuhlenbeck, *Phys. Rev. B.* **38**, 9451 (1988).

[75] D. Venus, *Rev. Sci. Instrum.* **62**, 1361 (1991).

[76] E. Bauer, *Z. f. Kristallographie* **110**, 372 (1958) (in German), Bauer's homepage: http://physics.asu.edu/homepages/bauer

[77] M. Wuttig, and X. Liu, *Ultrathin Metal Films: Magnetic and Structural Properties* , springer-Verlag, Berlin (2004)

[78] J. B. Pendry, *Low-Energy Electron Diffraction*, Academic Press, New York (1974)

[79] M. A. Van Hove, and S. Y. Tong, *Surface Crystallography by LEED*, Springer-Varleg, Berlin (1979)

[80] M. A. Van Hove, W. H. Weinberg, and C. M. Chan, *Low-Energy Electron Diffraction*, Springer-Varleg, Berlin (1986)

[81] H. L. Meyerheim D. Sander, R. Popescu, J. Kirschner, O. Robach and S. Ferrer, P. Steadman *Phys. Rev. B.* **67**, 155422 (2003).

[82] M. J. Dunlavy and D. Venus, *Phys. Rev. B* **69**, 094411 (2004)

[83] M. J. Dunlavy and D. Venus, *Phys. Rev. B.* **71** 144406 (2005)

[84] S. D. Bader, *Surf. Sci.* **500**, 172 (2002).

[85] Z. Q. Qui, and S. D. Bader, *J. Magn. Magn. Mater.* **200**, 664 (1999).

[86] S. D. Bader and J. L. Erskine, *Ultrathin Magnetic Structure Vol. II.* Edited by B. Heinrich and J. A. C. Bland, springer-Verlag, Berlin (1994).

[87] C. S. Arnold, and D. Venus, *Rev. Sci. Instrum.* **66**, 3280 (1995).

[88] K. Fritsch , *M.Sc Thesis* (McMaster University, 2008)

[89] N. Abu-Libdeh and D. Venus, *Phys. Rev. B* **80**, 184412 (2009).

[90] N. Abu-Libdeh and D. Venus, *Submitted to Phys. Rev. B, arXiv:1001.4069*